Thermomechanical and Microstructural Characterization of $Co_{49}Ni_{21}Ga_{30}$ and $Co_{38}Ni_{33}Al_{29}$ High-temperature Shape Memory Alloy Single Crystals

zur Erlangung des akademischen Grades eines
DOKTORS DER INGENIEURWISSENSCHAFTEN (Dr.-Ing.)
der Fakultät für Maschinenbau
der Universität Paderborn

genehmigte
DISSERTATION

von
Jayaram Dadda
aus Indien

Tag des Kolloquiums: 09.04.2009
Referent: Prof. Dr.-Ing. H.J. Maier
Korreferent: Prof. Dr. D. Canadinc

Dedicated to my parents.

Abstract

In this study, functional behavior of newly developed Co-base $Co_{49}Ni_{21}Ga_{30}$ and $Co_{38}Ni_{33}Al_{29}$ high-temperature shape memory alloys (HTSMAs) is reported. A thorough experimental programme addressing the mechanical and functional properties of $Co_{49}Ni_{21}Ga_{30}$ and $Co_{38}Ni_{33}Al_{29}$ (in at.%) single crystalline alloys was executed in order to understand the effects due to crystallographic orientation and thermomechanical treatments.

The $Co_{38}Ni_{33}Al_{29}$ single crystals investigated in this work demonstrate a large pseudoelastic (PE) window of more than 250 °C, good cyclic stability and trainability with a maximum two-way shape memory effect (TWSME) strain of 2.7%. The results emphasize the need for texturing polycrystalline aggregates of the current material near the <001> and <110> poles with an optimum γ-phase volume fraction to achieve high functional performance in $Co_{38}Ni_{33}Al_{29}$ alloys.

In as-grown $Co_{49}Ni_{21}Ga_{30}$ specimens, the low critical transformation stress due to the high resolved shear stress factor (RSSF) value, *i.e.* low Clausius-Clapeyron (CC) slope, high slip resistance in the austenite due to zero Schmid factor and B2 atomic ordering allow for excellent transformation recoverability with a large PE temperature range of about 325 °C when loaded in the [001] direction. The thermomechanical training resulted in a stable microstructure improving the transformation recoverability, which in turn resulted in a large PE window of 400 °C in the temperature range of 40-425 °C, and also in a stable cyclic behavior. In addition, the employed high-temperature aging treatments at 900 °C for 24 hours on $Co_{49}Ni_{21}Ga_{30}$ alloys brought about a stable cyclic stress-strain response at elevated temperatures as high as 300 °C. The martensite stabilization due to pinning of moving interfaces, detwinning and diffusion of point defects in $Co_{49}Ni_{21}Ga_{30}$ alloys especially at elevated temperatures (>120 °C) is macroscopically reflected by the shift of the unloading curve to lower stress levels and consequently resulted in a large stress hysteresis of about 350 MPa. Along with the *in-situ* microscopy, the spatial visualization of strain localization obtained by using digital image correlation (DIC) revealed heterogeneous transformation characteristics at temperatures below 120 °C, beyond which the nucleation and growth characteristics of SIM transformation are quasi-homogeneous resulting in a multi-variant configuration, which was later inherited by the trained crystal. An insight into the evolution of the microstructure and stress-strain behavior in terms of stress hysteresis with test temperatures is provided, and the possible operant mechanisms are presented.

Contents

Nomenclature

Greek Symbols

σ_{crit}^{For}	Critical stress for forward transformation
ϵ_{CVP}	CVP formation strain
ϵ_{det}	Detwinning strain
ϵ	Engineering strain
ϵ_{ps}	Permanent strain
ϵ_{res}	Residual strain
σ	Engineering stress
σ_{crit}^{Rev}	Critical stress for reverse transformation
$\Delta\epsilon$	Strain Range
$\Delta\sigma$	Stress Hysteresis
ϵ_T	Transformation strain

Superscripts

For	superscript Forward Transformation
Rev	superscript Reverse Transformation

Subscripts

$crit$	subscript Critical Value
f	subscript Finish
s	subscript Start

Acronyms

A	Austenite
AC	Air-cooled
A_f	Austenite Finish
A_s	Austenite Start
CC	Clausius-Clapeyron
$CSSR$	Cyclic Stress-Strain Response
CVP	Corresponding Variant Pair
DIC	Digital Image Correlation
DSC	Differential Scanning Calorimetry
$EBSD$	Electron Back-scattered Diffraction
$HTPM$	High-temperature Pseudoelastic Material
$HTSMA$	High-temperature Shape Memory Alloy
IST	Incremental Strain Test
M	Martensite
M_f	Martensite Finish
$MFIS$	Magnetic Field-Induced Strain
MR	Martensite Reorientation
M_s	Martensite Start

$MSMA$	Magnetic Shape Memory Alloy
$MSME$	Magnetic Shape Memory Effect
MT	Martensitic Transformation
OM	Optical Microscopy
OQ	Oil-quenched
$OWSME$	One-Way Shape Memory Effect or Shape Memory Effect
PE	Pseudoelasticity
$SADP$	Selected Area Diffraction Pattern
$SC-SRO$	Symmetry Conforming-Short Range Ordering
SCV	Single Correspondence Variant
SEM	Scanning Electron Microscope
SIM	Stress-induced Martensite
SMA	Shape Memory Alloy
SME	Shape Memory Effect
TEM	Transmission Electron Microscope
$TWSME$	Two-Way Shape Memory Effect
WQ	Water-quenched

Introduction and Scope of Research

In recent years, search for new shape memory alloys (SMAs) that can undergo phase transformations at high temperatures has been the focus of many researchers around the world owing to poor thermal stability, workability and pseudoelasticity (PE) of existing SMA systems. This is necessary for robotic, automotive, aerospace, turbine engine and air-conditioning industries where the operating temperatures are often well above 100 °C. In this study, the results related to different investigations carried out on new class of Co-Ni-Al and Co-Ni-Ga high-temperature shape memory alloy (HTSMA) material are presented. In particular, using proper experimental procedures, the thermomechanical behavior of the material was investigated under static and cyclic loading conditions to better understand the deformation mechanisms involved in the shape memory effect (SME) and PE.

Thermomechanical characterization of $Co_{49}Ni_{21}Ga_{30}$ and $Co_{38}Ni_{33}Al_{29}$ alloys was undertaken on their single crystals with the loading axis along the [001], [123], [235] and [110] crystallographic orientations. The use of single crystals allows a systematic bias of operant deformation mechanisms such as martensite variant reorientation, detwinning and dislocation slip, which facilitates the fundamental understanding of the phase transformation and the stress-strain response in $Co_{49}Ni_{21}Ga_{30}$ and $Co_{38}Ni_{33}Al_{29}$ alloys. Several appropriate heat-treatments were also performed to optimize the shape memory characteristics of these alloys. In addition, to gain an understanding of the other orientation dependence of the transformation stress and transformation strain levels, theoretical values for the resolved shear stress factors (RSSFs) and transformation strains were calculated using the energy minimization theory. This information is needed to fabricate a textured polycrystalline material already optimized for desired functional properties that are necessary for the envisaged applications.

In addition, high-temperature *in-situ* optical microscopy (OM) was carried out at various stages during the PE experiments to follow the evolution of the stress-induced phase transformation and to track the propagation of phase boundaries. Along with these investigations, a full-field digital image correlation (DIC) was also employed to obtain the local strain fields during loading and unloading. This information is essential for the constitutive modeling of inhomogeneous and homogeneous deformation regimes in SMAs. The present $Co_{49}Ni_{21}Ga_{30}$ and $Co_{38}Ni_{33}Al_{29}$ alloys displayed pronounced cyclic stability at elevated temperatures under compressive loading conditions indicating their potential as promising HTSMAs for PE applications that involve high stress levels. Part of the data presented herein has already been published elsewhere Canadinc *et al.* (2007); Dadda *et al.* (2006a,b, 2008, 2009); Meyer *et al.* (2006); Niklasch *et al.* (2008) due to the rapid evolution in the field.

Chapter 1

Theoretical Background

1.1 Shape Memory Alloys

Smart Materials are able to note an external stimulus responding in a predetermined and repeatable manner; this capacity permits the material to change its geometrical and thermomechanical conditions. In this field, SMAs are a class of materials able to remember a predetermined configuration and to recover it as consequence of thermal or mechanical loads. NiTi, Cu-base and Au-Cd alloys are the most commonly used and widely studied SMAs due to their abundance and inexpensive constituent elements especially in Cu-Zn-Al, Cu-Al-Ni alloys Duerig *et al.* (1990); Otsuka & Wayman (1999). The special functional properties exhibited by these alloys, namely one way or two way shape memory effect (OWSME, TWSME) and pseudoelasticity are the phenomena being exploited in a number of industrial fields such as biomedical, automotive, aerospace and turbine engines. The use of SMAs seems to be very useful in applications where it is necessary to use smart components with small dimensions. Many conventional actuators and sensors could be substituted with SMAs, obtaining high advantages in terms of reduction of weight and dimensions, reliability and costs. Furthermore, in the last years, their use for the realization of smart composites, as an example for vibration and shape control, is becoming very interesting.

Unfortunately, there are still some difficulties with SMAs that must be overcome before they can live up to their full potential. For example, these alloys are still relatively expensive to manufacture compared to other materials such as steel and aluminium. These difficulties regard the high sensibility to the production parameters. Furthermore, the non-linear characteristics of their behavior increases the difficulties related to the control of their functional properties. For this reason, in the last decades, many research activities have been addressed to the investigation of the influence of different working processes on the SMA behavior and to develop simple numerical models able to simulate it.

1.2 Reversible Martensitic Transformation

Martensitic transformations (MTs) are diffusionless, solid-to-solid phase transitions, and have been observed in metals, alloys, ceramics and polymers Otsuka & Wayman (1999). MTs can be irreversible, as seen in steels upon quenching, or they can be reversible (often termed 'thermoelastic'), such as those observed in SMAs. In the latter case, the microstructures formed on cooling can easily be manipulated by external loads and disappear upon reheating causing large reversible shape changes in SMAs. As the MT is associated with a shape change, a large strain develops around the martensite when it is formed in the parent phase (high temperature phase) Otsuka & Wayman (1999). This will increase the strain energy at the interface between austenite and martensite and consequently raises the total energy of the system. In order to minimize this energy the MT involves a pure shear that occurs either by internal slip or internal twinning as shown in Figure 1.1 Duerig *et al.* (1990); Otsuka & Wayman (1999). These two mechanisms are known as the lattice invariant shear, since neither process changes the structure of the martensite. The selection of either slip or twinning depends on the kind of alloy, but twinning is usually preferred to slip in SMAs. Schematic in Fig. 1.1c shows the twinned morphology where a twin boundary separates two martensite domains V_1 and V_2. It should be noted that V_1 and V_2 have the same structure, but the orientations are different as they are mirror reflections of each other across the twin boundary. Thus, these are also known as a corresponding variant pair (CVP) of the martensite. When a CVP is exposed to external stimuli such as magnetic or electric fields (in certain ferroelectric materials) or stress fields, the martensitic domains, V_1 in the present case, which are more favorable to external forces will grow in expense of others via twin boundary

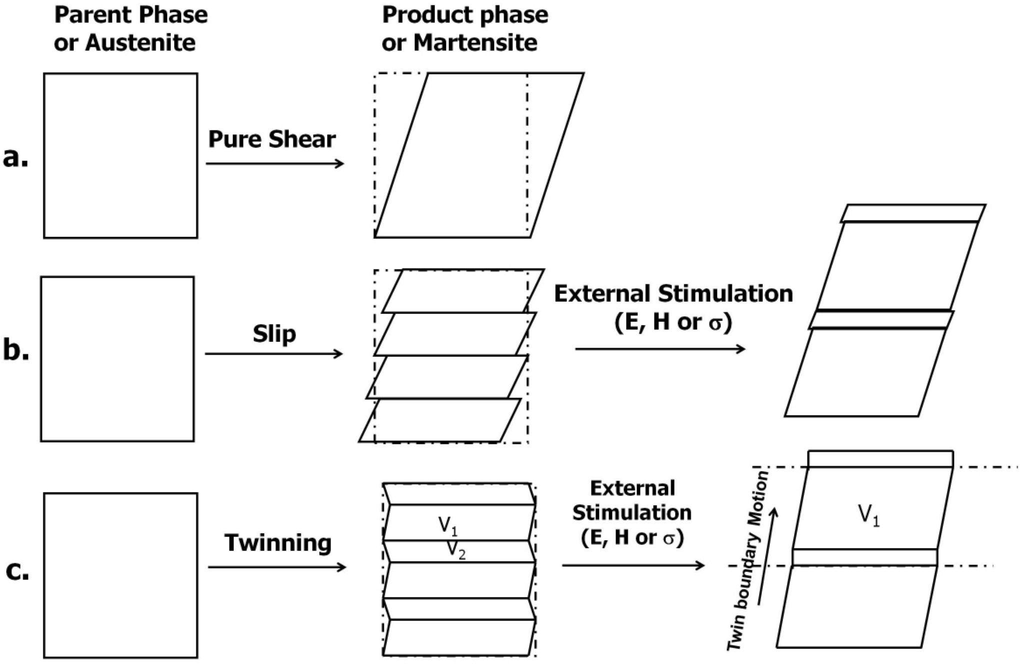

Figure 1.1: Schematics demonstrating the formation of martensite through a shear process from a single crystalline austenite

motion as illustrated in Fig. 1.1c, i.e. detwinning occurs giving rise to a large transformation strain. Based on these mechanisms, SMAs exhibit several phenomena accompanied with reversible MT coupled with external stresses, namely SME, PE and TWSME. It is worth to mention the thermodynamics of MT in SMAs before elucidating these phenomena in brief.

1.3 Thermodynamic Aspects of the Martensitic Transformations

In SMAs, martensitic transformations are characterized by the non-equilibrium transformation temperatures, namely M_s, martensite start, M_f, martensite finish, A_s, austenite start, and A_f, austenite finish temperature. A_f is the temperature above which the martensite becomes completely unstable. These transformation temperatures can be determined by measuring some physical properties such

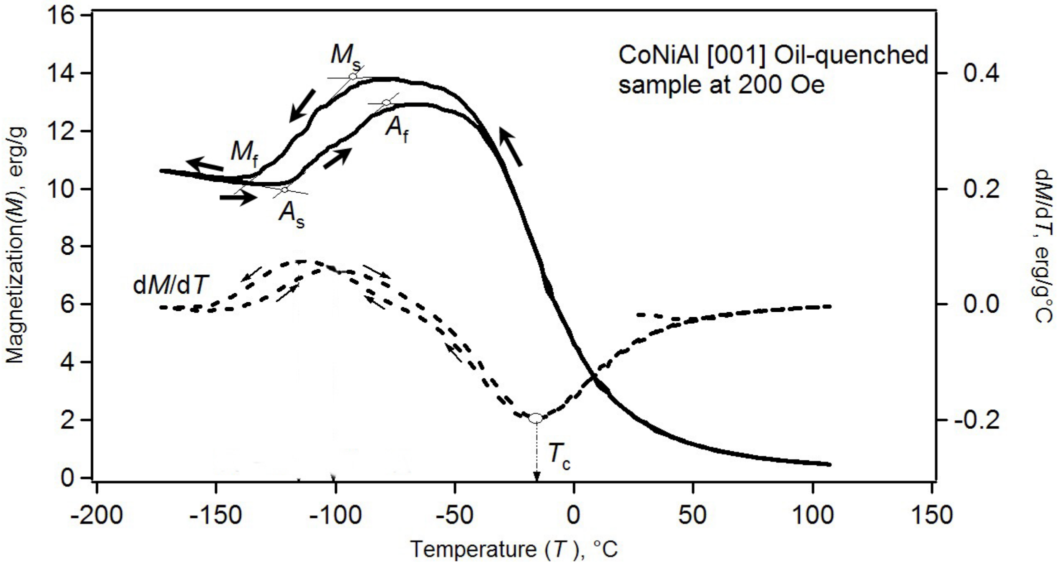

Figure 1.2: Magnetization-temperature response of $Co_{38}Ni_{33}Al_{29}$ alloy under a constant magnetic field of 200 Oe. The arrows indicate the cooling and heating paths of the curves.

as electrical resistance, magnetization, heat change as a function of temperature, since these properties drastically change upon reaching these temperatures. This is illustrated with help of a magnetization curve shown in Figure 1.2 for a $Co_{38}Ni_{33}Al_{29}$ system. Since the austenite and martensite phases have different magnetic properties, magnetization of the material changes upon thermal cycling clearly indicating the both forward and reverse transformations reflecting as slope changes as seen in the figure. The inflection points are considered as transformation temperatures as marked in Fig. 1.2. The minima on the curve obtained by plotting the change in magnetization with respect to temperature (dM/dT) is considered as the Curie temperature (T_c) above which the material becomes paramagnetic.

As the martensitic transformations are not associated with a compositional change, the free energy curves of both parent and martensite phases as a function of temperature may be represented schematically as shown in Figure 1.3. Fig. 1.3 shows that the forward transformation (A → M) occurs at the M_s temperature

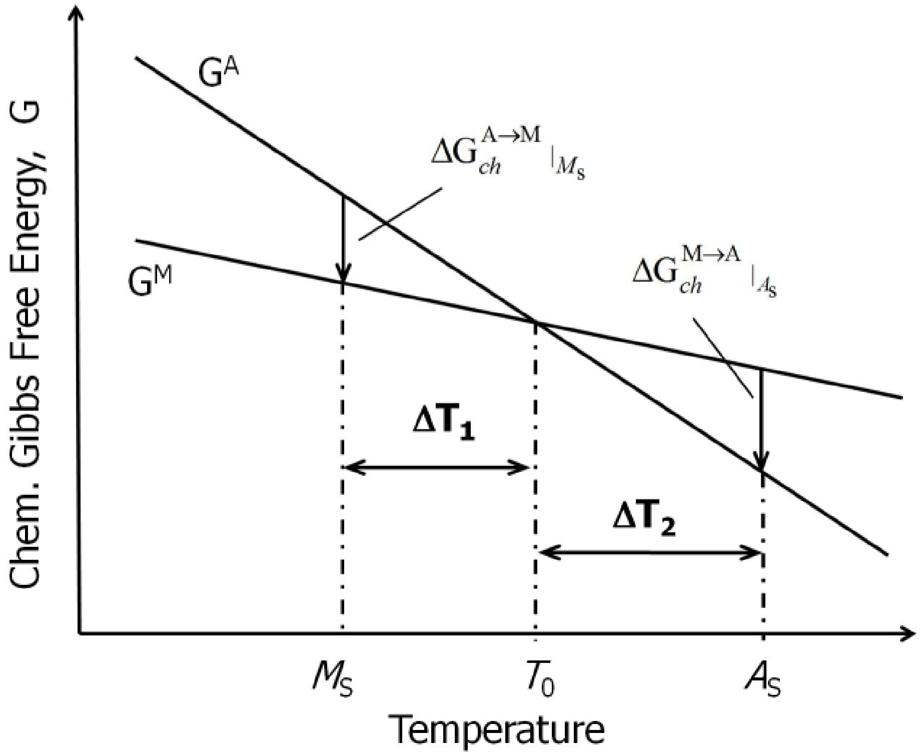

Figure 1.3: Schematic representation of free energy curves for both austenite (G^A) and martensite (G^M) phases, and their relation to the M_s and A_s temperatures. ΔT_1 and ΔT_2 are the under-cooling and over-heating required for forward and reverse transformations, respectively.

(where $\Delta G_{ch}^{A\rightarrow M}\mid_{M_s} = G^M - G^A < 0$) instead of thermodynamic equilibrium temperature T_0 at which the free energies of the two phases are equal. This brings about an under-cooling ΔT_1 that is necessary for the onset of MT. The same arguments apply for the reverse transformation (M → A) as well at the A_s temperature resulting in an overheating ΔT_2 (Fig. 1.3). An additional chemical driving force ΔG_{ch} to overcome energy barrier that is due to the generation of elastic energy (ΔG_{el}) and a surface energy (ΔG_s), and to the frictional work spent during the growth of martensite and dislocation formation (ΔG_{fr}) is responsible for this shift Otsuka & Wayman (1999); Panchenko *et al.* (2008); Patoor *et al.* (2006); Rösner *et al.* (2001). Thus, the energy balance for the onset of MT can be written as Panchenko *et al.* (2008); Rösner *et al.* (2001):

$$-\Delta G_{ch}^{A\to M} + \Delta G_{rev}^{A\to M} + \Delta G_{fr}^{A\to M} = -\Delta G_{ch}^{A\to M} + \Delta G_{nc}^{A\to M} = 0 \tag{1.1}$$

Here $\Delta G_{rev} = \Delta G_{el} + \Delta G_s$ is the reversible component of the non-chemical free energy ($\Delta G_{nc}^{A\to M}$), which increases with the volume fraction of martensite. $\Delta G_{fr}^{A\to M}$ is the irreversible component of $\Delta G_{nc}^{A\to M}$, which characterizes the energy dissipation during forward transformation. It is clear from Eq. 1.1 that ΔG_{nc} is as large as ΔG_{ch}, which is valid for the most of MTs and is also rationale behind the aforementioned under-cooling $\Delta \mathrm{T}_1$. This can be shown as follows: At T_0, the chemical Gibbs free energy change , $\Delta G_{ch} = \Delta H - T\Delta S$, equals zero, *i.e.* $T_0 = \Delta H/\Delta S$ (Fig. 1.3). ΔH and ΔS are the change in chemical enthalpy and entropy, respectively. Re-arranging Eq. 1.1 leads to the following expression for the M_s temperature:

$$M_s = T_0 - \frac{\Delta G_{rev}^{A\to M} + \Delta G_{fr}^{A\to M}}{\Delta S} \tag{1.2}$$

From Eq. 1.2, the under-cooling ΔT_1 (M_s - T_0) can be described by the second term, which is proportional to non-chemical Gibbs free energy term. Similarly, further undercooling $M_f - M_s$ is needed to complete MT as the elastic energy around martensite resists the growth of the martensite unless a further driving force (*i.e.* cooling) is provided externally. By the same token, A_s is not the same as A_f giving way to the necessary overheating for the completion of reverse transformation in many alloys.

1.4 Shape Memory Effect (SME)

Since the MT lowers the symmetry of a crystal without involving atomic exchange or diffusion, a single crystal of the parent phase is split into many twin-related domains called CVPs as said earlier. Figure 1.4 illustrates that, when the above-mentioned alloy is deformed below the M_s temperature, i.e. when the twinned martensite is prevailing, the strain can be accommodated by the easy reversal of some of the domains into new ones i.e. detwinned or reoriented variants. Since the stress-induced domains have the same martensitic structure as before and the

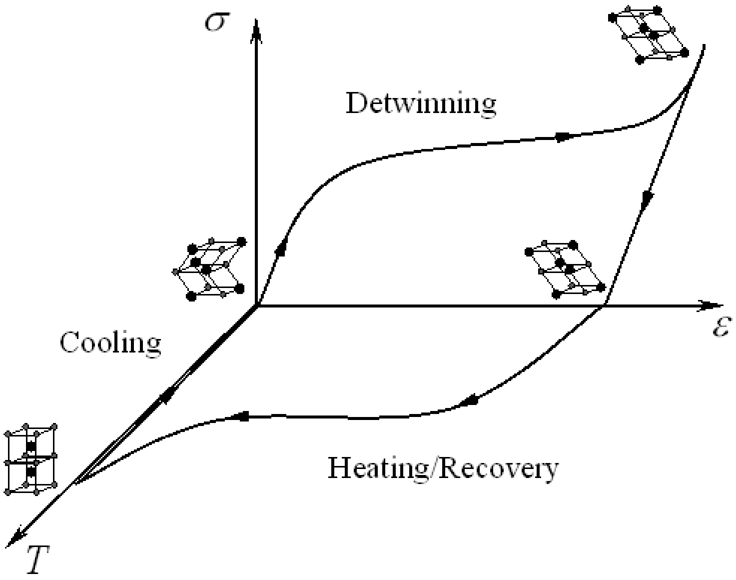

Figure 1.4: A schematic demonstrates the occurrence of the shape-memory effect with the help of a stress-strain-temperature diagram.

martensite is the stable phase below M_s, which is the working temperature, the original domains cannot be restored even after the stress is released as shown in the figure. This leads to an irrecoverable strain for the reoriented martensite. This strain can be restored, when the alloy is heated sufficiently to reach A_f such that austenite is induced and then a subsequent cooling is needed to obtain the original state of the alloy (Fig. 1.4). These processes in the aforementioned sequence result in a phenomenon commonly known as the shape-memory effect (SME), as the alloy remembers its original shape/dimensions upon heating and subsequent cooling from its deformed condition.

1.5 Pseudoelasticity (PE)

Pseudoelasticity is a phenomenon that generally occurs when an SMA is deformed at temperature sufficiently above A_f and is associated with the stress-induced martensite (SIM). The schematic in Figure 1.5 represents the typical stress-strain behavior of an SMA at temperatures above A_f. As austenite is the stable phase above A_f, initial loading results in linear elastic deformation of

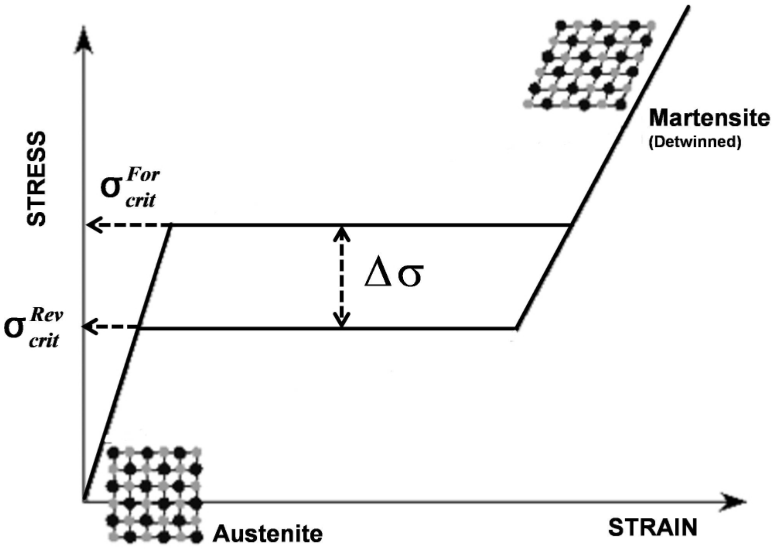

Figure 1.5: A schematic illustrating a typical pseudoelastic stress-strain curve.

austenite. The initial departure from linearity indicates the onset of SIM and the corresponding stress level is known as the critical stress levels for SIM or forward transformation (σ^{For}_{crit}) as marked in the figure. As the loading continues, the level of strain continues to increase pointing out the transformation of untransformed austenitic regions in the sample. Further loading leads to an apparent hardening behavior, which indicates the elastic deformation of martensite as well as detwinning of twinned martensite. Note that this second linear loading curve does not reveal the completeness of the stress-induced austenite to martensite transformation. Finally, as the martensite is unstable at this test temperature, SIM will transform back to austenite on unloading, thereby completely recovering the large strain accompanying a stress hysteresis, $\Delta\sigma$, as marked in the figure. Thus, this phenomenon is referred to as pseudoelasticity. In addition, the unloading curve also shows the same trend as the loading curve, where the first deviation from linearity corresponds to the onset of reverse transformation, and is called the critical stress for the reverse transformation, σ^{Rev}_{crit}, as indicated in Fig. 1.5.

Moreover, the effect of temperature, T, on PE can be understood based on the Clausius-Clapeyron (CC) relationship as follows:

$$\frac{d\sigma_{crit}^{For}}{dT} = -\frac{\Delta S}{\epsilon_0} = -\frac{\Delta H}{\epsilon_0 T_0} \tag{1.3}$$

where ϵ_0 is the transformation strain, ΔS is the entropy of transformation per unit volume, and ΔH the enthalpy of transformation per unit volume. It is clear from Eq. 1.3) that σ_{crit}^{For} follows a linear relationship with test temperature, T, for a constant ratio between ΔS and ϵ_0 at all temperatures. In other words, the left-hand term in Eq. 1.3, *i.e.* the CC-slope, is constant for a given SMA system producing a linear relationship between critical stress and temperature.

In Figure 1.6, the straight line with positive slope represents the critical stress to induce SIM with temperature. This is in accord with the CC relationship in Eq. 1.3, since ΔH is exothermic for SIM in the equation. The reason for the increase in critical stress levels with increasing test temperature is that the austenite becomes more stable at higher temperatures, and thus a higher stress level is needed to induce SIM. Fig. 1.6 also demonstrates that both PE and SME

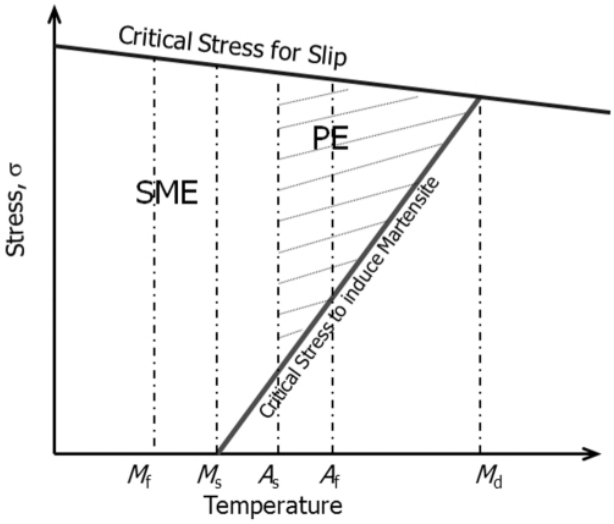

Figure 1.6: Stress-Temperature diagram that shows the region of the shape-memory effect and pseudoelasticity in temperature-stress coordinates.

are observable in the same sample, depending upon the test temperature, as long as the critical stress for slip is high enough. A straight line with negative slope represents the critical stress for slip. Since slip is irreversible upon heating or unloading, the stress must be below this line to realize either SME or PE. It should be noted that, in the temperature regime between M_s and A_s, both phenomenon may take place partially. The temperature above which no more SIM can be observed is defined as M_d on the abscissa as shown in the figure. In addition, the temperature difference $M_d - M_s$ is also considered as the PE temperature window/range in which an SMA can exhibit pseudoelasticity. This is a very important parameter for an SMA system, as it determines the working temperatures at which the alloy can be exploited for PE applications.

1.6 Two-way Shape Memory Effect (TWSME)

The TWSME is generally resulted in SMAs by repeating the forward and reverse transformations. This can be achieved either by isobaric thermal cycles or through isothermal stress-strain cycles. This will induce and increase the dislocation density in the matrix as MTs are commonly accompanied by defect formation. This causes the nucleation and growth of most favorable martensitic variants due to the stress fields generated around the dislocations. This makes the alloy to remember the shape of the sample in the martensitic state every time when the sample is cooled to below M_s. The subsequent heating will revert the specimen to its original austenitic state/shape. In this way, if heating and cooling is repeated even in the absence of external forces, the specimen changes its shapes between martensite and austenite. This is called two-way shape memory effect.

1.7 Cyclic stress-strain response (CSSR) of Shape Memory Alloys

SMAs can yield large forces in actuators Duerig *et al.* (1990); Otsuka & Wayman (1999), and possess high damping capacity both in the austenitic state, where the SIM transformation takes place, and in the martensitic state because of the SIM variant reorientation Liu *et al.* (1999). In many applications, a thermomechanical loading path utilizing the PE effect is repeated often involving a large number of loading and unloading cycles above the A_f temperature. Irrecoverable strains accumulated during cyclic loading may result in loss of the pseudoelastic material response, thus, good cyclic stability is an essential criterion for SMAs. Therefore, it is important to comprehend the evolution of the cyclic stress-strain characteristics and the associated operant mechanisms that cause the degradation of the functional properties in SMAs.

For the widely studied NiTi and Cu-Zn-base SMA systems, it has been reported that cyclic deformation initially results in an increase in the residual strain, a decrease in the critical stress for inducing SIM and a decrease in the stress hysteresis Gall & Maier (2002); Kato *et al.* (1999); Miyazaki *et al.* (1986); Sehitoglu *et al.* (2001a). However, with increasing number of cycles, the effects become less pronounced and finally steady state PE characteristics may be attained Eggeler *et al.* (2004); Gall & Maier (2002); Gall *et al.* (1999); Kato *et al.* (1999); Liu *et al.* (1999); Miyazaki *et al.* (1986); Nemat-Nasser & Guo (2006); Sehitoglu *et al.* (2001a); Strnadel *et al.* (1995); Yawny *et al.* (2005). The changes in stress-strain characteristics are attributed to the introduction and accumulation of dislocations during the repeated SIM transformations Miyazaki *et al.* (1986). Therefore, it is necessary to raise the critical stress for slip in order to stabilize the PE characteristics during cyclic loading. Strengthening against dislocation slip can be achieved through precipitation hardening or by reducing the grain size in polycrystalline material. Thus, several studies have focused on precipitated NiTi single crystals Gall & Maier (2002); Gall *et al.* (1999); Sehitoglu *et al.* (2001a), and ultra-fine grained NiTi wires and bulk material Yawny *et al.* (2005) in an attempt to capture the inherent orientation dependent cyclic pseudoelastic properties and to provide the parameters needed for constitutive modeling.

1.8 Co-base Alloys

The magnetic shape memory alloys (MSMAs) are a new class of smart materials that exhibit magnetic shape memory effect (MSME), which involves the magnetic field-controlled reversible shape changes resulting in faster response time than the temperature driven reversible shape changes in conventional SMAs. Heusler Ni_2MnGa alloys are widely studied MSMAs since the pioneering work of Ullakko *et al.* (1996). This alloy in its single crystalline state is well-known for its superior MSMA properties such as large magnetic field-induced strains (MFIS) of about 9.5 % via a rearrangement of martensite twin variants induced by an external magnetic field Sozinov *et al.* (2002). However, the poor ductility of Ni_2MnGa in the polycrystalline state Oikawa *et al.* (2001) and low blocking stress levels Karaman *et al.* (2006) limits its applications. Therefore, in the pursuit of fabricating an alternative to Ni_2MnGa alloys, the new Co-base alloys have been developed because of their natural ferromagnetism and ability to undergo thermoelastic maratensitic transformations Craciunescu *et al.* (2002); Oikawa *et al.* (2001); Sato *et al.* (2003). Some other attributes that make CoNiAl and CoNiGa alloys interesting MSMA candidate materials are: better ductility compared to NiMnGa due to secondary γ-phase in the matrix Sato *et al.* (2003), wide range of transformation temperatures Craciunescu *et al.* (2002); Oikawa *et al.* (2001, 2006), and higher Curie temperature, $T_c > 150$ °C, thus giving way to higher magnetization at operating temperatures below T_c. In addition, there are several studies that investigated thermo-mechanical characteristics of Co-Ni-Al and Co-Ni-Ga systems in relation to the expected MSME in these alloys Canadinc *et al.* (2007); Dadda *et al.* (2006a); Efstathiou *et al.* (2004); Hamilton *et al.* (2004, 2005); Li *et al.* (2004); Zhang *et al.* (2005). However, reports on the any observed MSME phenomenon of these Co-base alloys are very scarce in the literature, owing to their high twinning stresses that require relatively large magnetic fields to exhibit any MFIS Chernenko *et al.* (2004); Niklasch *et al.* (2008); O'Handley (1998). Nevertheless, recent studies Canadinc *et al.* (2007); Dadda *et al.* (2006a,b) have shown that these alloys are promising HTSMAs, therefore, the current study mainly focused on their high-temperature characterization.

Several other HTSMA systems reported to date are CuZnAl, CuAlNi, ZrCu-base, NiTiHf, NiTiZr, NiTiPd, NiTiPt, NiMnGa and NiAl Firstov *et al.* (2004b); Otsuka & Wayman (1999); Segui *et al.* (2005). However, these SMAs suffer from several problems, for instance, Cu-based alloys are considered unstable, as they tend to decompose into other non-transformable phases Duerig *et al.* (1990); Otsuka & Ren (1999). The NiTiHf, NiTiZr and NiMnGa alloys, on the other hand, are too brittle for practical use Otsuka & Ren (1999). As for the NiTiPd and NiTiPt alloys, the high cost of Pd and Pt elements and poor pseudoelasticity of ZrCu-base alloys hinders their widespread use Firstov *et al.* (2004a). The NiAl alloys received considerable attention for HTSMA as well as high temperature structural applications, since they are relatively inexpensive, their martensite start (M_s) temperature may be raised up to 900 °C depending upon composition Otsuka & Ren (1999), and they possess a high melting temperature, relatively low density and good resistance to oxidation Tian *et al.* (1998). Nevertheless, they still suffer from a lack of low temperature ductility, lack of high temperature creep strength, and are unstable at high temperatures Otsuka & Ren (1999); Tian *et al.* (1998). Researchers have succeeded in improving workability of NiAl alloys by the addition of Fe, Mn and Co as ternary elements Otsuka & Wayman (1999). Thus, the CoNiAl system acquired hot workability and room-temperature ductility by incorporating a small amount of disordered γ (Ni,Co,Al: A1) within the β ((Ni,Co)Al: B2)-matrix Oikawa *et al.* (2001); Tian *et al.* (1998).

Figure 1.7 shows the phase constitution of Co-Ni-Al system taken from Kainuma *et al.* (1996) and equilibria among the β, γ and γ' ((Ni,Co)$_3$Al: L1$_2$) phases. The phase relations concerned with these phases play a key role on the practical design of high temperature Co-Ni-Al material. In particular, the γ' phase shows the anomalous positive temperature dependence of strength, while the β phase is used for the surface coating because of its excellent oxidation resistance Kainuma *et al.* (1996). Moreover, the β phase appears in a wide range of compositions (the shaded region) as shown in Fig. 1.7 and undergoes a thermoelastic martensitic transformation to L1$_0$ in structure and exhibits the shape memory effect Kainuma *et al.* (1996) and pseudoelasticity at elevated temperatures as high as 200 °C Karaca *et al.* (2003). Another important feature of these alloys is the absence of highly volatile alloying elements, such as Mn in the case of high-temperature NiMnGa alloys, so that one can control the chemical composition more accurately. This is necessary for adjusting the transformation temperatures as they are very sensitive to the content of Nickel Oikawa *et al.* (2001). Furthermore, in continuing efforts made to provide some ductility to various intermetallic compounds, there has been an attempt by Kimura *et al.* (1994) to make B2 CoAl, an intrinsically brittle high temperature material, ductile by controlling

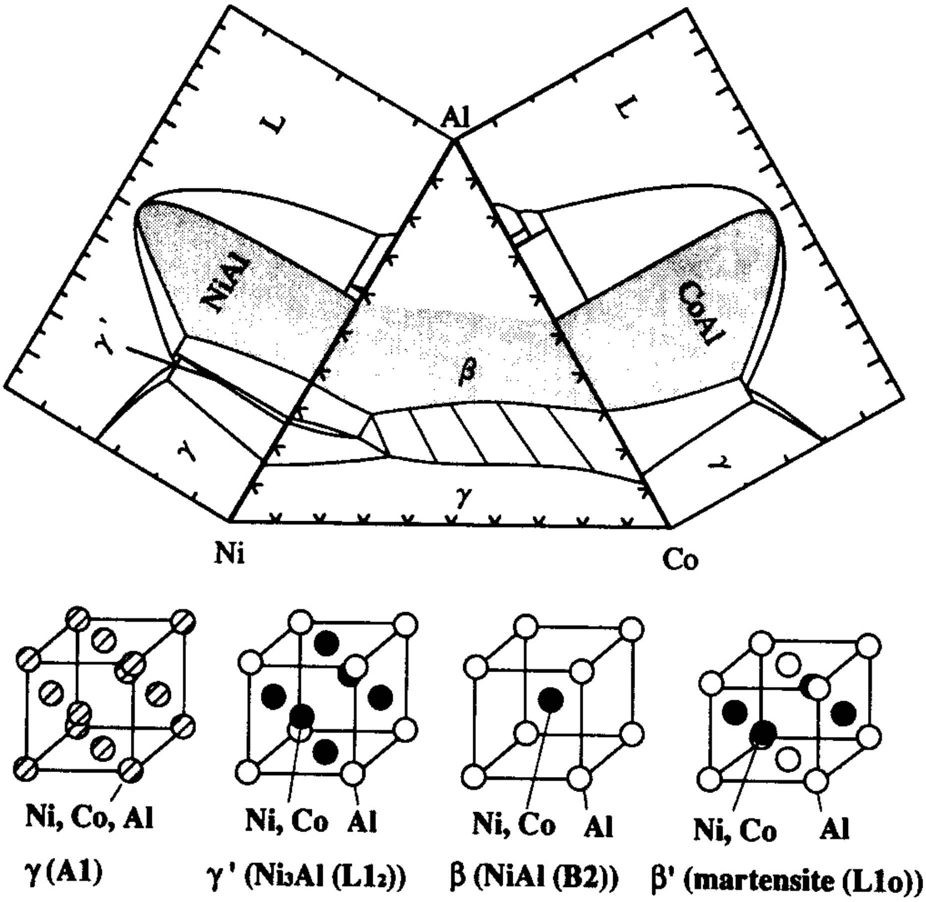

Figure 1.7: Phase equilibria in Co-Ni-Al system Kainuma *et al.* (1996)

the two-phase β/γ and β/γ' microstructures in the CoNiAl system. Similarly, a new Co-Ni-Ga β-base alloy system was developed and expected to have similar characteristics as the Co-Ni-Al β-base alloy, because: *a*) Ga and Al belong to column IIIb in the periodic table; and *b*) the β phase appears in a wide range of compositions in the Ni-Ga and Co-Ga binary systems and is in equilibrium with the γ phase in Co-rich and Ni-rich regions as shown in Figure 1.8. Fig. 1.8 shows the conjectural ternary phase diagram pieced by the Co-Ni, Co-Ga and Ni-Ga binary phase diagrams reported elsewhere Liu *et al.* (2006). Most importantly, the $\beta + \gamma$ two phase CoNiGa alloys, which exists over a large composition range

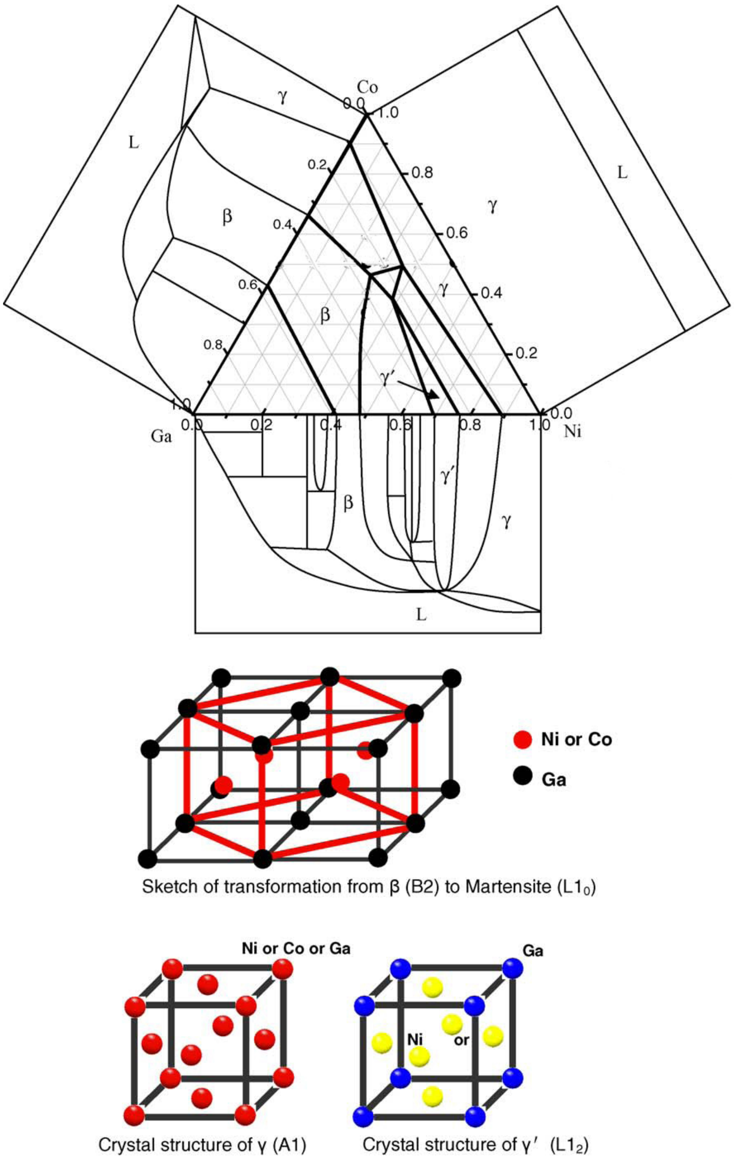

Sketch of transformation from β (B2) to Martensite ($L1_0$)

Crystal structure of γ (A1)

Crystal structure of γ′ ($L1_2$)

Figure 1.8: The designed two composition series in the CoNiGa schematic ternary diagram and crystal structure for each phase. The B2 ordered parent phase undergoes to the $L1_0$ martensite based on the Bain distortion model Liu *et al.* (2006)

(Fig. 1.8), are characterized by good ductility and wide range of transformation temperatures Oikawa *et al.* (2001, 2006). Moreover, the recent reports on CoNiGa alloys suggested that these alloys are promising HTSMA systems with M_s and A_f temperatures reaching as high as 200 and 350 °C, respectively, by adjusting the composition Liu *et al.* (2006); Ma *et al.* (2007); Schlagel *et al.* (2004).

From Figs. 1.7 and 1.8 and previous reports Brown *et al.* (2005); Oikawa *et al.* (2001), it can be understood that other than the austenitic and martensitic crystallograhpic structures, the solid-state transformations and the magnetic properties of Co-Ni-Ga alloys are similar to those in CoNiAl alloys. However, the resultant microstructures upon solidification of Co-Ni-Ga and Co-Ni-Al alloys are quite different according to the recent studies by Liu *et al.* (2005, 2006) and they attributed this behavior to different equilibrium reactions; Co-Ni-Ga system undergoes peritectic reaction ($L + \gamma \rightarrow \beta$), while Co-Ni-Al eutectic reaction ($L \rightarrow \beta + \gamma$). In addition, there are several studies describing the fundamental shape memory and pseudoelastic properties as a function of temperature and stress such as the transformation strains, Clausius-Clapeyron relation, stress and thermal hysteresis, and the influence of deformation history on the transformation behavior and cyclic stability at ambient temperatures Canadinc *et al.* (2007); Chernenko *et al.* (2004, 2007); Dadda *et al.* (2006a,b, 2008, 2009); Efstathiou *et al.* (2004); Hamilton *et al.* (2005, 2006); Karaca *et al.* (2003, 2004); Meyer *et al.* (2006).

Chapter 2

Material and Experimental Procedures

2.1 Material and Sample Preparation

Ingots of CoNiGa and CoNiAl with a nominal composition of 49Co-21Ni-30Ga and 38Co-33Ni-29Al (in at. %) were prepared using vacuum induction melting in an inert gas environment[1]. The composition of these alloy system was chosen in order to obtain a two phase $\beta+\gamma$ microstructure with β-matrix as the stable phase at high temperatures as shown in the phase diagrams in Figs. 1.7 and 1.8 on page 16 and17 in Chapter 1. The single crystals were grown using the Bridgman technique in a He environment. For compression experiments, specimens with dimensions of $4 \times 4 \times 8$ mm^3 were electro-discharge machined from the bulk single crystals such that their longer, i.e. compression axes, were along the [001],[123], [110] and [235] crystallographic orientations.

For the heat-treatments, the samples were kept in evacuated and argon filled quartz tubes in order to avoid oxidation and evaporation of any constituent elements. Solutionization of $Co_{38}Ni_{33}Al_{29}$ and $Co_{49}Ni_{21}Ga_{30}$ alloys was carried out at 1350 °C for 24 hours and 1200 °C for 4 hours followed by quenching in cold water, respectively. The aging of the $Co_{49}Ni_{21}Ga_{30}$ alloys was conducted at 900 °C for 24 hours and 1100 °C for 4 hours and then water quenched. Samples for

---

[1] This was carried out under the supervision of Prof. Y. Chumlyakov.

optical microscopy (OM) were prepared using standard silicon carbide grinding down to 4000 grit, followed by mechanical polishing with 1 μm diamond paste using Struers Red lubricant, and 0.02 μm OPS (Oxide (silica) polishing suspension) solution. Sometimes samples were etched to better bring out the γ-phase distribution in the β-matrix of both CoNiAl and CoNiGa alloys utilizing the etchant HCl (75 ml), ethanol (75 ml), 15 gr $CuSO_4$ and 15 ml water solution. Samples for Electron Backscattered Diffraction (EBSD) were first mechanically polished to 0.02 μm OPS as describe above, and subsequently twin-jet electro-polished with a 5 % perchloric acid and 95 % ethanol solution cooled to -25 °C; electro-polishing was carried out at 30 V for about 120 seconds. The removal of few microns (20-30 μm) of the surface layer by electro-polishing is necessary to remove any preparation-induced artifacts. For Transmission Electron Microscopy (TEM), 1 mm thick disks were sliced normal to the loading axis of the compression samples. Final thinning of mechanically polished 3 mm diameter disks was carried out by twin-jet electro-polishing with a 5 % perchloric acid and 95 % ethanol solution.

2.2 Thermo-mechanical Experiments

Two main types of thermo-mechanical tests were conducted to study the transformation behavior of $Co_{38}Ni_{33}Al_{29}$ and $Co_{49}Ni_{21}Ga_{30}$ alloys: i) isostress temperature variation experiments, and ii) isothermal monotonic or cyclic stress-strain tests. In the first case, depending on the test temperature range, heating/cooling was either achieved by direct flow of hot/cold nitrogen gas onto the samples or by induction heating for test temperatures above 200 °C (Figure 2.1). The heating/cooling rate was limited to 10 K/min, and thus, temperature variation along the sample could be restricted to a maximum of ± 2 °C. The isothermal stress-strain experiments that involved many cycles were conducted using an MTS servo-hydraulic load frame in displacement control with a fixed maximum strain upon loading and a fixed minimum stress for unloading at a strain rate of 1×10^{-3} s^{-1}, while those involved only one loading-unloading cycle (a monotonic test) were performed at a quasi-static rate of 6×10^{-5} s^{-1}. Strains were mea-

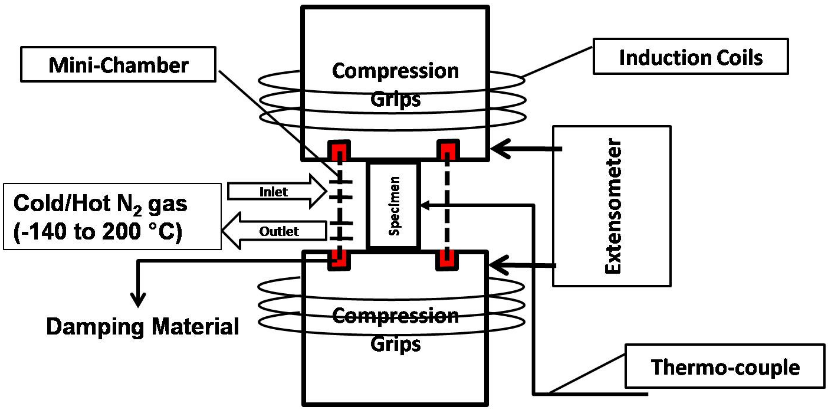

- **Sample dimension : 4 x 4 x 8 mm^3**

Figure 2.1: Experimental setup adopted for thermomechanical characterization under compressive loading conditions. This setup also allows one to perform *in-situ* microscopy at elevated temperatures when it is used without the mini-chamber shown in the schematic.

sured with a high-temperature MTS extensometer having a 12 mm gauge length attached to the compression grips.

2.3 Microscopy and Digital Image Correlation

In-situ microscopic observations were made to investigate the evolution of transformation at various stages during pseudoelasticity. Images were captured with a Keyence digital microscope model VH-500 with a resolution of 500 nm. A telezoom lens was used at 50 times magnification covering 5×4 mm^2 surface area. A full-field optical technique called digital image correlation (DIC) was carried out on the images of size 5×4 mm^2 to determine the local strain fields during loading and unloading. The DIC technique measures the displacement fields by tracking features on the specimen surface and to achieve this a surface with a random speckle patterns is the most common approach, which works well for DIC Chu *et al.* (1985). Speckle patterns with a speckle size in the range of 5 - 40 μm on a polished surface were achieved using an Efbe-Airbrush with the nozzle size of 0.15 mm from Friedrich Boldt GmbH. Commercially available Vic-2D software from LIMESS Messtechnik und Software GmbH was used to perform the image correlation and strain calculations.

To perform DIC, a region of interest is selected in the reference image and divided into small square regions with a defined number of pixels called subsets or subimages. Here the reference image stands for an image that is recorded in an undeformed state of the sample. An array of pixel intensities in each subset typically of size (2M + 1)×(2M + 1) pixels is registered and the regions with the same intensities are sought after in the deformed image. Here M is an integer referring to the given subset size. In order to find the location of a deformed subset, nonlinear optimization techniques are used in which displacements and displacement gradients are assumed. An iterative approach is used to adjust these assumed values until the difference in pixel intensity between the undeformed and deformed subsets is a minimum. In other words, a 2D cross correlation coefficient as a function of pixel intensity maps is defined and minimized in order to find the position of a corresponding deformed subset. This can be represented as follows:

$$r_{ij} = 1 - \frac{\sum_{i=-M}^{i=M} \sum_{j=-M}^{j=M} \left[F\left(x_i, y_j\right) - \bar{F}\right] \left[G\left(x_i^*, y_j^*\right) - \bar{G}\right]}{\sqrt{\left(\sum_{i=-M}^{i=M} \sum_{j=-M}^{j=M} \left[F\left(x_i, y_j\right) - \bar{F}\right]^2\right) \left(\sum_{i=-M}^{i=M} \sum_{j=-M}^{j=M} \left[G\left(x_i^*, y_j^*\right) - \bar{G}\right]^2\right)}} \tag{2.1}$$

Here F(x_i,y_j) and G(x_i^* ,y_j^*) are the grey values or the pixel intensities of the subset centered at the source and target point located in the reference and deformed images, respectively; $\bar{F}$ and $\bar{G}$ are the ensemble averages. The coordinates or grid points (x_i,y_j) and (x_i^* ,y_j^*) are related by the deformation that occurs between the two images. If the motion is perpendicular to the optical axis of the camera and a subset is chosen small enough, then the deformation can be assumed to be homogenous within the region, thus, the relation between (x_i,y_j) and (x_i^* ,y_j^*) can be approximated by a 2D affine transformation such as:

$$x^* = x + u + \frac{\partial u}{\partial x}\Delta x + \frac{\partial u}{\partial y}\Delta y \tag{2.2}$$

$$y^* = y + v + \frac{\partial v}{\partial x}\Delta x + \frac{\partial v}{\partial y}\Delta y \tag{2.3}$$

Here u and v are the admissible translation fields of the center of the subset in the X and Y directions, respectively (capital X and Y refer to the coordinate system in the deformed reference system). The distances from the center of the subset to the point (x, y) are denoted by Δx and Δy. Thus, the correlation coefficient r_{ij} is a function of displacement components (u, v) and their gradients, i.e. strain fields. These deformations of the reference subset commonly include rigid body motions and deformations as outlined in Figure 2.2. It should be noted that the aforementioned admissible deformation fields are referred only to the subset deformation not to the applied deformation of the sample. Further details of data analysis and general background on DIC can be found in Chu *et al.* (1985).

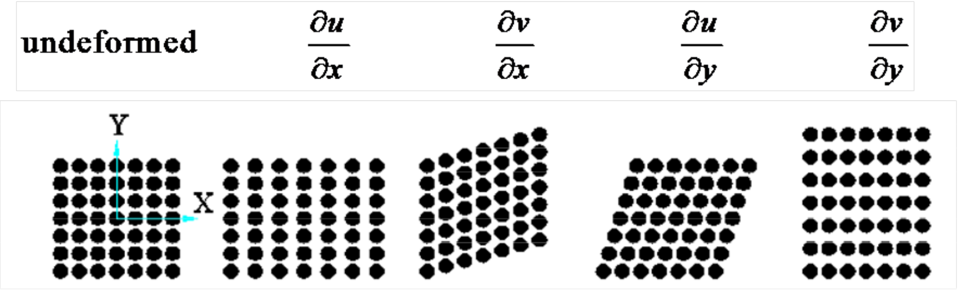

Figure 2.2: The pixels in the undeformed subset undergoing a variety of homogeneous deformations according to the deformation gradients shown above.

2.4 Electron Microscopy, DSC and SQUID

The samples were examined with a Philips CM 200 Transmission Electron Microscope (TEM) operated at a nominal accelerating voltage of 200 kV. An EBSD system in a Philips- XL 40 ESEM- scanning electron microscope (SEM) operated at nominal voltage of 20 kV was used to obtain orientation maps. EBSD measurements have been realized with an orientation imaging microscopy (OIM) system provided by TexSEM-Laboratories (TSL).

Differential scanning calorimetry (DSC) was performed on virgin and trained samples in order to determine the transformation temperatures and their evolution under stress-free conditions. A Perkin Elmer DSC cell was used in the temperature range of -100 to 300 °C at cooling/heating rates of 10 K/min, and all DSC measurements started by cooling until temperature reached -100 °C in order to ensure the sample was completely in martensitic state.

The phase transformation temperatures were also obtained through a Quantum Design Superconducting Quantum Interference Device (SQUID) magnetometer that utilizes the principle of magnetization change upon martensitic transformation Oikawa *et al.* (2001); Ullakko *et al.* (1996). A 3 °C/min heating/cooling rate was utilized during the SQUID experiments, in order to avoid rate effects.

Chapter 3

Characterization of Shape Memory Behavior in $Co_{38}Ni_{33}Al_{29}$ and $Co_{49}Ni_{21}Ga_{30}$ Alloys

3.1 Introduction

In Section 1.8 of Chapter 1 the motivation for the development of new Co-Ni-Al and Co-Ni-Ga HTSMA and MSMA systems has been described. However, their successful incorporation into industry requires a full comprehension of their thermoelastic martensitic transformation behavior and the resultant shape memory and pseudoelastic phenomena. In this chapter some of the results of the experimental investigations that involve isobaric thermal cycling and isothermal stress-strain experiments and incremental strains tests (ISTs) on $Co_{38}Ni_{33}Al_{29}$ and $Co_{49}Ni_{21}Ga_{30}$ (in at. %) single crystalline alloys are reported. The results demonstrate that i) the γ-phase volume fraction can be adjusted to achieve optimum SME, PE and TWSME properties in solutionized $Co_{38}Ni_{33}Al_{29}$ alloys subjected to different cooling rates and ii) the [001]-oriented as-grown $Co_{49}Ni_{21}Al_{30}$ single crystals exhibit pseudoelasticity at temperatures high above 300 °C marking them as promising candidates for high-temperature pseudoelastic material (HTPM).

3.2 Analysis of Results and Discussion

3.2.1 Stress-assisted Shape Memory Effect

$Co_{38}Ni_{33}Al_{29}$ single crystals solutionized for 24 hours at 1350 °C and cooled down in different media (water, oil and air) were used for this study. The typical microstructures achieved through utilizing the three cooling methods are illustrated in Figures 3.1 (a) to (c). The micrographs in the figure demonstrate significantly varying distribution and volume fraction of γ-phase in the β-matrix. It is observed that the volume fraction of the γ phase increases with decreasing cooling rate for all three orientations studied (Fig. 3.1) as this phase is stabilized at low temperatures Liu *et al.* (2005). It should be noted that the γ phase is relatively soft and enhances ductility Ishida *et al.* (1991); Kimura *et al.* (1994), which does not undergo phase transformation, even though it strongly affects the

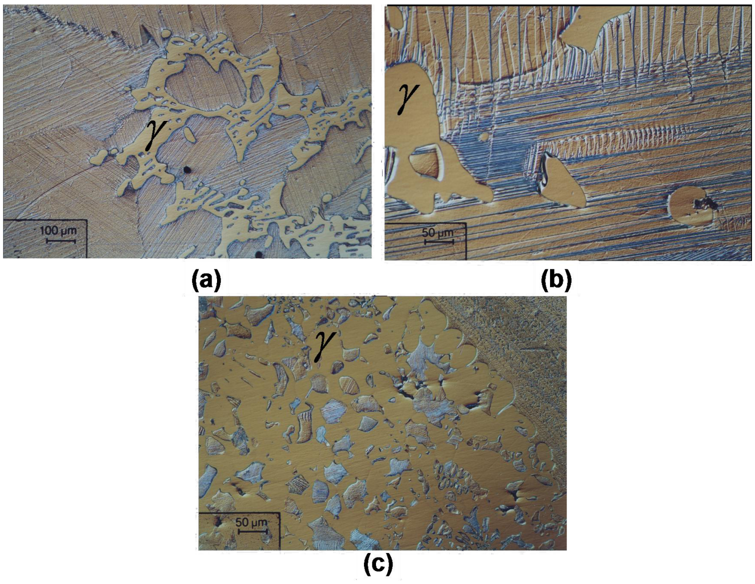

Figure 3.1: Optical micrographs of $Co_{38}Ni_{33}Al_{29}$ alloys showing the microstructures obtained through different cooling media following solutionization: (a) water quenched (WQ), (b) oil quenched (OQ), and (c) air cooled (AC). Canadinc *et al.* (2007).

phase transformation temperatures and the martensitic transformation behavior as it interacts with the moving phase fronts Efstathiou *et al.* (2004).

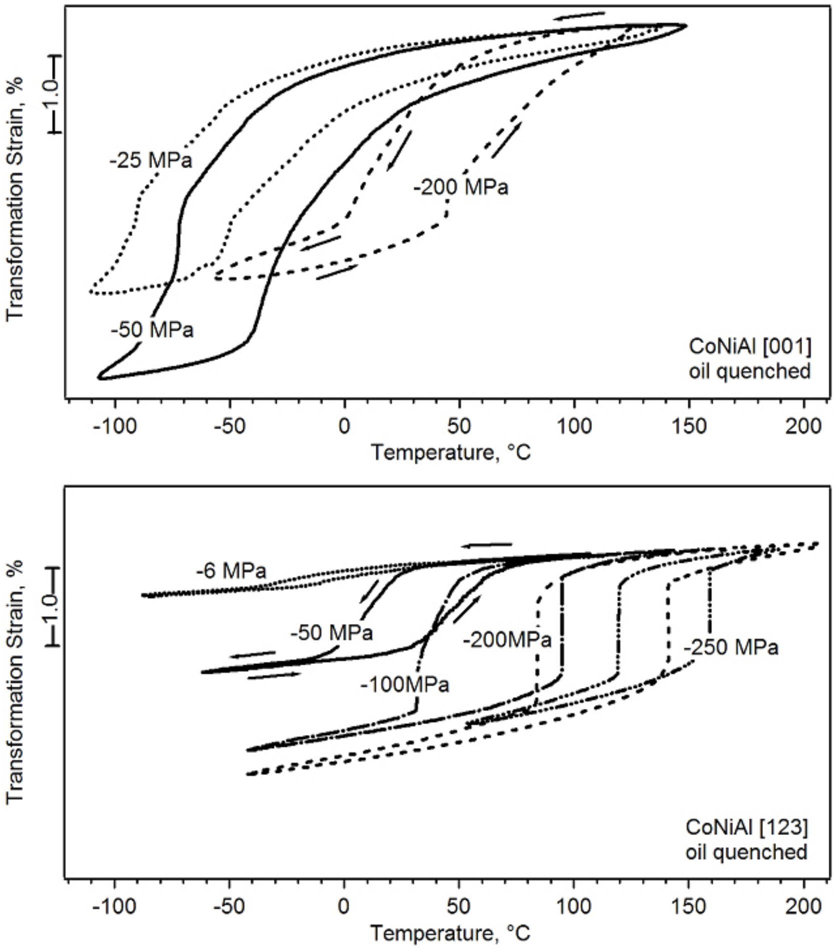

Figure 3.2: Strain-temperature response of $Co_{38}Ni_{33}Al_{29}$ single crystals under compressive loading. Three thermal cycles were conducted at each stress level, yet only the final cycles are shown here for the sake of clarity. Canadinc *et al.* (2007).

Results of the thermal cycling experiments carried out under various constant stress levels (Figure 3.2) brought several important points to attention. Moreover, thermal cycles shown in Fig. 3.2 were used to evaluate different shape-memory parameters including shape memory strains, thermal hysteresis and transforma-

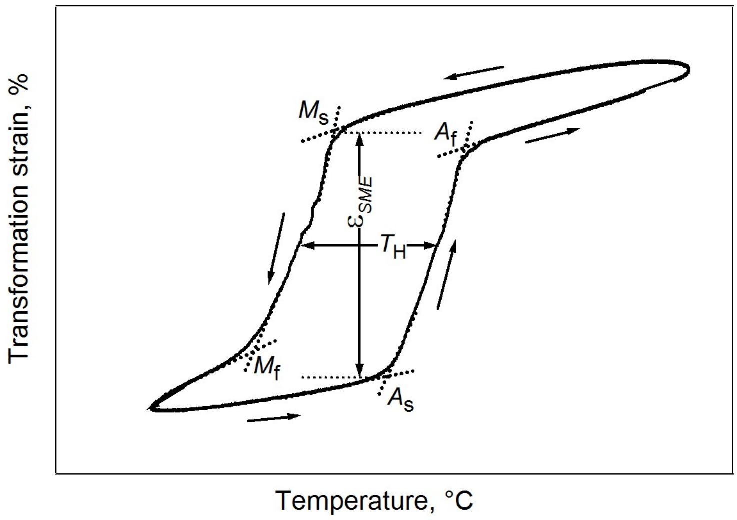

Figure 3.3: Schematic showing a typical isobaric strain-temperature curve under compression illustrating the definition of transformation temperatures (M_s, M_f, A_s and A_f) using intersecting slope-line method, and the vertical and horizontal widths of the loop are considered as transformation strains (ϵ_{SME}) and thermal hysteresis (T_H), respectively. The arrows indicate the cooling and heating paths of the loop.

tion temperatures as defined in Figure 3.3. These values were compared among the different oriented crystals with different microstructures (Fig. 3.1) to better estimate the functional performance of $Co_{38}Ni_{33}Al_{29}$ alloys. To start with, the [001]-oriented single crystals exhibit the highest recoverable transformation strains, which stand close to -yet slightly below- the theoretical CVP formation strain (ϵ_{CVP}) values, as stated in Table 3.1, which also displays the maximum transformation strain (ϵ_{SME}) for each single crystal and cooling rate, along with the corresponding Schmid factors for dislocation slip in the {110}<001> and {100}<001> systems (austenite), the resolved shear stress factors (RSSF), maximum recoverable PE strains (ϵ_{PE}), and maximum TWSME strains (ϵ_{TWSME}). The [110] orientation in some microstructural conditions, on the other hand, exhibits recoverable transformation strains exceeding their corresponding ϵ_{CVP}

values (Table 3.1). It should be noted that they were calculated considering only the transformable β-phase Karaca *et al.* (2004). The γ-phase does not undergo phase transformation: however, it obstructs the propagation of the phase front. Hence the reduced volume fraction of transformable phase in a dual phase (β+γ) microstructure (Fig. 3.1) reduces the maximum transformation strains.

Table 3.1: The resolved shear stress factors (RSFF), Schmid factors (SF), theoretical CVP formation strains (ϵ_{CVP}) (from energy minimization theory Karaca *et al.* (2003)), maximum transformation strain (ϵ_{SME}), maximum recoverable PE strains (ϵ_{PE}), and maximum TWSME strains (ϵ_{TWSME}) for each single crystal orientation and cooling rate. σ: Compressive stress; T: Temperature; N/A: Not available; AC: Air cooled; OQ: Oil quenched; WQ: Water quenched. Canadinc *et al.* (2007).

Crystallographic orientation	[001]			[123]			[110]		
RSSF	0.56			0.38			0.30		
SF	0			0.45			0.50		
ϵ_{CVP}(%)	4.8			3.1			2.4		
Cooling method	AC	OQ	WQ	AC	OQ	WQ	AC	OQ	WQ
ϵ_{SME}(%)@ σ_{opt}(MPa)	3.1 100	4.1 50	4.0 50	1.8 200	1.9 200	2.8 100	1.0 200	3.4 50	4.0 50
ϵ_{PE}(%)@ T(°C)	4.3 10	3.8 22	4.0 170	2.2 50	N/A	2.5 107	N/A	2.6 26	3.4 60
ϵ_{TWSME}(%) @4-6MPa	1.3	1.2	0.25	0.8	1.4	2.6	0.15	2.6	2.7

The orientation dependency of recoverable transformation strains is dictated by the RSSF, such that high RSSF values imply low transformation stresses and high recoverable transformation strains. Accordingly, the [110] orientation, which possesses a low RSSF, is expected to yield a low transformation strain. However, the experimentally determined transformation strain values for the OQ or WQ [110] samples are well above the ϵ_{CVP} values (Table 3.1). This clearly demonstrates the contribution of martensite detwinning to the overall strain. Specifically, compression along the [110] direction activates dislocations and the corresponding local stress fields create preferential nucleation sites for the most favorably oriented CVPs and help twin boundary motion. This, in turn, promotes the growth of a favorable single correspondence variant (SCV), giving way to detwinning strains, and thus increasing the overall transformation strain exhibited by the material. As for the [001] orientation, its zero Schmid factor theoretically eliminates the possibility for easy dislocation slip. The matrix resists dislocation slip and twin boundary motion, suppressing the detwinning in this orientation, which explains the transformation strains being lower than the corresponding ϵ_{CVP} values (Table 3.1).

Accordingly, the orientation dependence of the transformation strains is brought about by the orientation dependence of CVP activation and growth of a favorable SCV Hamilton *et al.* (2004); Meyer *et al.* (2006); Sehitoglu *et al.* (2000, 2001b). For instance, the [123] orientation in B2 phase NiTi alloys possess only one active CVP Sehitoglu *et al.* (2003), which should also be true for the B2 structured $Co_{38}Ni_{33}Al_{29}$ alloys. In fact, in the strain-temperature experiments, the [123] orientation $Co_{38}Ni_{33}Al_{29}$ single crystals exhibited low transformation strains (Table 3.1). The low RSSF value and dislocation activity coupled with the presence of the γ-phase in the [123] orientation offer more frictional resistance to the twin boundary motion, as well as to that of a CVP martensite structure into a SCV structure. Consequently, higher optimum training stress (σ_{opt}) Meyer *et al.* (2006) and lower transformation strains were obtained in this orientation. Furthermore, the results emphasize the need for texturing polycrystalline aggregates of the current material near the [001] and [110] poles with an optimum γ-phase volume fraction to achieve high transformation strains.

It is speculated that the transformation strains below the theoretical values displayed by the AC samples stems from the increased matrix strength due to γ' precipitation. The high matrix strength obstructs twin boundary motion and detwinning, as observed in peak-aged NiTi alloys Sehitoglu *et al.* (2000), where coherent precipitates increase the matrix strength suppressing transformation and/or detwinning at low stresses. Moreover, the single crystals that demonstrate higher dislocation activity, such as the [110] and [123] orientations, further exhibit reduced transformation strains due to increased dislocation density in the untransformed austenite regions, which in turn increases the matrix strength. This idea is supported by the lower transformation and TWSME strains, and high σ_{opt} values exhibited by the [110] and [123]-oriented AC single crystalline samples (Table 3.1). With regards to the AC [001] samples, the higher ϵ_{SME} and ϵ_{TWSME} in the AC [001]-oriented single crystals (Table 3.1) can be attributed to the lack of substantial dislocation slip in the matrix and the nucleation and growth of specific favorable martensitic variants aided by stress fields around γ - β boundaries, the presence of γ' precipitates, and the growth of variants trapped at the γ - β boundaries.

The OQ and WQ samples, which possess a lower volume fraction of ductile γ-phase compared to AC samples (Fig. 3.1), exhibit higher ϵ_{SME} and ϵ_{TWSME}. This is attributed to the high volume fraction of transformable β-phase, offering lower frictional resistance to the mobility of phase fronts and thereby facilitating growth of favorable variants. However, the [001] oriented WQ crystals exhibit lower ϵ_{TWSME} despite the high ϵ_{SME} they display. The absence of local stress fields due to dislocation arrays, or secondary phase, such as the γ-phase, is responsible for this difference in the case of the [001] orientation.

Other important facts revealed by the iso-stress strain-temperature experiments (Fig. 3.2) include a gradual variation in strain at the transformation temperatures at low stress levels in the [123] orientation, abrupt variation in strain at the transformation temperatures in the same orientation at high stress levels, a gradual strain-temperature response instead of an abrupt transition in the other orientations ([001] and [110]) at all stress levels, and a wider thermal hysteresis in the case of the [123] and [110] orientations than in the [001] orientation. All of the observations revealed by the iso-stress strain-temperature experiments can be rationalized on the basis of various energy contributions to the overall free energy of the system during phase transformation. For instance, at low stress levels the volume fraction of self-accommodating groups of martensite CVPs grows, and increases the interfacial energy due to variant-variant interaction. The variant-variant interaction, γ-martensite phase interaction and elastic strain raise the stored elastic energy of the system. The elastic strain energy due to various forms of interactions provides opposition to the forward transformation, and thus, further transformation requires additional undercooling, leading to a gradual flow of the strain-temperature curves as shown in Fig. 3.2. As the stress levels increase, formation of the most favorably oriented CVPs in expense of unfavorable ones results in a decrease in the stored elastic energy. An abrupt transition occurs when the stored elastic energy is dissipated by relaxing coherency strains of martensite-austenite interfaces Hamilton *et al.* (2004) under higher stress levels.

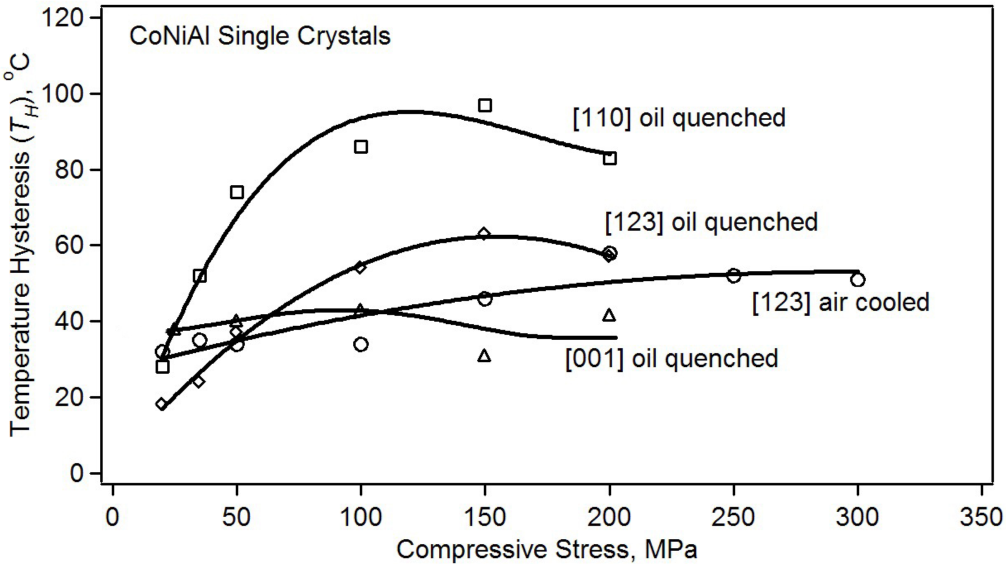

Figure 3.4: Evolution of thermal hysteresis with applied stress. Canadinc *et al.* (2007).

In the [123] and [110] orientations, relaxation of coherency strains occur by introducing dislocations upon the application of stress. Therefore, [110] and [123] orientations display abrupt transition at high stress levels, whereas the [001] orientation does not respond similarly. As a result of stored elastic energy dissipation in the [123] and [110] orientations, less elastic energy is available to assist the reverse transformation. Therefore, increased chemical driving force is necessary (resulting in an increased A_s) to initiate and complete the reverse transformation, which widens the thermal hysteresis (Figures 3.2 and 3.4). In the [001] orientation, on the other hand, stored elastic energy helps the reverse transformation, reducing the thermal hysteresis (Fig. 3.4). It should be noted that the thermal hysteresis of $Co_{38}Ni_{33}Al_{29}$ alloys studied in this work is greater than those exhibited by NiTi and NiTiCu alloys Hamilton *et al.* (2004); Sehitoglu *et al.* (2001b, 2003). Large thermal hysteresis can be exploited in applications that require high damping capacity and shape stability, while smaller thermal hysteresis is more essential for actuators Mosley & Mavroidis (2001). Thus, crystals with [001] orientation would perform better in actuation applications, whereas [110] and [123] orientations are more suitable for applications demanding higher damping capacity.

Transformation strain and thermal hysteresis evolutions with stress observed in the present study are different from what has been reported so far for conventional SMAs such as NiTiCu Sehitoglu *et al.* (2001b) and NiTi Hamilton *et al.* (2004); Sehitoglu *et al.* (2000, 2003). At low stress levels, the martensite morphology is self-accommodating, and imparts low transformation strains. Consequently, CVP interactions and variant-second phase interactions raise the stored elastic energy contributing to the reversible form of free energy of the system, which in turn helps reverse transformations, thus lowering the thermal hysteresis. As the external stresses are increased, the growth of favorable martensite variants gives way to reduced interaction energies, and thereby increased transformation strains. The concomitant decrease in stored elastic energy by relaxation of coherency strains increases the difficulty of reverse transformation. As a result, more energy is required, as evidenced by the increase in temperature hysteresis. The results in Figs. 3.2 and 3.5 for the [001]-oriented OQ single crystals demonstrate that both the maximum transformation strain and the maximum temperature hysteresis occur at approximately the same stress level (σ_{opt}). The maximum transformation strain is obtained when a multivariant martensite (A and B in schematic of Fig. 3.5) transforms into a single variant martensite (C in the schematic of Fig. 3.5) in an ideal condition. Therefore, a martensite structure with a single variant is expected at 4.1% strain (C in the schematic of Fig. 3.5). With further thermal cycling upon attaining a maximum value, increased stress levels decrease the thermal hysteresis, as well as the transformation strains. The decrease in transformation strains is attributed to the formation of a twinned

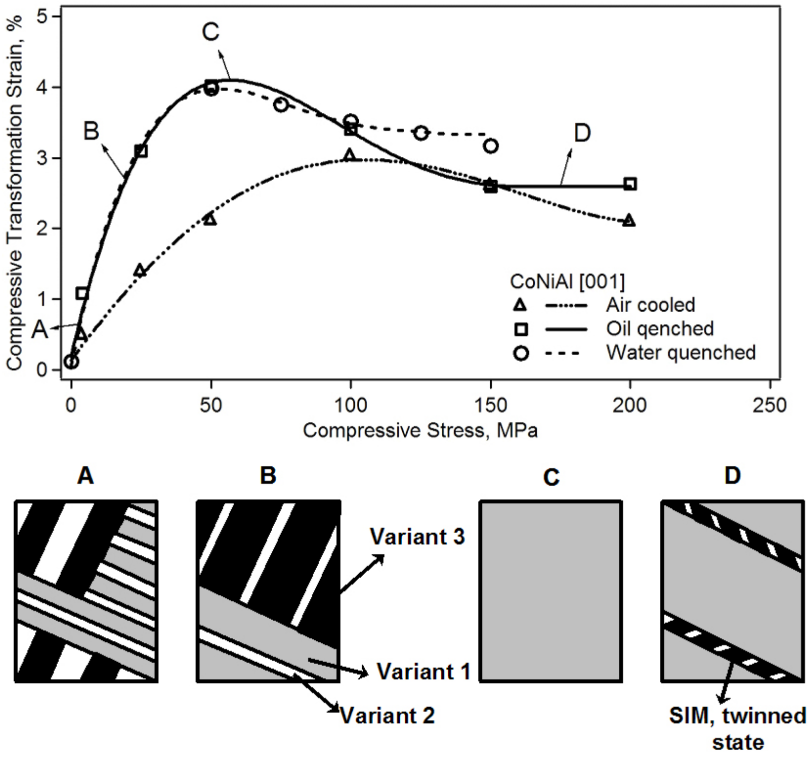

Figure 3.5: Demonstration of transformation strain evolution with compressive stress as a function of cooling rate. Potential twinning of variants is not shown in the schematics of microstructure states A and B. Canadinc *et al.* (2007).

state of SIM within the thermoelastic martensite to relax strain energy or introduction of dislocations, which interrupt the phase or twin front propagation. This state of martensite promotes the interaction between SIM and thermally-induced martensite, or oriented martensite variants due to the internal stresses, and results in an increased elastic energy, and thus reduces the temperature hysteresis.

In the case of $Co_{49}Ni_{21}Ga_{30}$ alloys, as-grown crystals were used and whose general microstructure is shown in Figure 3.6. The micrograph in the figure displays the uniform distribution of fine γ precipitates in the β-matrix. Owing to the slow cooling rates that have prevailed during the growth of single crystals using the Bridgman process, one would expect precipitation of γ phase in $Co_{49}Ni_{21}Ga_{30}$ alloys as the γ phase-field stabilizes at lower temperatures Liu *et al.*

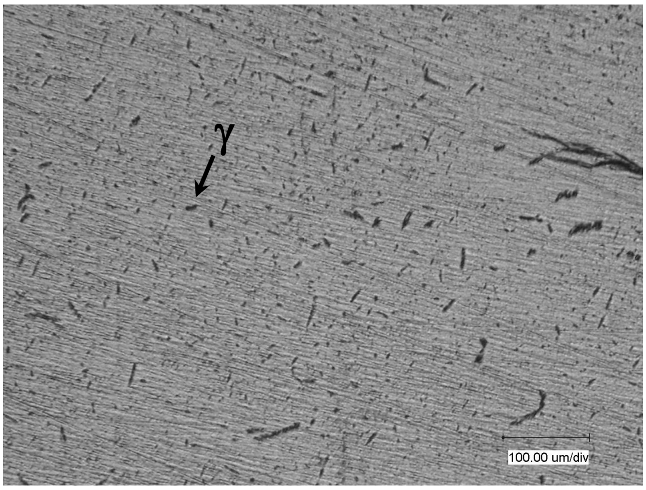

Figure 3.6: A microstructural overview of an as-grown $Co_{49}Ni_{21}Ga_{30}$ crystal showing the fine γ precipitates in the matrix.

(2006). The transformation temperatures of as-grown $Co_{49}Ni_{21}Ga_{30}$ single crystals were determined through differential scanning calorimetry (DSC) as shown in Figure 3.7. Accordingly, A_s, A_f, M_s, M_f are -2.4, 1.3, -18 and -22.4 °C, respectively. A stress-free thermal hysteresis, T_H, of only 20 °C is present in this material. Such a narrow hysteresis indicates the high degree of compatibility between austenite and martensite in these alloys. The strain-temperature response of [001]-oriented $Co_{49}Ni_{21}Ga_{30}$ single crystals under constant compressive stress (Figure 3.8) revealed that the phase transformation occurs in a rather abrupt manner at low stress levels (e.g. -4 MPa), accompanied by a low thermal hysteresis. Yet higher levels of applied compressive stresses bring about a completely different picture, such that a wider thermal hysteresis is present (Fig. 3.8). Moreover, substantial undercooling and overheating are indispensable for the completion of the forward and backward phase transformations, respectively. This difference in strain-temperature response due to change in applied stress levels stems from the fact that the frictional dissipation during phase transformation increases with increasing external stresses. It should also be noted that the difference between the transformation temperatures obtained from DSC and strain-temperature experiments results from a possible heterogeneity in the chem-

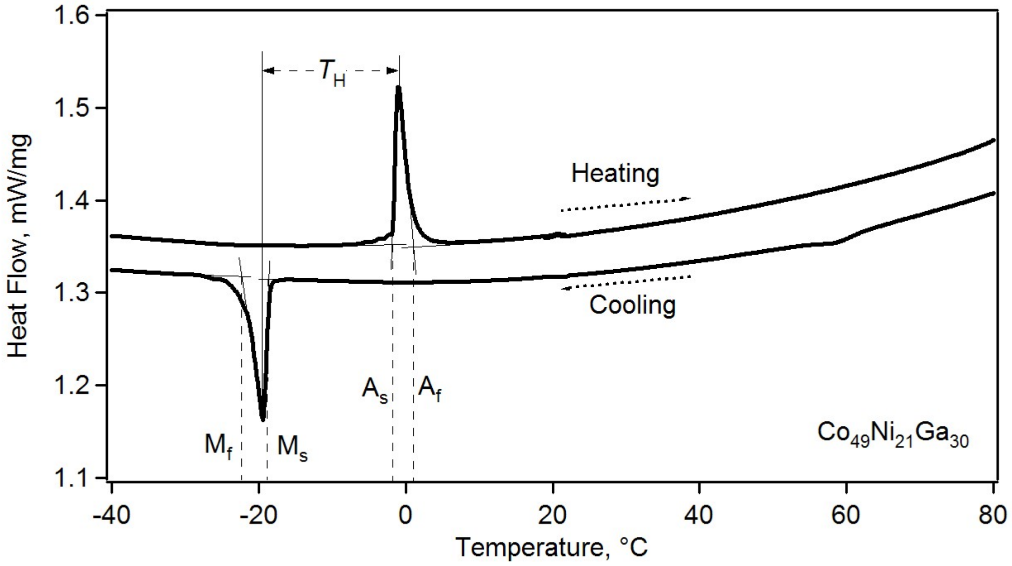

Figure 3.7: DSC curve of $Co_{49}Ni_{21}Ga_{30}$ alloy, showing the A_s, A_f, M_s and M_f temperatures, and the thermal hysteresis (T_H) brought about by stress-free thermal cycling. Dadda *et al.* (2006a).

ical composition. Specifically, the samples utilized in DSC are much smaller in size compared to the specimens used in strain-temperature tests. While the large specimens reflect the average response, even a small inhomogeneity in the composition could lead to large effects in a small DSC sample. Moreover, the material utilized in this study was as-grown, and this could cause inhomogeneities in the bulk.

Fig. 3.8 demonstrates that both the transformation strain and temperature hysteresis evolve with externally applied stress. The increase in thermal hysteresis is not drastic above stress levels of 50 MPa, and the saturation is reached at 150 MPa and higher stresses. The transformation strain of 4.7 % at 4 MPa applied stress decreases with increasing stress levels, converging to a saturation value of 3.5% at applied stress levels of 150 MPa and above. Interestingly, the response at low stress levels differs significantly from that observed in [001]-oriented $Co_{38}Ni_{33}Al_{29}$ single crystals *cf.* Figs. 3.2 and 3.5, indicating expressively lower critical stress levels for the $Co_{49}Ni_{21}Ga_{30}$ alloy in comparison to $Co_{38}Ni_{33}Al_{29}$.

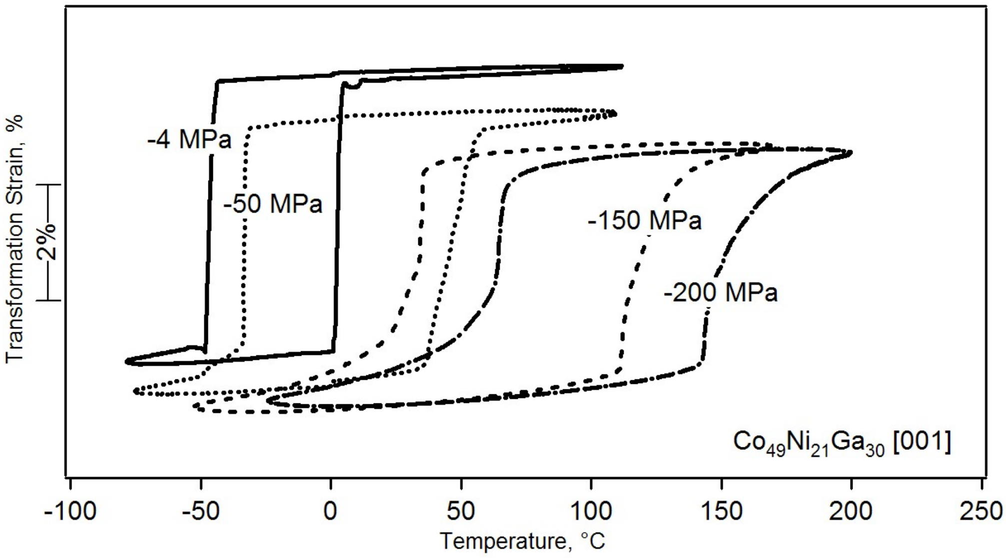

Figure 3.8: Isostress strain-temperature behavior of [001] oriented $Co_{49}Ni_{21}Ga_{30}$ single crystals. The scale bar on the strain axis is used instead of a conventional scale to avoid misunderstanding as the curves were shifted vertically from their original position for the sake of a clear presentation. Dadda *et al.* (2006a).

The abrupt phase transformation at lower applied stress levels (-4 MPa) in Fig. 3.8 suggests the nucleation and growth of a single variant, thereby reducing the interaction between the CVPs. Moreover, an external stress of about -4 MPa gives way to a transformation strain of about 4.3 %, which is the transformation strain from single crystal austenite to single crystal martensite according to theoretical calculations made elsewhere Dadda *et al.* (2008).

As for the higher stress levels (150 MPa), however, the transformation does not occur abruptly, but takes place in a gradual manner (Fig. 3.8) due to the difficulty in forward transformation brought about by the increased interaction between the thermally-induced and stress-induced martensitic variants. Figure 3.9 illustrates martensitic variants grown in several directions, which shows an example to this statement, where interaction between these differently oriented martensitic variants takes place. Consequently, the martensite is expected to possess a partial self-accommodating structure at these stress levels, where thermally- and stress-

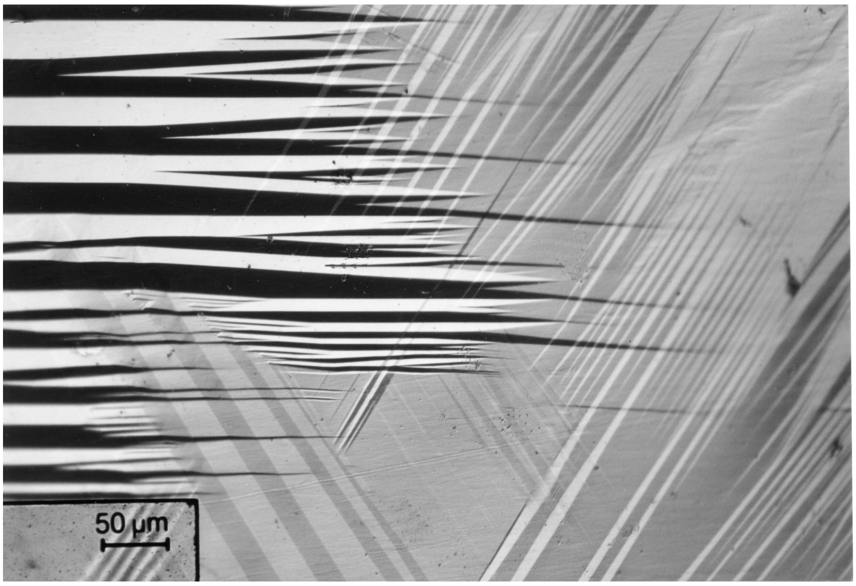

Figure 3.9: The residual martensite plates that grew in different directions in a trained/deformed sample. Dadda *et al.* (2006b).

induced variants coexist. This is supported by the observed decrease in transformation strain with increasing stress level (Fig. 3.8), which is again consistent with the microstructural model proposed earlier to understand the variation of transformation strains with the applied stress in Fig. 3.5 for $Co_{38}Ni_{33}Al_{29}$ alloys. On the other hand, the increase in thermal hysteresis is associated with the mechanical stabilization of martensite, leading to the reverse transformation at elevated temperatures Picornell *et al.* (2001). Further elaboration, such as in-situ observations of the microstructural changes, is necessary in order to draw a solid conclusion regarding this point.

3.2.2 Pseudoelasticity

Figure 3.10 shows a typical pseudoelastic response of the Co-base alloys used in this study. The figure is used to define several pseudoelastic parameters such as the critical stress levels for the forward, σ_{cr}^{For}, and the reverse, σ_{cr}^{Rev}, transformations, which were evaluated using the intersecting slope lines method at the inflection points where the deviation from initial linearity occurs both during loading and unloading. The stress hysteresis, $\Delta\sigma$, was measured at the half of the applied strain range ($\Delta\epsilon$). The strain, ϵ_0, is due to elastic deformation of austenite, while ϵ_T is the transformation strain. These parameters are useful in the analysis and discussion of pseudoelastic response of $Co_{38}Ni_{33}Al_{29}$ and $Co_{49}Ni_{21}Ga_{30}$ alloys as a funciton of crystallographic orientation and thermomechanical treatments as follows.

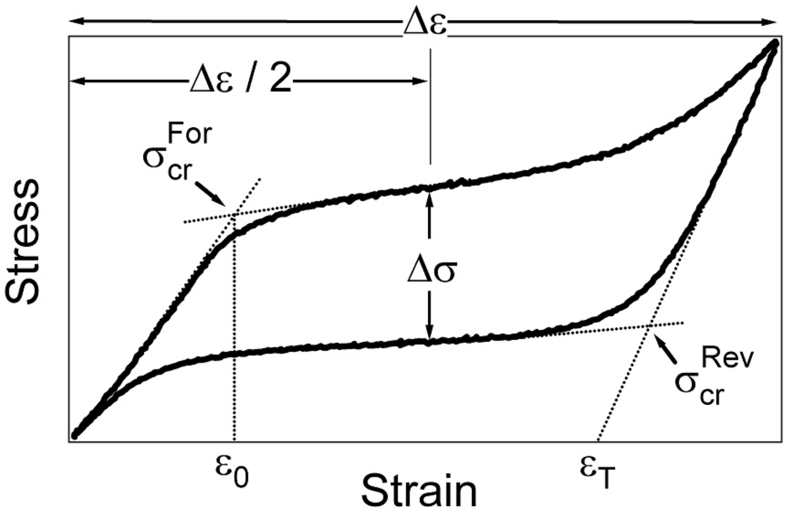

Figure 3.10: A typical pseudoelastic response showing the loading-unloading curves used to define the PE parameters.

Figures 3.11 and 3.12 lay out the orientation and cooling rate dependencies of the pseudoelastic behavior of the $Co_{38}Ni_{33}Al_{29}$ single crystals studied. It should be noted that the general trend in stress-strain behavior of the [110] and [123] orientations resembles that of CoNiAl polycrystals Karaca *et al.* (2003). It was proposed by Karaca *et al.* (2003) that the second stress drop at the end of the plateau region in CoNiAl polycrystals indicates a two-stage martensitic transformation. A similar response is observed for the [110] oriented crystals investigated in this study (Fig. 3.11).

The alteration of the critical stress in the [110] orientation with increasing deformation (Fig. 3.11) is linked to the role of irreversible mechanisms, such

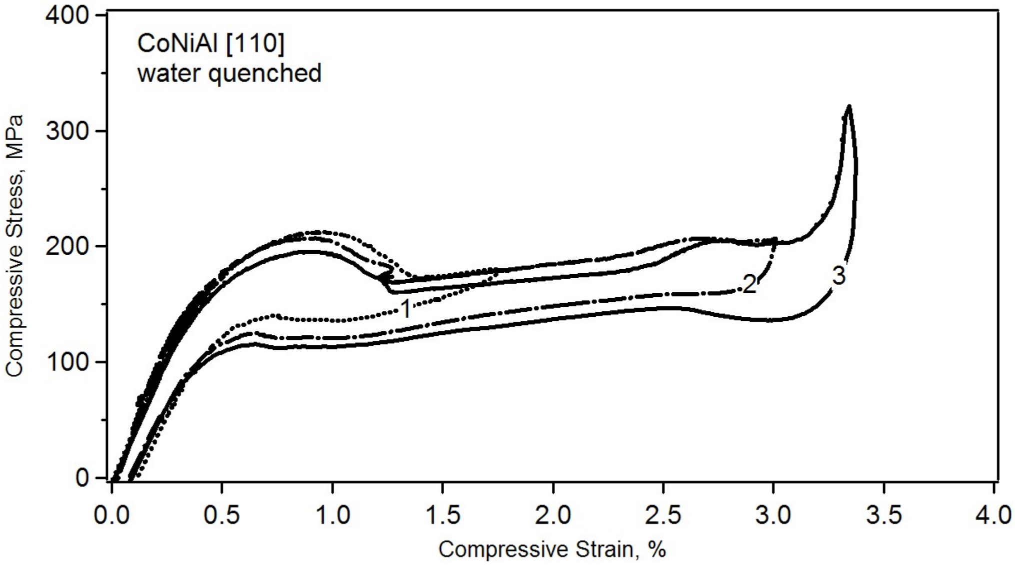

Figure 3.11: Pseudoelastic response of [110]-oriented WQ $Co_{38}Ni_{33}Al_{29}$ single crystals at 60 °C. Canadinc *et al.* (2007).

as dislocation generation and formation of residual martensite, which assist the forward transformation in subsequent cycles Efstathiou *et al.* (2004); Hamilton *et al.* (2006); Karaca *et al.* (2004). Interestingly, the critical stresses are quite stable for increasing strain levels in the [123] orientation (Fig. 3.12), where the irreversible mechanisms play a less pronounced role. Furthermore, stress hysteresis increases slightly with increased strain levels in all orientations (Figs. 3.11 and 3.12), which can be attributed to defect generation coupled with frictional dissipation. For instance, compression tests on the [001]-oriented single crystals revealed large stress hysteresis despite the lack of significant dislocation activity. Earlier studies confirmed that compression along the [001] orientation activates a relatively higher number of variants Hamilton *et al.* (2004). In such a case, the stress hysteresis is governed by multi-variant interaction, i.e. by variants that are preferentially oriented along the applied stress direction (SIM) and variants oriented in accordance with the internal stress fields, and interaction of moving phase fronts with the γ-phase. Another contribution to the large stress hysteresis in the [001]-oriented crystals comes from the high resistance against dislocation

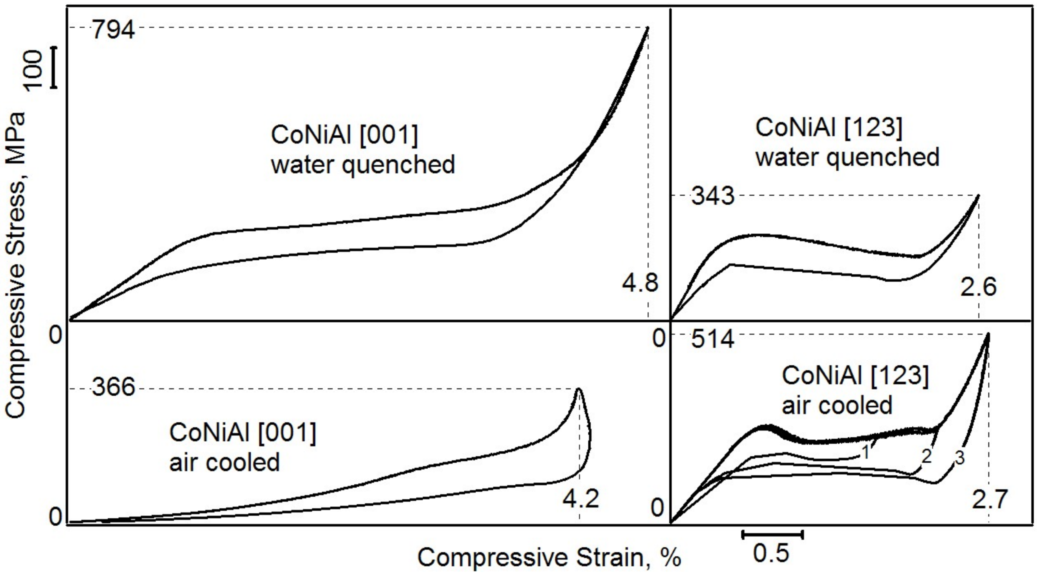

Figure 3.12: The pseudoelastic response of [001] (at 170 °C for WQ and at 60 °C for AC) and [123] (at 107 °C for WQ and at 33 °C for AC) oriented $Co_{38}Ni_{33}Al_{29}$ single crystals. The curves are plotted with identical scales to allow for comparison of the actual stress-strain response. The negative slope at the start of the unloading part of the AC [001] curve stems from an extensometer effect due to a short instability upon quick release of the load. Canadinc *et al.* (2007).

slip in the matrix, which suppresses twin boundary motion and detwinning. This in turn increases variant-variant interaction, leading to a high stress hysteresis. Such interaction reflects as an ascending flow curve in the stress-strain response, rather than a plateau typically observed in conventional SMAs. Consequently, the propagation stress change per unit strain in stress-strain response is higher in the case of the [001] orientation in comparison to the [110] and [123] orientations. Nevertheless, the slip activity and local stress fields in the [110] orientation create nucleation sites for favorable CVPs and promote the growth of a SCV, altering the variant-variant interactions. Hence in the [110] and [123]-oriented samples, low stress hysteresis is primarily due to local plasticity, instead of the variant-variant interactions.

One more remark regarding the pseudoelastic response of the [001]-oriented samples is that this orientation attains large PE strains even in the absence of pronounced dislocation activity and detwinning strains. This observation is associated with the high RSSF and easy reorientation of variants in the direction of the external stress. Moreover, the similarity between PE strains and transformation strains indicate the similarity between CVPs in SIM and thermally-induced martensite CVPs.

As stated earlier, compression along the [123] direction in B2 crystals activates only one CVP, altering the interaction among the variants. In this case, the availability of favorable variants to the local stress fields is minimized, reducing transformation strains or detwinning strains, as evidenced by the experimental results on [123] oriented single crystals (Table 3.1). The ascending stress-strain curve displayed by [123] oriented AC samples is linked to the interaction of twin boundary or moving phase fronts with γ' precipitates or γ-phase boundaries (Fig. 3.12). By contrast, the lack of variant-variant interaction, low volume fraction of γ-phase and absence of γ' precipitates in WQ [123] oriented crystal brings about very low resistance to mobile twin boundary or phase front, resulting in a descending stress-strain curve (Fig. 3.12).

In B2-structured alloys, the low critical transformation stress, high slip resistance and B2 atomic ordering allow for excellent transformation recoverability when loaded in the [001] direction as seen in the case of $Co_{38}Ni_{33}Al_{29}$ alloys discussed above and NiTi alloys by Sehitoglu *et al.* (2000). Thus, it became a common approach to characterize the [001]-oriented crystals first and then evaluate the effect of crystallographic orientation on the transformation and deformation behaviors in order to develop a strong textured material.

Figure 3.13 shows the pseudoelastic response of $Co_{49}Ni_{21}Ga_{30}$ [001]-oriented crystal at different temperatures. The crystal exhibited the PE strains of about 4.3 % at low temperatures ($\leq$ 120 °C) and altered strains of about 3 % at higher temperatures. The latter can be attributed to the formation of self-accommodating martensite at higher temperatures as the prevailing high stress levels have the tendency to induce a higher number of martensite variants. This increases the variant-variant interaction, which in turn will result in an ascending loading plateau at elevated temperatures as seen in Fig. 3.13. This will be discussed in detail later in Chapter 4 with *in-situ* observations at high temperatures.

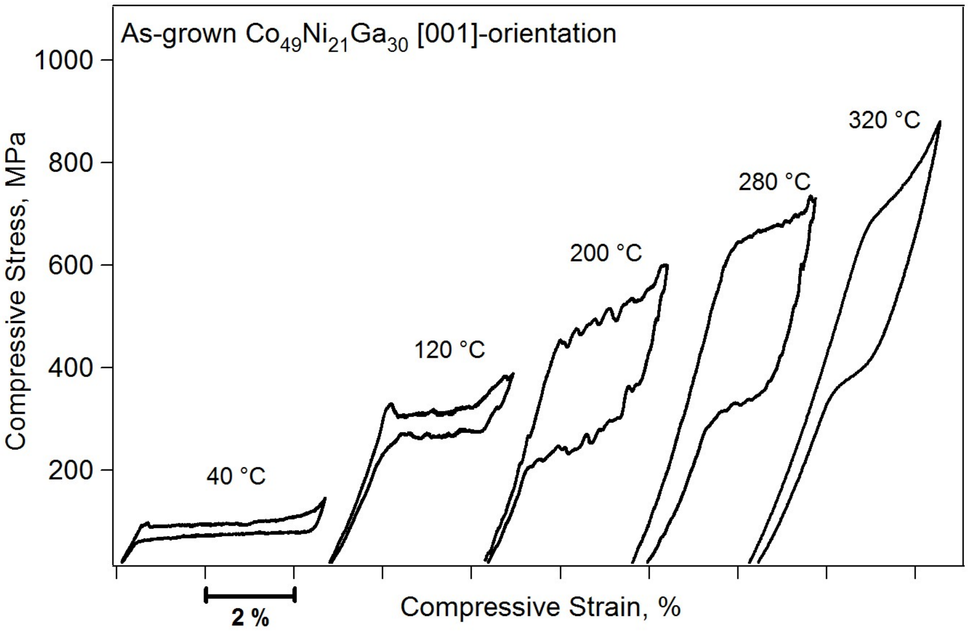

Figure 3.13: Pseudoelasticity and its dependency on temperature in an as-grown [001]-oriented $Co_{49}Ni_{21}Ga_{30}$ single crystal.

Figure 3.14 shows the stress-strain curves of [235]-oriented $Co_{49}Ni_{21}Ga_{30}$ crystal where the test temperatures were raised progressively up to 200 °C. It is clear from the figure that Lüder's type deformation prevails in this orientation. This type of behavior generally takes place in SMAs when the resistance to the transformation interface propagation is lower than that to the nucleation of martensite Canadinc *et al.* (2007). Lüder's type behavior is also observed during the reverse transformation, i.e. upon unloading the reverse transformation of SIM begins with a lower stress (the point where the unloading curve changes its slope) and is followed by an increase of the stress to a higher plateau level. The SIM transformation starts as soon as the stress-strain curve deviates from linearity and a first transformation band appears. The upper limit of the Lüder's type deformation marks the moment when this band has spread over the entire cross section

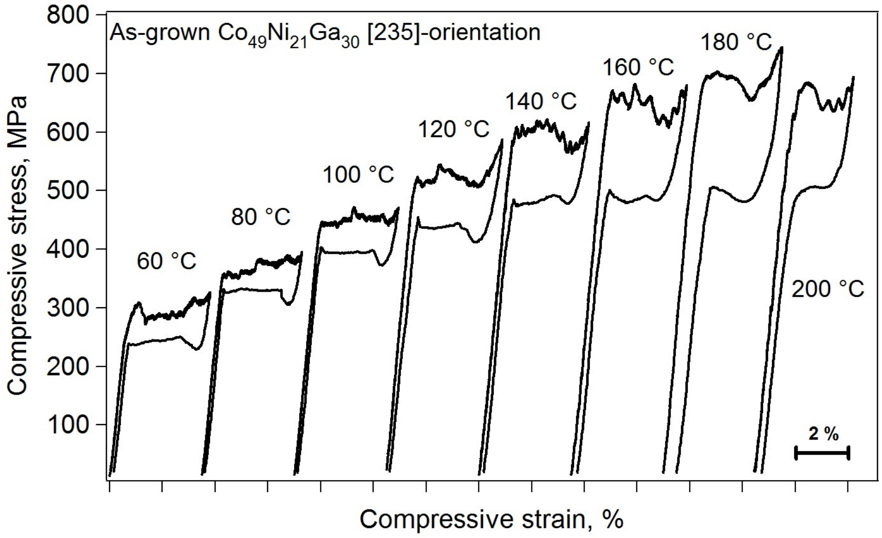

Figure 3.14: Pseudoelastic response of [235]-oriented $Co_{49}Ni_{21}Ga_{30}$ single crystal as a function of temperature. Dadda *et al.* (2009).

of the specimen Liu *et al.* (1995). As the band reaches the free surface of the sample a portion of the elastic energy stored during its growth is released, resulting in a decrease in the resistance to the propagation of the band interface Liu *et al.* (1995). This decreases the plateau stress to lower levels causing the typical Lüder's type deformation. Moreover, the *in-situ* and DIC studies in the next Chapter 4 will reveal that the each stress rise (other than the first upper limit) in the plateau region corresponds to the formation of a new transformation interface (band) every time. Similarly, the lower stress limit for the reversion of the martensite during unloading indicates the point when the propagating austenite band reaches the free surface of the specimen, instead of being associated with the nucleation of austenite Liu *et al.* (1995). Finally, the irrecoverable strains at elevated temperature ($\geq$ 180 °C) that limit the sample to exhibit any further perfect pseudoelasticity in Fig. 3.14 are linked to the martensite stabilization coupled with the plastic accommodation in the material due to the high prevailing stresses.

Figure 3.15 shows the σ_{crit}^{For} values (see the definition in Fig. 3.10 on page

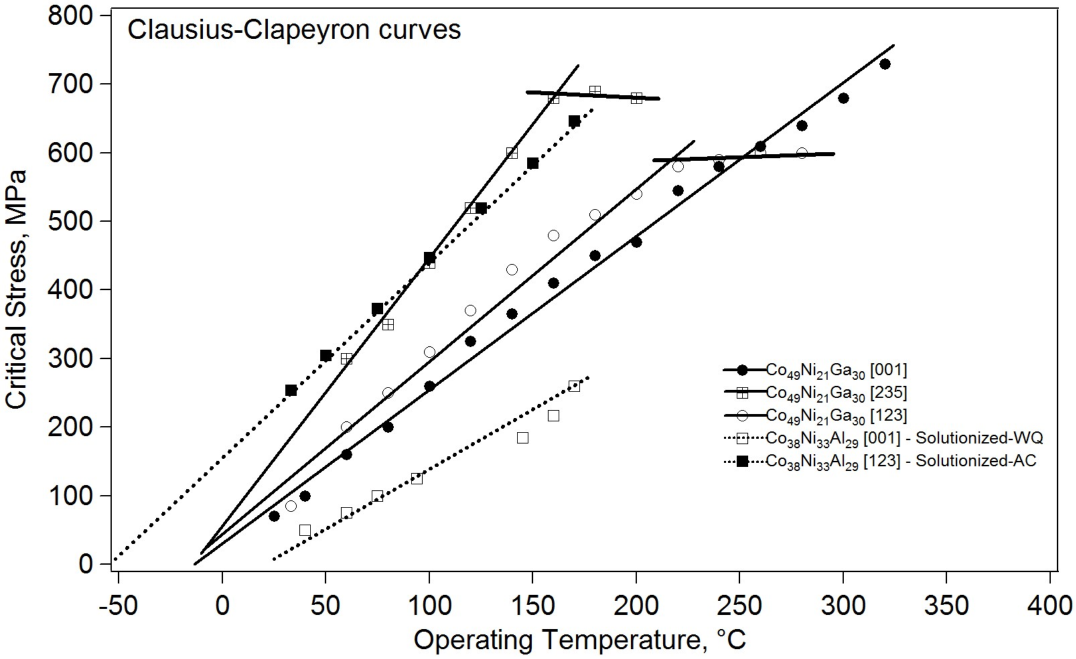

Figure 3.15: The representation of PE temperature ranges in terms of Clausius-Clapeyron (CC) curves for $Co_{49}Ni_{21}Ga_{30}$ and $Co_{38}Ni_{33}Al_{29}$ alloys. All the $Co_{38}Ni_{33}Al_{29}$ alloys in the figure are solutionized and the curves are represented by dashed curves, while solid curves refer to the $Co_{49}Ni_{21}Ga_{30}$ alloys.

39) obtained for both the alloys as a function of test temperature. The linear curves follow the CC-relationship (Eq. 1.3 on page 11) and some of the curves deviate from the linearity, for instances, in the case of [235] and [123]-oriented $Co_{49}Ni_{21}Ga_{30}$ alloys. This deviation was attributed to the plasticity by dislocation slip in the material that occur prior to SIM transformation Dadda *et al.* (2006b). It should be noted here that all the CC-curves of as-grown $Co_{49}Ni_{21}Ga_{30}$ crystals converge almost to the same point when they are extrapolated to the zero stress level on the abscissa, which is considered as the M_s temperature (-20 °C) under stress free conditions. This is in good agreement with that evaluated using DSC measurements in Fig. 3.7. The temperature ranging from M_s to the point where the curves depart from linearity is considered as the PE range in Fig. 3.15 (*cf.* Fig. 1.6). The different values of M_s temperatures for $Co_{38}Ni_{33}Al_{29}$ single crystals

in Fig. 3.15, 20 and -60 °C for WQ and AC, respectively, is associated with the variation in chemical composition of the matrix, which is in turn because of the differences in the amount of precipitation (Fig. 3.1).

Fig. 3.15 also demonstrates that the CC-slope of [001]-oriented crystals is always lower than for the other orientations. In other words, the [001] orientation tends to undergo SIM transformation in a much easier fashion than the [123] and [235] orientations for a given temperature. This difference purely stems from the crystallography and depends on Schmid's law where the initiation of SIM begins when the shear stress acting on the habit plane resolved in the direction of transformation reaches a certain critical value. To gain further insight into this behavior, resolved shear stress factors (RSSFs) and theoretical total (CVP formation plus detwinning) transformation strains calculated in the framework of energy minimization theory Dadda *et al.* (2008); Sehitoglu *et al.* (2001a) have been displayed as a function of crystallographic orientation in a unit stereographic triangle shown in Figures 3.16(a) and 3.16(b), respectively, for $Co_{49}Ni_{21}Ga_{30}$ alloys. The negative values represent the compression stress state.

The RSSF value is an indicator of the critical stresses needed for SIM, the level of transformation strains and the recoverability upon loading along different orientations. The high RSSF value implies that the critical transformation stresses would be low, *i.e.* low CC-slopes, the transformation strains would be larger and the recoverability would be high. Table 3.2 lists the RSSFs for various single crystal of both $Co_{38}Ni_{33}Al_{29}$ and $Co_{49}Ni_{21}Ga_{30}$ alloys along with their Schmid's factor for slip in the austenite, theoretical transformation strains that include both CVP formation (ϵ_{CVP}) and detwinning (ϵ_{det}) strains, experimentally obtained maximum transformation strains, CC-slopes and PE temperature window. It is clear from the table that the aforementioned RSS criterion is valid in both alloy systems as the [001] orientation with largest RSSF value (0.56) exhibits the lower CC-slopes, larger transformation strains with complete recoverability than that observed in the other orientations with lower RSSF values of 0.35 and 0.33 for [123] and [235] orientations, respectively.

Moreover, based on the results shown Table 3.2, a criterion has been established to develop HTPMs that can demonstrate pseudoelasticity at high temperatures. The crystals with high RSSF, i.e. favorable orientation for the marten-

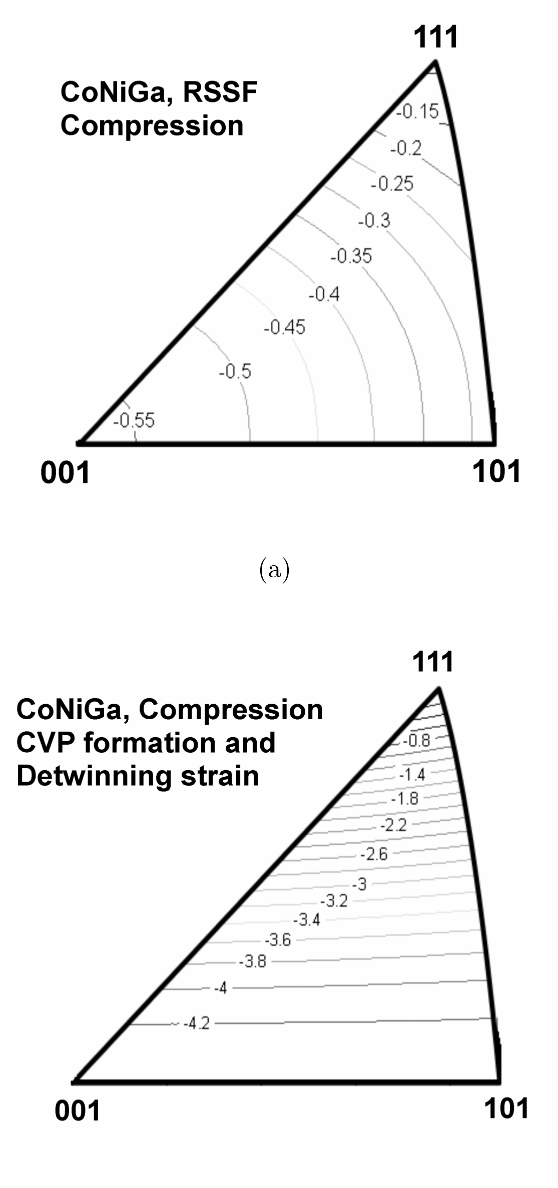

(a)

(b)

Figure 3.16: $Co_{49}Ni_{21}Ga_{30}$ (a) RSSF and (b) CVP formation (ϵ_{CVP}) and detwinning (ϵ_{det}) strains as a function of crystallographic orientation. Dadda *et al.* (2008).

sitic transformation with respect to the applied stress, and low values of Schmid factors, i.e. unfavorable orientation for the slip system in the austenite, demonstrate a large pseudoelastic temperature window. For example, the [001]-oriented $Co_{49}Ni_{21}Ga_{30}$ crystal with largest RSSF and zero Schmid factor demonstrates remarkably high-temperature pseudoelasticity at temperatures as high as 325 °C (Fig. 3.13) with large PE window of 300 °C (Table 3.2). This extends the utility of these alloys over a wider temperature range in comparison to NiMnGa Chernenko *et al.* (2003), CuAlNi Otsuka & Wayman (1999), CoNiAl Karaca *et al.* (2003), and NiTi Sehitoglu *et al.* (2000) alloys, which exhibit pseudoelastic temperature ranges of about 80, 125, 160 and 200 °C, respectively. This makes as-grown $Co_{49}Ni_{21}Ga_{30}$ an alternative to Cu-based, NiTi-based and NiMnGa HTSMAs. However, a detailed study on the stability of SIM transformation behavior at high temperatures is required for their successful utility as presented in the next chapters. Moreover, the upperbound for PE temperature range in the $Co_{38}Ni_{33}Al_{29}$ system is still open (>250 °C) and one would expect large temperature range due its low CC-slope of 1 MPa/°C (Table 3.2). Thus, future research should be focused on the development of high temperature Co-Ni-Al systems.

3.3 Chapter Summary

The basic shape memory characteristics of $Co_{38}Ni_{33}Al_{29}$ and $Co_{49}Ni_{21}Ga_{30}$ single crystals were analyzed and presented utilizing isostress thermal cycles and isothermal loading-unloading cycles at different temperatures in this chapter. The key findings of this study are given as follows:

1. The [001]-oriented $Co_{38}Ni_{33}Al_{29}$ single crystals subjected to high cooling rates following a high temperature heat treatment exhibit large phase transformation strains of about 4.1 % under compressive stress levels as low as 50 MPa. The maximum transformation strain observed is in agreement with the theoretical corresponding variant pair (CVP) transformation strain.

2. Similar to the [001] orientation, the [110]-oriented single crystals with high cooling rates exhibit large transformation strains of 4 % under compressive stresses as low as 50 MPa. Nevertheless, this strain value exceeds the theoretical CVP transformation strain, indicating a significant contribution of detwinning strains to the overall phase transformation strain.

Therefore, the results emphasize the need for texturing polycrystalline aggregates of the current material near the <001> and <110> poles with an optimum γ-phase volume fraction to achieve high transformation strains in $Co_{38}Ni_{33}Al_{29}$.

3. Near-perfect pseudoelasticity above the A_f temperature was obtained in compression tests with a maximum pseudoelastic strain of about 4.3 %. The $Co_{38}Ni_{33}Al_{29}$ samples investigated in this work demonstrate a large pseudoelastic window (> 250 °C). Thus, $Co_{38}Ni_{33}Al_{29}$ alloys with optimum ductile γ-phase content are suitable for conventional pseudoelastic applications at elevated temperatures.

4. The $Co_{38}Ni_{33}Al_{29}$ single crystals studied demonstrate good cyclic stability and trainability with a maximum two-way shape memory effect (TWSME) strain of 2.7%. The TWSME strain obtained for the [001]-oriented air cooled samples constitutes an evidence of the substantial role of the ductile γ-phase for trainability in the absence of pronounced dislocation activity.

5. Owing to the most favorable orientation for the transformation and least favorable for dislocation slip, the [001]-oriented $Co_{49}Ni_{21}Ga_{30}$ single crystals exhibit about 4.4% transformation strains at compressive stress levels as low as 4 MPa, and a fully recoverable 4.3 % pseudoelastic strain. Perfect pseudoelasticity was observed in the temperature range from room-temperature to 325 °C indicating their excellent high temperature capability.

6. The pseudoelastic temperature range is limited by the occurrence of slip, which sets in the range of 650-750 MPa at least for [123] and [235]-oriented $Co_{49}Ni_{21}Ga_{30}$ samples. Further thermomechanical treatments are expected to increase the matrix strength that will raise the flow resistance of austenite so that the alloys can undergo stress-induced martensitic transformation even at higher temperatures. The results open the possibility to tailor textured polycrystalline material with a strong <100> component along the loading axis for its outstanding high-temperature pseudoelasticity.

Table 3.2: Maximum resolved shear stress factors (RSSFs), Schmids factors (SF) for the slip system {110} <001> in the austenite, theoretical transformation strains ($\epsilon_{CVP} + \epsilon_{det}$), maximum experimentally obtained pseudoelastic strains, Clausius-Clapeyron slopes and pseudoelastic temperature window for $Co_{49}Ni_{21}Ga_{30}$ (CNG) and $Co_{38}Ni_{33}Al_{29}$ (CNA) single crystals under compressive loading conditions.

	Theoretical Estimations			Experimental Values		
Specimen	RSSF	SF	$\epsilon_{CVP} + \epsilon_{det}$ (%)	Max_Exp ϵ_T (%)	CC-slope (MPa/°C)	PE-Window (°C)
CNG_[001]	0.56	0.0	4.4	4.3	2.3	> 300
CNG_[123]	0.35	0.4	3.6	3.4	2.6	220
CNG_[235]	0.33	0.42	3.0	3.0	3.9	200
CNA_[001]-WQ	0.54	0.0	4.4	4.3	1.0	> 200
CNA_[123]-AC	0.35	0.4	3.3	3.6	2.25	> 250

Chapter 4

$Co_{49}Ni_{21}Ga_{30}$-alloys as a High-temperature Pseudoelastic Material

4.1 Introduction

This chapter deals with the analysis of high-temperature *in-situ* microstructural observations in correlation with the stress-strain response during SIM transformations in $Co_{49}Ni_{21}Ga_{30}$ alloys. Especially, as-grown $Co_{49}Ni_{21}Ga_{30}$ [001]-oriented crystals under compressive loading conditions were used as they exhibit a large PE window as shown in Figs. 3.13 and 3.15 on pages 43 and 45 in the last chapter. The effect of training on the PE behavior and its temperature range has also been established and it is found that trained crystals exhibit PE response at temperatures as high as 425 °C. Moreover, the PE behavior in terms of stress hysteresis and critical transformation stress levels and their variation with test temperatures are analyzed and discussed in this chapter. *In-situ* OM and DIC were carried out at various stages during the PE experiments to follow the evolution of the stress-induced phase transformation at elevated temperatures and to track the propagation of phase boundaries. This information is essential for the modeling of inhomogeneous deformation regimes in SMAs Abeyaratne & Knowles (1993). *In-situ* microscopy revealed the martensite stabilization due to pinning of moving interfaces in $Co_{49}Ni_{21}Ga_{30}$ alloys especially at elevated temperatures (>120 °C), which is macroscopically reflected by the shift of the unloading curve to lower stress levels. Along with microscopy observations, the spatial visualization of strain localization obtained by using DIC revealed heterogeneous transformation characteristics at temperatures below 120 °C, above which the nucleation and growth characteristics of SIM transformation are quasi-homogeneous resulting in a multi-variant configuration, which was later inherited by the trained crystal. An insight into the evolution of microstructure and stress-strain behavior in terms of stress hysteresis with test temperatures is provided, and the possible operant mechanisms are presented.

4.2 Microstructure-pseudoelastic property relationships

4.2.1 Mechanical property variation with temperature

Figure 4.1 demonstrates the variation in the PE parameters such as stress hysteresis, $\Delta\sigma$, and the critical transformation stress levels for both forward, (σ_{crit}^{For}), and reverse, (σ_{crit}^{Rev}), transformations obtained from the curves shown in Fig. 3.13 on page 43 in Chapter 3. The definitions for the aforementioned parameters are given in Fig. 3.10 on page 39. Fig. 4.1 demonstrates that σ_{cr}^{For} follows a linear relationship with a CC-slope of of 2.2 MPa/°C, and also shows a significant variation of stress hysteresis with test temperature, accordingly the plot is divided into two regions. An almost constant stress hysteresis of about 20 MPa is observed in Region I, i.e., until the test temperature reaches about 120 °C. An increase in temperature above 120 °C brings about a continuous rise in stress hysteresis reaching the highest level of 350 MPa at 320 °C (Regions II), which is an 18 fold increase from the value obtained in region I. The deviation of the σ_{cr}^{Rev} values from linearity in the temperature regions II in the figure explains the increase in the stress hysteresis. This trend in σ_{cr}^{Rev} suggests the difficulty in nucleation of habit planes necessary for the onset of the reverse transformation Chernenko *et al.* (2004). This is known as mechanical stabilization of martensite Liu & Favier (2000); Picornell *et al.* (2001) due to inelastic deformations such as martensite

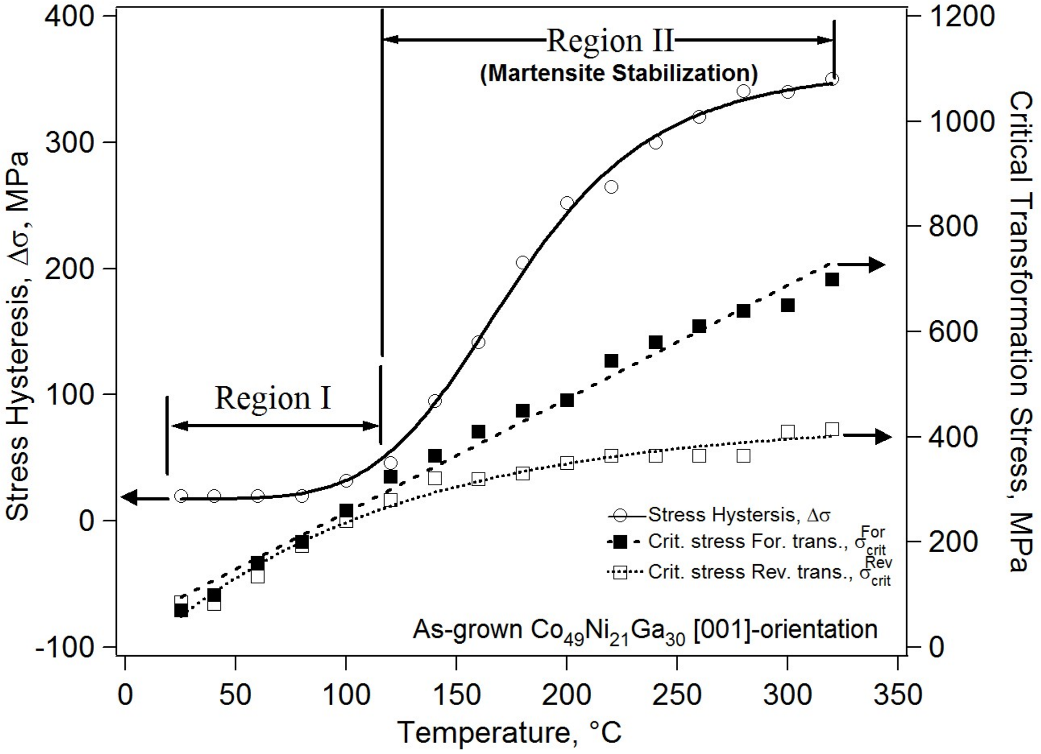

Figure 4.1: The evolution of stress hysteresis and critical transformation stress levels with test temperatures in as-grown $Co_{49}Ni_{21}Ga_{30}$ [001]-oriented crystal.

reorientation (MR) and/or detwinning that prevail(s) during the forward transformation. The degree of difficulty depends on the amount of detwinning as it removes the back stress that was stored in the twinned martensite, which would have aided the back transformation upon unloading Dadda *et al.* (2006b, 2008); Gall *et al.* (1999). Moreover, the transformation strain, ϵ_T (*cf.* Fig. 3.10 for definition), decreases gradually with temperature beginning at 4.3 % strain and saturates at around 3 % strain above 100 °C. The observed variation in, $\Delta\sigma$ and ϵ_T can be understood as a change in the martensite morphology during SIM transformation and its dependency on the temperature is clarified with the help of *in-situ* observations in the following section.

4.2.2 Evolution of microstructure with temperature during SIM transformations

4.2.2.1 Region I - Constant low stress hysteresis

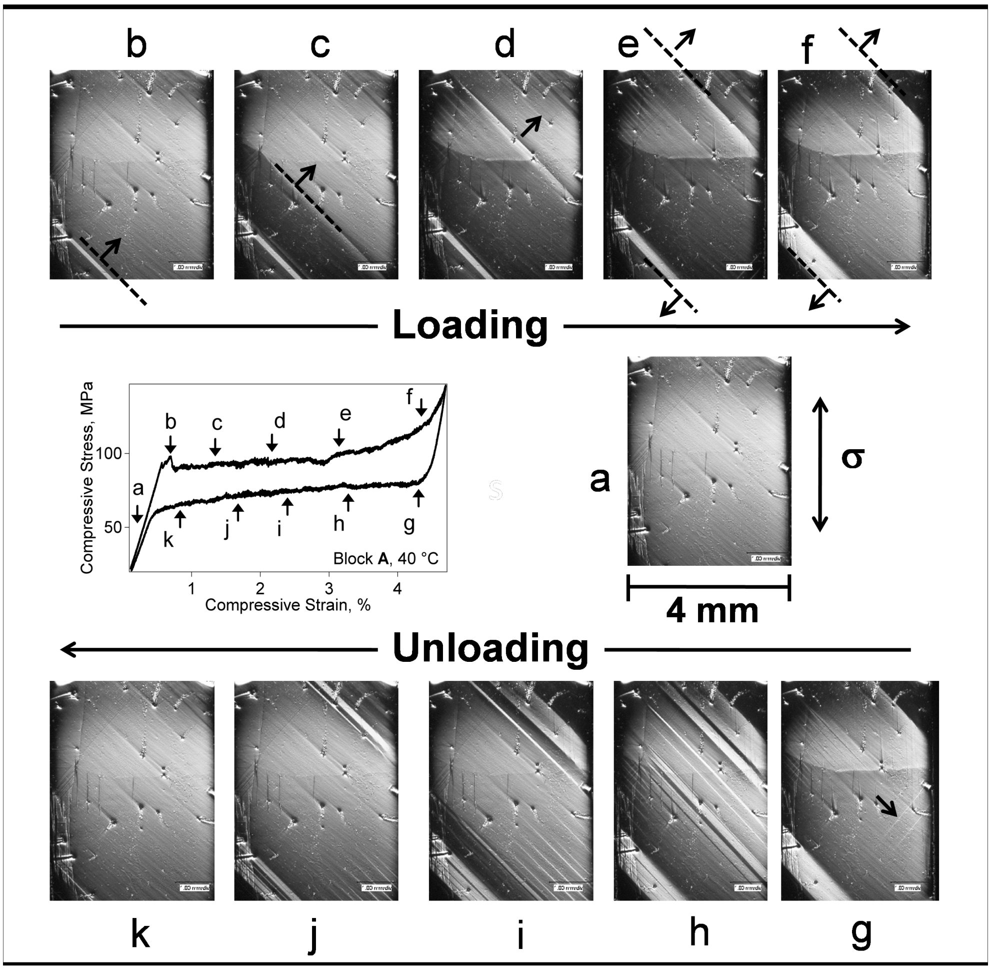

Figure 4.2: Microstructural changes during pseudoelasticity of as-grown $Co_{49}Ni_{21}Ga_{30}$ [001]-oriented single crystal at 40 °C. The direction of loading is represented by σ. The arrow in the micrograph **g** points out the formation of new phase fronts, whose normals are perpendicular to the original ones.

Systematic *in-situ* high-spatial resolution optical microscopy has been conducted at critical temperatures in the different regions as defined in Fig. 4.1.

Figure 4.2 shows the micrographs that were recorded at different stages on the PE curve during loading and unloading paths obtained at 40 °C. Figure 4.2a shows the reference microstructure of the specimen taken at point **a** on the curve in the inset. It is clear from Figure 4.2b that the departure of the PE curve from its initial linearity is characterized by the formation of a single interface or martensite plate with well defined habit planes indicating the onset of SIM. Straining of the sample to points **c** and **d** on the curve results in concurrent growth of the martensite region via propagation of the phase-front as marked by arrows in Figs. 4.2c and d. At point **e** on the curve a new phase front propagates in the opposite direction as indicated by arrow in Fig. 4.2e further increasing the volume fraction of martensite. This event, in fact, is reflected in the macroscopic response as a raise in stress level to 95 MPa on the stress-strain curve at point **e**, which is equal to the stress value at point **b**. A further loading to point **f** (4.3 %) has resulted in an apparent strain hardening and the corresponding image shows that the sample almost fully transformed. The resultant total strain of 4.3 % from the formation of a nearly single crystalline martensite from a single crystalline austenite is in good agreement with the expected theoretical value shown in Fig. 3.16(b).

As the martensite becomes unstable upon unloading, the reversion to austenite takes place by forming numerous additional interfaces, whose habit planes are perpendicular to the original ones as marked by an arrow in Fig. 4.2g. These new phase fronts are consumed by the original dominant ones as seen in in Fig. 4.2h probably by a reorientation mechanism. Unlike the formation and propagation of a single interface during the forward transformation, reverse transformation is characterized by the nucleation of multiple emanating phase fronts. The SIM transformation is always accompanied by the formation of mis-match dislocations due to the difference in the crystal structures of austenite (parent) and martensite Otsuka & Wayman (1999), and these will be left behind as the moving interface sweeps through fresh austenite areas. Upon unloading, these dislocated regions will act like nucleation sites forming new interfaces for the growth of austenite. As seen in Fig. 4.2i, further unloading lead to the coalescence of austenite variants and thickening of austenite regions reducing the total number of visible interfaces. The reverse transformation further proceeds upon unloading to 1.8 % and 0.8 %, points **j** (Figs. 4.2j) and **k** (Figs. 4.2k) on the PE curves, respectively. Finally, the sample reverts back to austenite phase recovering its initial microstructure and orientation at minimum applied stress levels.

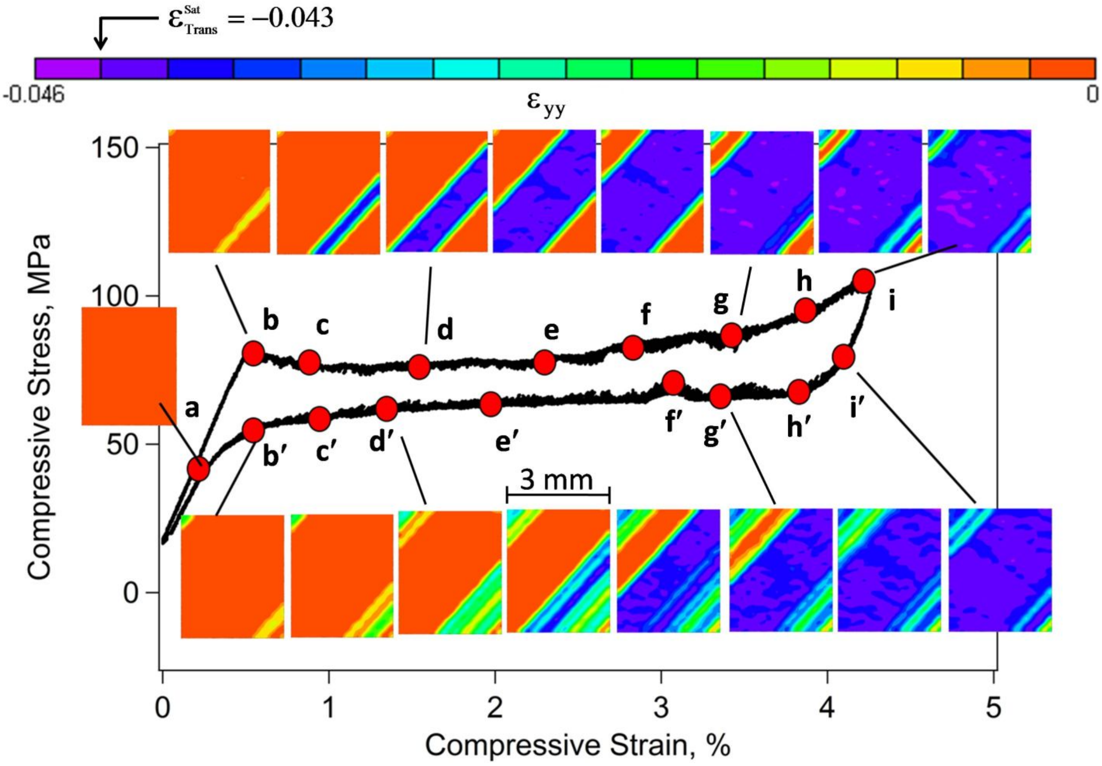

Figure 4.3: Local strain distribution during stress-induced martensite transformation in $Co_{49}Ni_{21}Ga_{30}$ [001]-oriented single crystal at 40 °C. The elastic strain, ϵ_0, of -0.5 % (defined in Fig. 3.10 on page 39) was subtracted as the focus was only on the transformation strains. See main text for detail.

Figure 4.3 presents the PE response of a companion as-grown $Co_{49}Ni_{21}Ga_{30}$ [001]-oriented sample at 40 °C and the evolution of the localized component of the strain in the loading direction (ϵ_{yy}) and its distribution at the mesoscopic scale obtained by DIC at different stages of loading and unloading. The inflection point where the curve deviates from linearity is characterized by the appearance of a band with a localized transformation strain of about -1.4 % within the band and its morphology is similar to that captured by the optical microscope seen in

Fig. 4.2b. If only optical imaging is available, this would be typically interpreted as a completely transformed martensite plate with well defined habit planes. By contrast, DIC revealed that the strain inside the band does not show the saturation value of the transformation strain (ϵ_{Trans}^{Sat}), which is -4.3 % in the current alloy Dadda *et al.* (2008) under compressive loading conditions as marked on the scale bar in the figure. This demonstrates that the transformation is only partially complete when the bands form and proceeds with further loading as one can see from Figure 4.3c. In addition, similar reports on NiTi sheets elsewhere Daly *et al.* (2007) using DIC seem to indicate that this is true for the other existing SMAs as well.

Further straining leads to growth of the martensite as can be seen in Figs. 4.3d and e. Fig. 4.3f demonstrates that new bands appear (green bands on top-left corner) when the moving phase front stops, concomitant with the raise in local stress at point **f**, which is similar to the observation made at point **e** in Fig. 4.2e. This suggests that the nucleation of bands always starts at a little higher stresses than that required for their propagation. This can also be inferred from the stress drops at points **b** marked on either curves shown in Figs. 4.2 and 4.3. In addition, frequent occurrence of such events has led to the periodic stress drops and raises along the loading path, for example points **f** and **g** in Fig. 4.3. The serrated features of the stress-strain response are attributed to the stick-slip motion of the phase boundaries Vainchtein (2002) and can only appear when the experiments are performed at sufficiently slow loading rates as experimentally observed and simulated elsewhere Dadda *et al.* (2008); Vainchtein (2002).

Loading of the sample to point **h** on the curve has resulted in the increase in martensite volume fraction and also the onset of an apparent strain hardening. The latter can be attributed to the elastic deformation of martensite as one can see purple islands in completely transformed blue region (Figs. 4.3h and i). However, both DIC (Fig. 4.3) and microscopy (Fig. 4.2) observations unequivocally verified that the end of the loading plateau does not imply the completeness of the transformation in SMAs. This can be seen as green and yellow bands (partially transformed regions) in Fig. 4.3i. Upon unloading, the reverse transformation begins with the formation of multiple variants within the fully transformed martensitic regions as seen before in Fig. 4.2, thus, deserves the same explanation. The transforming localized bands and their growth characteristics during SIM suggest that the transformation is heterogeneous on the macroscopic scale in $Co_{49}Ni_{21}Ga_{30}$ alloys at low temperatures. Moreover, the spatial variation of strains within the individual bands points out the transformation heterogeneity in the specimen at the microscopic level as well (Fig. 4.3).

4.2.2.2 Region II - Increasing stress hysteresis

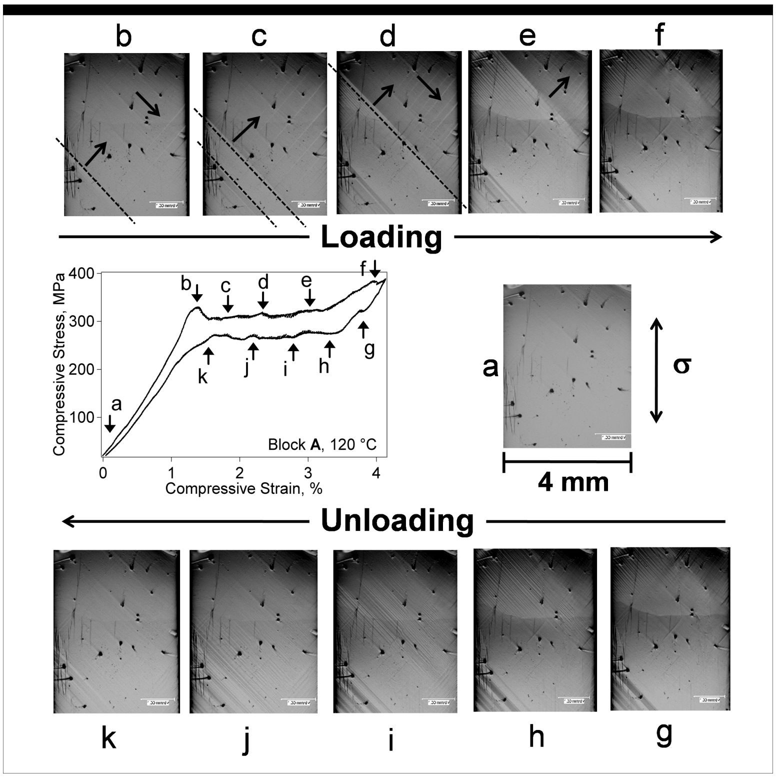

Figure 4.4: Pseudoelastic response and variation in the microstructure during forward and reverse transformation in $Co_{49}Ni_{21}Ga_{30}$ [001]-oriented crystal at 120 °C. Differently oriented arrows indicate the coexistence of two different types of habit-plane variants. The interfaces marked by the downward pointing arrows in Figs. 4.4b and d were consumed during the growth of the other dominant martensite plate.

In order to gain insight into the change in stress hysteresis at 120 °C (end of region I, Fig. 4.1), *in-situ* observations were made and representative micrographs are shown in Figure 4.4 along with the PE response at 120 °C. The forward transformation is initially characterized by the formation of many variants (phase boundaries) with the progression of loading as indicated by arrows, but further growth of martensite is achieved by the propagation of a single interface (pointed out by the arrow in Fig. 4.4c) consuming the others as indicated in Figs. 4.4b-e. In addition, each wave pattern in the stress-strain curve corresponds to the appearance and coalescence of new interfaces with the moving phase front. Further loading results in the growth of martensite by transforming remaining pockets of austenite regions (Fig. 4.4f) and also in a considerable strain hardening. The reverse transformation is accompanied by the activation of numerous interfaces as it was discussed earlier for Figs. 4.2 and 4.3 and finally the sample retained its original structure at the minimum stress level (Figs. 4.4g-k). The increase in stress hysteresis at 120 °C (Fig. 4.1) can be associated with the energy dissipated in the form of frictional work that is spent overcoming the resistance to the motion of the dominant interface. One would expect a high resistance to the propagating inter-phase boundary in this case because of the increased amount of interacting events with the other interfaces as seen in Fig. 4.4.

Unlike in Fig. 4.4, the images in Figure 4.5 show that the nucleation and growth of SIM in the sample at 200 °C is characterized by the simultaneous formation and growth of multiple variants, which is an indicative of a quasi-homogeneous transformation behavior in SMAs Abeyaratne & Knowles (1993); Shaw & Kyriakides (1995). Because of the significant increase in test temperature (200 °C) and raise in interacting events emanating from simultaneously propagating variants (Figs. 4.5b-d), continuation of the transformation requires an increase in the applied stress. This brings about an ascending as well as a wavy nature of stress-strain curve as seen from the figure. Further loading resulted in a change in the material contrast due to significant change in the topography (Figs. 4.5e-f), which indicates the progression of transformation and growth of martensite regions. Upon unloading, the images in Figs. 4.5h-i demonstrate hardly any changes in the martensite morphology until point **j** is reached on the curve suggesting difficulty for the reverse transformation. The latter also

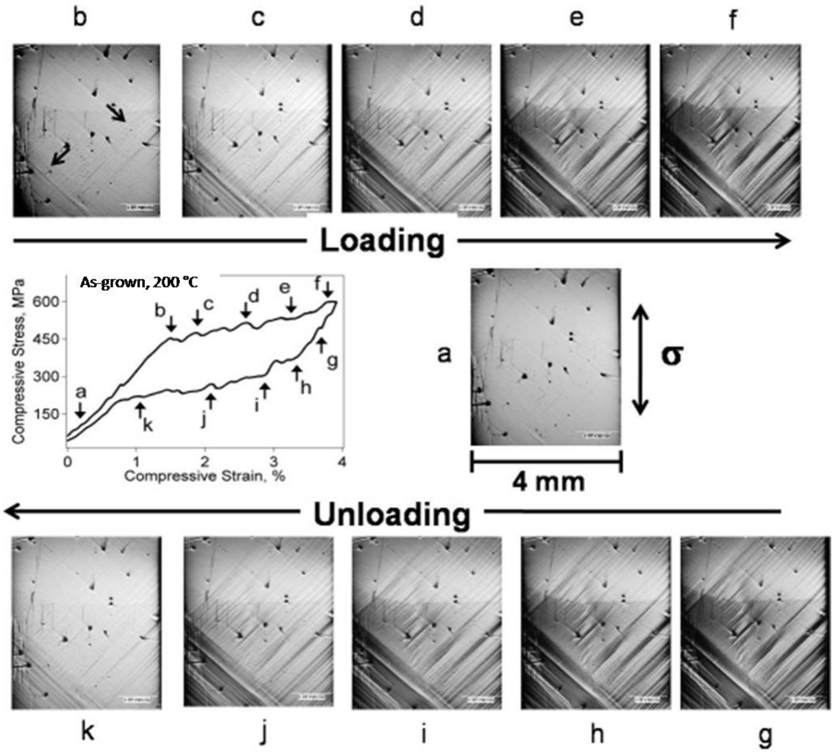

Figure 4.5: Evolution of microstructure with the forward and backward stress-induced phase transformations in $Co_{49}Ni_{21}Ga_{30}$ [001]-oriented single crystal at 200 °C.

implies the occurrence of detwinning of twinned martensite variants, thus, a large stress hysteresis is recorded for this test temperature. Since the transformation is nearly homogeneous, it is hard to notice any events at the microscopic level that are taking place at the intermediate strain levels between the marked points on the curve. Further unloading led to the material to retrieve its original microstructure in the austenite state (Fig. 4.5j-k).

4.3 Effect of Training on the Pseudoelasticity

As the SME and PE phenomena are often repeated in several applications that utilize SMA devices, it is necessary to understand the trainability, reproducibility and stability of these properties, and which can be done by adopting several training methods. Most training procedures are based on the repetition of transformation cycles from the parent to preferentially oriented martensite. Some of the examples are: repetition of one-way memory effect, temperature cycles at a constant strain or stress, and pseudoelastic cycling. This is generally observed that the training will result in complete recoverability and/or improved shape memory properties and/or TWSME. This is achieved by the formation of complex dislocation arrays which have the lowest energy in the repeatedly induced 'trained' martensite variants. In addition, the increased dislocation density will suppress further slip deformation by raising the strength of the matrix. This in turn generates martensite at lower stress levels due to the favorable stress fields around these defects leading to TWSME phenomenon or complete recoverability.

The schematic in Figure 4.6 shows the two sequences of experiments namely Block **1** and **2** that were carried out on two different companion $Co_{49}Ni_{21}Ga_{30}$ specimens. The isostress thermal cycles and a single loading-unloading cycle at each temperature step at Level **1** are referred as Type I and II training procedures, respectively. In the figure, Type II training experiments at Level **2** will provide an insight into the pre-transformation history effects in terms of reproducibility, recoverability and stability of pseudoelastic behavior in $Co_{49}Ni_{21}Ga_{30}$ alloys. Moreover, the instances of Type I and II training experiments can be seen in Figs. 3.8 and 3.13 on page 37 and 43 in Chapter 3, respectively.

Figure 4.7 shows a strong temperature dependence of stress-strain response of a Type I trained $Co_{49}Ni_{21}Ga_{30}$ [001]-oriented crystal. The stress-strain loading path after the initial linear elastic deformation exhibits a typical plateau type response at low temperatures, (< 120 °C), while higher temperatures bring about an ascending stress-strain curve with a pronounced strain hardening. This behavior is similar to that observed in as-grown crystals in Figs. 3.13, 4.2 and 4.5, thus, a multi-variant martensite morphology is schematically depicted in Fig. 4.7 at elevated temperatures (200 °C). The multi-variant morphology offers higher resistance to the propagating interface because of increased variant-variant interactions (Fig. 4.5) during the progression of SIM transformation giving rise to an ascending type stress-strain response. Similarly, based on the *in-situ* observations made on an as-grown alloy (see Figs. 4.2 and 4.3), a schematic illustrating

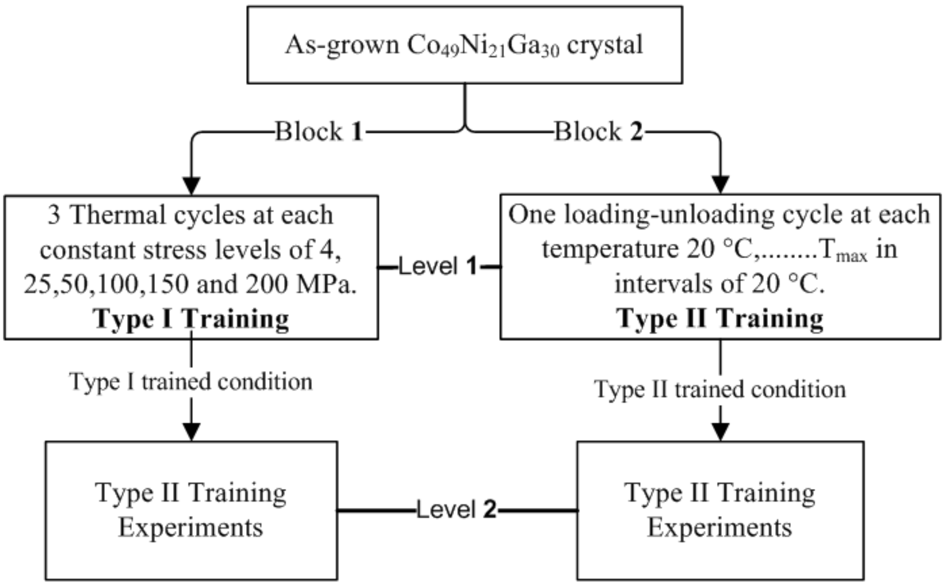

Figure 4.6: Schematic illustration of Type I and II training procedures that were adopted for this study. The first appearance of residual strains in a PE curve determined the maximum test temperature $T_{\max}$.

fewer preferred variants is indicated in Fig. 4.7 for low temperature regimes as large transformation strains and a plateau type loading characteristics are more pronounced.

Figure 4.8 shows the pseudoelastic response of a Type II trained $Co_{49}Ni_{21}Ga_{30}$ [001]-oriented crystal as well as that of an as-grown crystal for comparison. It is clear from the figure that training had a significant influence on the mechanical behavior especially the reduced transformation strains at low test temperatures. This is explained by recording the microstructures at various stages of loading-unloading path of the curve at 40 °C obtained for Type II trained crystal as shown in Figure 4.9.

The curve in Fig. 4.9 shows that loading of the specimen resulted in a near plateau region of A-C and is followed by a pronounced strain hardening in the C-D portion. The microstructure evolution in A-D region is similar to the one that was observed during training at high temperatures (200 °C, Fig. 4.5). Except that deformation to points **C** and **D** led to the transformation of the encircled

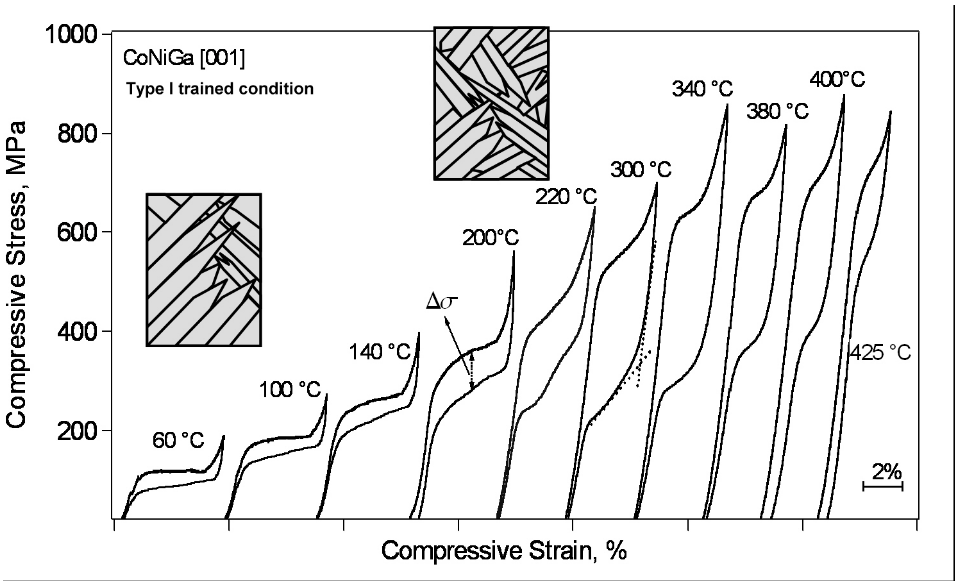

Figure 4.7: Pseudoelastic response of Type I trained $Co_{49}Ni_{21}Ga_{30}$ single crystal as a function of temperature. The schematics illustrate the expected martensitic morphology and potential internal twinning of variants is not shown Dadda *et al.* (2006b).

area of the sample, which was not observed in earlier results shown in Figs. 4.2 and 4.5. Further loading beyond point **D** changes the progression (slope) of the stress-strain curve resulting in a second plateau (D-E). This is pertaining to inelastic deformations such as MR and/or detwinning of martensite, which hinder the reverse transformation resulting in residual strains as seen in the figure. This is deformation induced martensite stabilization and can be realized from the microstructures recorded during unloading that hardly evolve in the specimen from point **E** to **G**. When the stress reaches its minimum value, the sample recovers only 1 % strain and the rest was recovered completely after heating the sample to 100 °C demonstrating the typical SME phenomenon. The latter is expected when the stabilized martensite undergoes MR or detwinning processes. The *in-situ* microscopy results at high temperatures on Type II trained crystals are not reported here as the microstructure is stabilized and no significant changes in martensite morphology were noticed. The differences in the PE behavior of

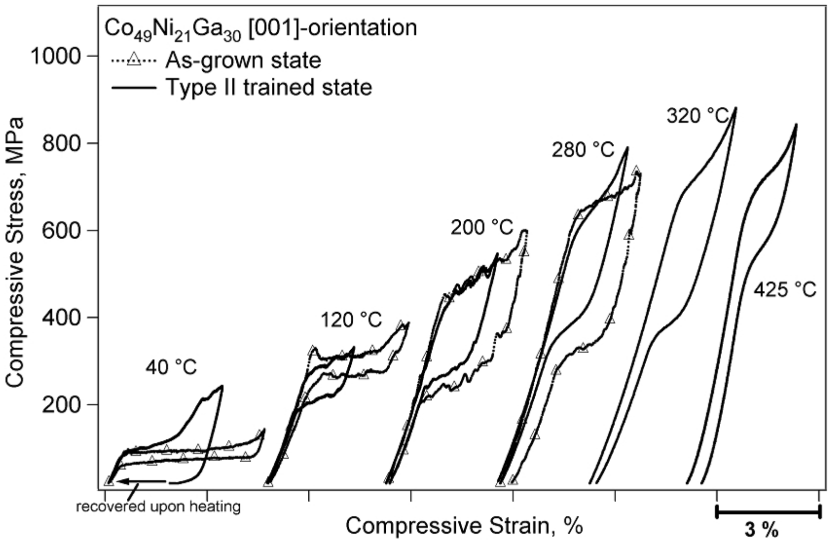

Figure 4.8: Pseudoelastic response of Type II trained $Co_{49}Ni_{21}Ga_{30}$ [001]-oriented single crystal as a function of temperature in comparison with those obtained from as-grown crystal.

Type I and II trained crystals (Fig. 4.7 and 4.8, respectively) can obviously be linked to the type of training and a possible small variation in the chemical composition of the samples that were used. The presence of low stress levels of only 200 MPa (Fig. 3.8) and higher stresses levels above 600 MPa (Fig. 3.13) in Type I and II training, will evolve dislocation structure and their distribution in the material differently as shown in TEM images in Figures 4.10 and 4.11, respectively. The relatively high density of dislocated regions in Type II trained crystal (Fig. 4.11) offer more number of nucleation sites for the onset of numerous variants resulting in a multi-variant morphology and whose simultaneous growth will lead to homogeneous type transformation as seen in Fig. 4.9. This also altered the transformation strains in Type II trained crystal in the whole range of operating temperatures.

Figure 4.12 shows the evolution of stress hysteresis with temperature and its dependency on the type of training. Interestingly, the same trend prevails in the stress hysteresis regardless of the condition of the sample. However, in the case of

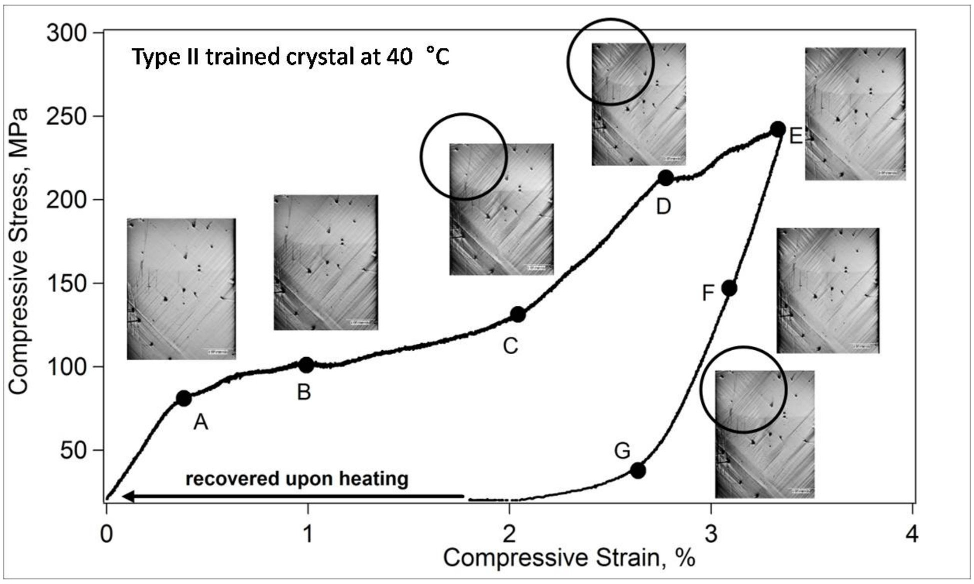

Figure 4.9: Microstructural evolution during stress-induced phase transformation in the Type II trained $Co_{49}Ni_{21}Ga_{30}$ [001]-oriented crystal at 40 °C.

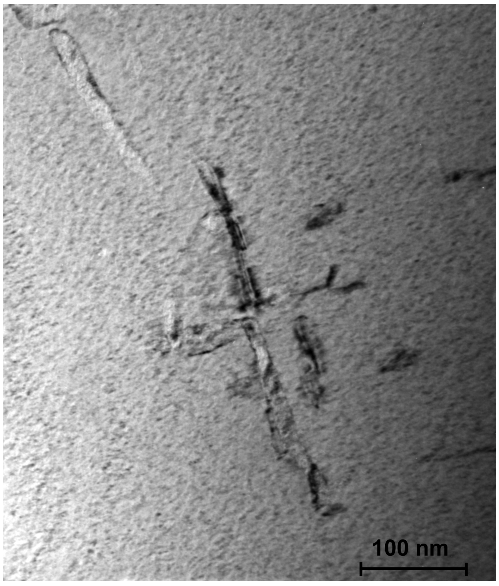

Figure 4.10: Bright field image showing the microstructure of Type I trained $Co_{49}Ni_{21}Ga_{30}$ [001]-oriented single crystals.

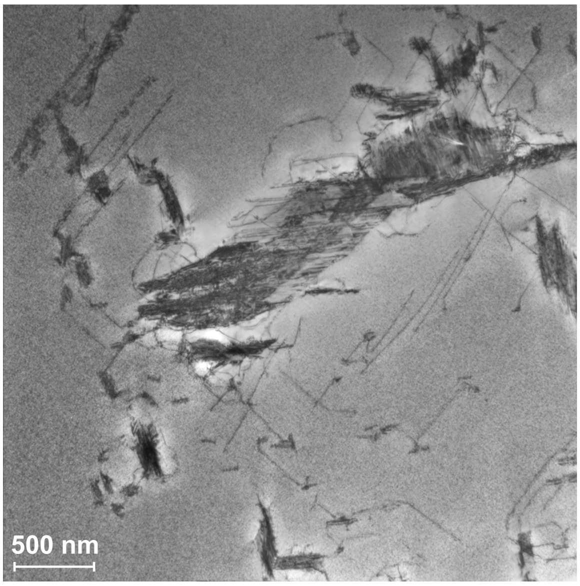

Figure 4.11: TEM image showing the dislocations in Type II trained $Co_{49}Ni_{21}Ga_{30}$ [001]-oriented single crystals.

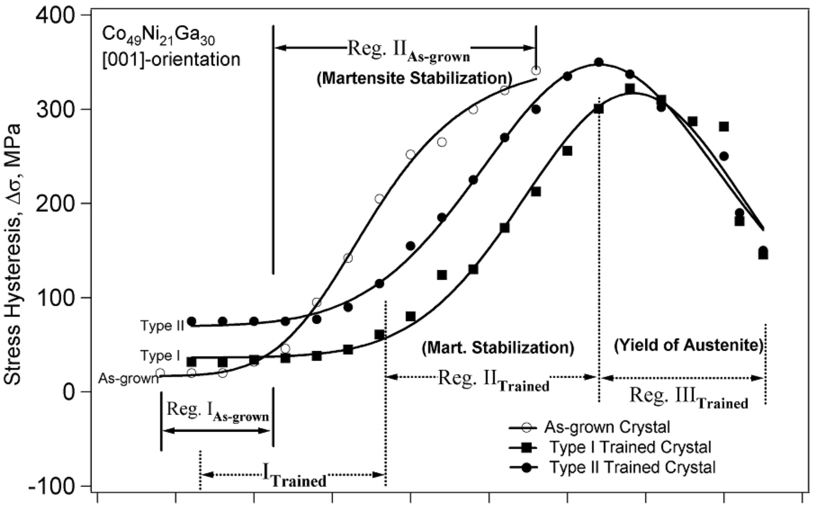

Figure 4.12: Effect of the training on the evolution of stress hysteresis with test temperature in as-grown $Co_{49}Ni_{21}Ga_{30}$ [001]-oriented single crystals.

trained crystals; the region II$_{Trained}$ starts at slightly higher temperatures of about 180 °C and a new region III$_{Trained}$ is defined as the stress hysteresis decreases. The former suggests that the detwinning seems to be delayed in trained samples, which is in good agreement with earlier TEM studies Dadda *et al.* (2008) where the detwinning was partially suppressed in a pre-fatigued $Co_{49}Ni_{21}Ga_{30}$ [123]-oriented crystal due to the increased amount of dislocations during the cycling.

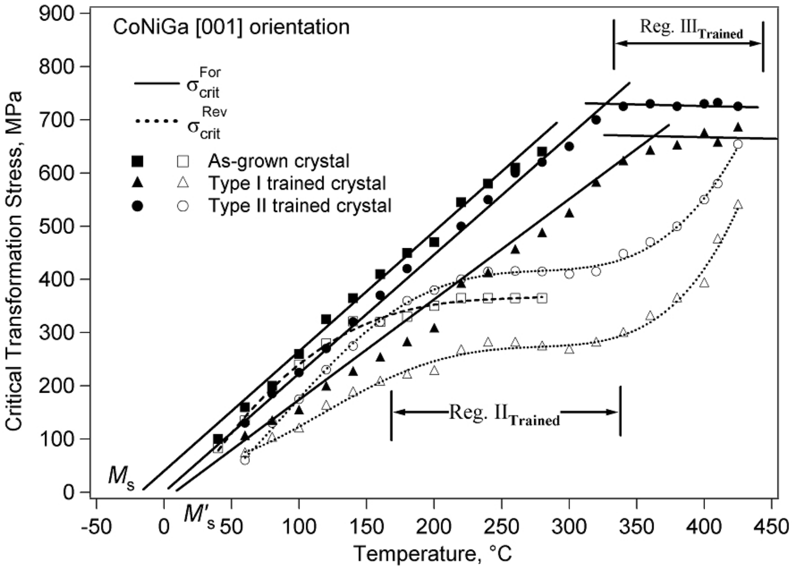

Figure 4.13: Evolution of critical stress levels for both forward (solid lines, full symbols) and reverse (dashed lines, open symbols) transformations with the training in [001]-oriented $Co_{49}Ni_{21}Ga_{30}$ single crystals.

Moreover, the decreasing trend of stress hysteresis values observed for region III$_{Trained}$ in Fig. 4.12 can be related to the decreasing and increasing values of σ_{cr}^{For} and σ_{cr}^{Rev}, respectively above 325 °C as shown in Fig. 4.13. The deviation of σ_{cr}^{For} from its linear CC-curve, can be attributed to plastic yielding of the austenite, which now occurs prior to the SIM Dadda *et al.* (2006b); Sehitoglu *et al.* (2000). This fits to the occurrence of similar deviations observed for [123] and [235]-oriented crystals in the range of 650-800 MPa in Fig. 3.15 on Page 45 clearly supporting the onset of yield in $Co_{49}Ni_{21}Ga_{30}$ alloys via slip deformation.

The increase in σ_{cr}^{Rev} (Fig. 4.13) is linked to the incomplete phase transformation, thereby, untransformed regions of austenite help the onset of the reverse transformation.

The increase in stress hysteresis in region II is connected to the dominant detwinning and associated martensite stabilization, which is in fact seen as the shift of the unloading curve to lower stress levels, *i.e.* the decrease in σ_{cr}^{Rev} in Fig. 4.13. The occurrence of this mechanism at elevated temperatures can be linked to the easier mobility of martensite twin boundaries due to high thermal activation in $Co_{49}Ni_{21}Ga_{30}$ alloys.

In addition, martensite stabilization due to symmetry conforming-short range ordering (SC-SRO), especially in B2 ordered alloys that undergo thermoelastic martensite transformations should not be ruled out in the present case. Owing to the diffusionless nature of martensitic transformation, the resultant martensite inherits the high temperature B2 crystal symmetry, which is now thermodynamically unstable as this is different from the $L1_0$ symmetry of martensite in $Co_{49}Ni_{21}Ga_{30}$ alloys. The restoration of the $L1_0$ symmetry or ordering can be achieved via atomic rearrangement within the sublattice of the imperfectly ordered martensite, *i.e.* SC-SRO, which is similar to the atomic diffusion process in ordered usual intermetallics. This is the only way that a martensite can lower its free energy without altering the average martensite structure (equilibrium phase) Ren & Otsuka (1997). This inhibits the reverse transformation initially, *i.e.* stabilizes the martensite, resulting in an increase in the critical transformation temperature (A_s) for the martensite to austenite (Figure 4.14). Moreover, a raise in A_s temperatures is thermodynamically equivalent to a decrease in σ_{cr}^{Rev}. This behavior, in fact, can be observed from the PE curves at 120 °C shown in Fig. 4.8 before and after training.

Furthermore, the current TEM investigations also provide quintessential evidence of SC-SRO in $Co_{49}Ni_{21}Ga_{30}$ alloys. The martensite band-like contrast marked with a white arrow in Fig. 4.15 in the B2-matrix, whose selected area electron diffraction pattern confirms the B2 structure, indicates the existence of a ’faulted’ (ghost like martensite) SRO symmetry in the cubic phase and was termed as *microstructure memory* by Otsuka *et al.* Otsuka & Ren (2001). This

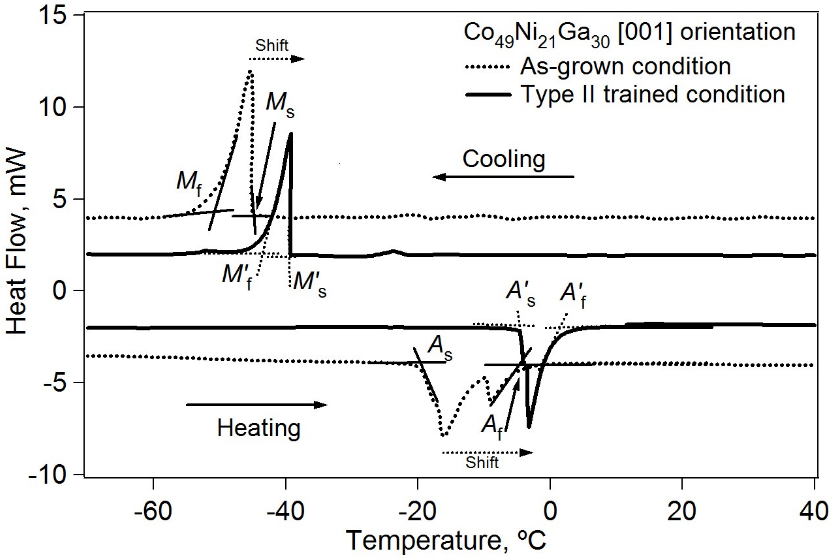

Figure 4.14: Thermograms of $Co_{49}Ni_{21}Ga_{30}$ alloy under as-grown (dashed) and Type II trained (solid) condition. The method of intersecting slope lines has been adopted to determine transformation temperatures. The dashed arrows represent the shift of transformation temperatures to higher temperatures as a result of training while the solid ones show the direction of cooling and heating paths.

phenomenon has been reported for off-stoichiometric Au-Cd alloys as a manifestation of SC-SRO Otsuka & Ren (2001).

Note that the SC-SRO is associated with the diffusion of atoms at the sublattice level that may involve mobile point defects such as vacancies, anti-site defects or both (triple defects, TDs). And the deviation from stoichiometry brings about a high density of point defects in any ordered system Ren & Otsuka (1997). One would expect the same in the present Co-21Ni-30Ga (at. %) system as it deviates from stoichiometry and also possesses ordered B2-austenite and $L1_0$-martensite structures. Although there is no direct experimental evidence of these point defects, the resultant stabilization effects can easily be realized from the macroscopic and microscopic observations made in the present study. For example, the shift of the unloading curve to lower stress levels (Fig. 4.13), which

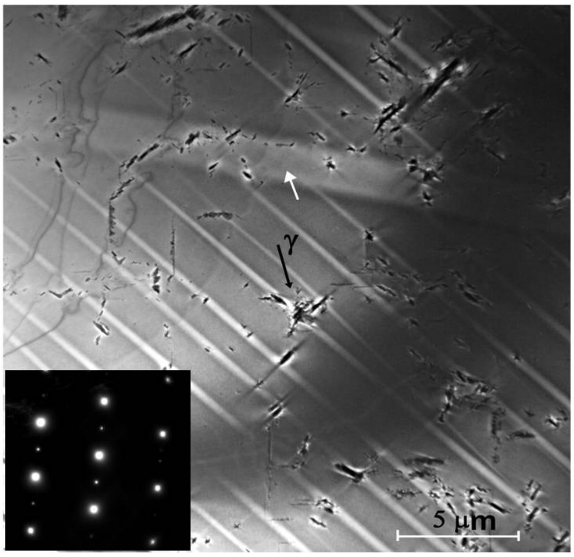

Figure 4.15: Bright field TEM image of a trained $Co_{49}Ni_{21}Ga_{30}$ [001]-oriented crystal showing the stabilized martensite needles pinned at the secondary phase γ particles as marked out by a black arrow. The white arrow indicates a ghost like martensitic structure. The inset displays the corresponding selected area diffraction pattern (SADP) confirming the B2 crystal structure of the matrix.

means martensite stabilization, is observed only at elevated temperatures (region II in Fig. 4.13). This implies that the mobilization of vacancies due to thermal activity is increased speeding up the diffusion process, thereby the stabilization phenomenon. This will also increases the number interaction events with linear (dislocations) and planar (interphase or intervariant boundaries) defects bringing about Cottrell-type pinning atmospheres around these defects, strongly affecting the mobility of propagating interfaces. This enhances further diffusion (on a rather large distance) of point defects migrating to interfaces because of energetically more favorable positions in the vicinity of interfaces Kustov *et al.* (2004b). This can lead to a drop in the local free energy of martensite interfaces stabilizing the martensite plates, which is called kinetic pinning-induced stabilization by Kustov *et al.* in their recent work Kustov *et al.* (2004a). Presence of such pinned interfaces require a higher chemical driving force for the reverse transformation to proceed, thus, decreased σ_{cr}^{Rev} values have been recorded in the current study.

Moreover, during the forward transformation, as soon as the pinning occurs and the local thermoelastic balance is shifted to higher stress levels due to the raise of the friction stress acting on the boundary, another martensite plate can be easily nucleated as is evident from microscopy (point **e**, Fig. 4.2) and DIC (points **f**-**g**, Fig. 4.3) results. This mechanism seems to be more pronounced at high temperatures due to the aforementioned diffusion mechanisms that involve point defects, which immobilizes propagating interfaces. This rationalizes the formation of a high number of interphase boundaries in $Co_{49}Ni_{21}Ga_{30}$ alloys at elevated temperatures in region II (Figs. 4.4 and 4.5). In order to verify the temperature dependent microstructural changes, a companion sample was tested for one thousand pseudoelastic cycles repeatedly invoking a single phase-front and its growth during SIM at 40 °C. When the sample temperature was increased to 200 °C in the subsequent PE test, the specimen exhibited new interphase boundaries and their growth. This experiment suggests that the pinning of moving phase fronts is inherent to $Co_{49}Ni_{21}Ga_{30}$ alloys at elevated temperatures, which will lead to the formation of multiple variants.

As the coherent inter-phase boundaries are accompanied by the generation of defects such as dislocations during SIM transformation Otsuka & Wayman (1999), this increases the dislocation density and their distribution changing the microstructure of the original material. The defected regions and corresponding stress fields in the matrix nucleate the same oriented variants in subsequent phase transformations. Thus, the stable microstructure and favorable internal stresses acquired by the trained crystals improved the recoverability allowing the sample to exhibit pseudoelasticity in the temperature window of 400 °C (Figs. 4.7 and 4.8). Moreover, as the self-accommodating martensite is useful in applications that require energy absorption and vibration mitigation, the current results suggest that $Co_{49}Ni_{21}Ga_{30}$ alloys have the potential for such applications involving elevated temperatures and higher stresses. As many SMA applications often involve a large number of loading and unloading cycles, it is imperative to understand the cyclic deformation behavior of $Co_{49}Ni_{21}Ga_{30}$ alloys for their successful usage. Thus, the next chapter will deal with cyclic stability of these alloys at high temperatures.

4.4 Chapter Summary

In this chapter, the effects of repeated stress-induced phase transformation on the PE behavior of as-grown $Co_{49}Ni_{21}Ga_{30}$ [001]-oriented crystals were analyzed as a function of temperature under compression. The results revealed that dislocation activity, detwinning, point defects, SC-SRO and the associated martensite stabilization are the determining factors in the evolution of microstructure as well as the PE characteristics in $Co_{49}Ni_{21}Ga_{30}$ alloys. The main findings of this chapter can be summarized as follows:

1. The samples irrespective of their initial condition exhibit the same trends in the stress hysteresis evolution, yet, a strong dependency on test temperature prevails. A temperature region with a constant stress hysteresis is recorded below 120 and 180 °C for as-grown and trained crystals, respectively. Above these temperatures stress hysteresis increases monotonically in both cases, which is attributed to the ease of detwinning at elevated temperatures due to the high mobility of twin boundaries and the resultant shift of the unloading curve to lower stress levels.

2. During the training, the kinetic pinning-induced martensite stabilization is more pronounced at elevated temperatures due to high thermal-activity, which provides room for diffusion of point defects facilitating the pinning of propagating interfaces. This has resulted in the formation of multiple variants during the training process beginning from 120 °C giving way to the formation of self-accommodating martensite, thus the alloy exhibits lower transformation strains and serrated plus ascending stress-strain response.

3. The *in-situ* observations revealed that the nucleation and growth characteristics of SIM transformation on the microscopic as well as macroscopic scale are heterogeneous as the martensite growth proceeds via single propagating interface in room-temperature - 120 °C range and becomes quasi-homogeneous at elevated temperatures (>120 °C), which remained constant even after training in the $Co_{49}Ni_{21}Ga_{30}$ [001]-oriented crystal at all test-temperatures.

4. In the trained [001]-oriented single crystals, the stress required for the onset of yield of austenite is as high as 800 MPa at room-temperature, which is 20 folds higher than the critical stress needed for SIM. This is a necessary condition for obtaining large transformation strains by restricting the slip activity. This has in fact facilitated the samples to exhibit perfect pseudoelasticity at temperatures as high as 425 °C bringing about a large pseudoelastic window of more than 400 °C. This is remarkably larger than in NiTi-based, Cu-based and NiMnGa alloys marking $Co_{49}Ni_{21}Ga_{30}$ alloys as promising candidate material for numerous applications involving high stresses and elevated temperature.

Chapter 5

Cyclic Stability of $Co_{49}Ni_{21}Ga_{30}$ Single Crystals

5.1 Introduction

In this chapter, experimental results about the cyclic deformation behavior of single crystalline $Co_{49}Ni_{21}Ga_{30}$ SMAs are presented for compressive loading conditions at elevated temperatures. In Chapter 4, $Co_{49}Ni_{21}Ga_{30}$ alloys have been identified as the promising HTPM that can undergo a stress-induced phase transformation at temperatures as high as 425 °C with a complete shape recovery of at least 3 % strain. However, their success depends on the complete understanding of their cyclic stability, especially at high-temperatures. The results demonstrated a poor cyclic stability of as-grown crystals above 200 °C. Thus, appropriate heat-treatments were conducted to minimize the functional degradation, especially at elevated temperatures ($>$ 200 °C) as dislocation slip characteristics in these alloys can be modified by incorporating the disordered γ-phase (A1) and/or ordered γ'-phase ($L1_2$) in the ordered β-matrix (austenite, B2). In addition, the high strength, relatively low density and good corrosion resistance facilitate the utility of $Co_{49}Ni_{21}Ga_{30}$ alloys in various applications.

Moreover, these alloys are also considered as MSMA candidates owing to their natural ferromagnetism Craciunescu *et al.* (2002); Oikawa *et al.* (2001); Sato *et al.* (2003) that can demonstrate MSME as mentioned in Section 1.8 of Chapter 1. This phenomenon can occur at frequencies of the order of 1 kHz Marioni *et al.*

(2003), and thus stable cyclic behavior is paramount for the envisaged applications of MSMAs. Upon cyclic loading of conventional SMAs, stress-induced dislocation motion results in degradation of the PE properties. Similarly, magnetoplasticity could be a limiting factor for MSMAs since the MSME involves the motion of twinning dislocations, hence magnetic-field induced transformations may experience the same cyclic degradation as in the case of stress-induced phase transformations Müllner *et al.* (2003).

Cyclic deformation at ambient temperatures resulted in rapid accumulation of irrecoverable strains in the [123]-oriented crystals. However, after a few cycles the samples demonstrated cyclic stability with fully recoverable transformation. By contrast, the [001]-oriented crystals displayed excellent cyclic stability with hardly any change in stress-strain characteristics. The use of single crystals promotes a systematic bias of operant deformation mechanisms (martensite variant reorientation, detwinning, and dislocation slip) and their association with the cyclic stress-strain response (CSSR). The present results demonstrate that slip deformation accompanying the phase transformation and martensite stabilization play a major role in determining the cyclic transformation behavior. Macroscopically, dislocation slip and the resultant stabilized martensite result in the accumulation of residual strain with cycling and the corresponding internal stress fields alters the critical transformation stress levels softening the CSSR.

5.2 Cyclic Stress-Strain Response at Ambient Temperatures

Figures 5.1 and 5.2 present the cyclic PE response of the [001] and [123]-oriented samples, respectively. It is obvious from the data that the cyclic stress-strain responses are significantly different from each other. The compression behavior of the [001]-oriented crystal in Figure 5.1 remains relatively unchanged with cycling, i.e. it displays a constant transformation stress and stress hysteresis typically observed upon activation of a single martensite variant. By contrast, cyclic loading along the [123] orientation decreased the transformation stress by about 20 % while increasing the stress-strain slope as shown in Figure 5.2. As the critical

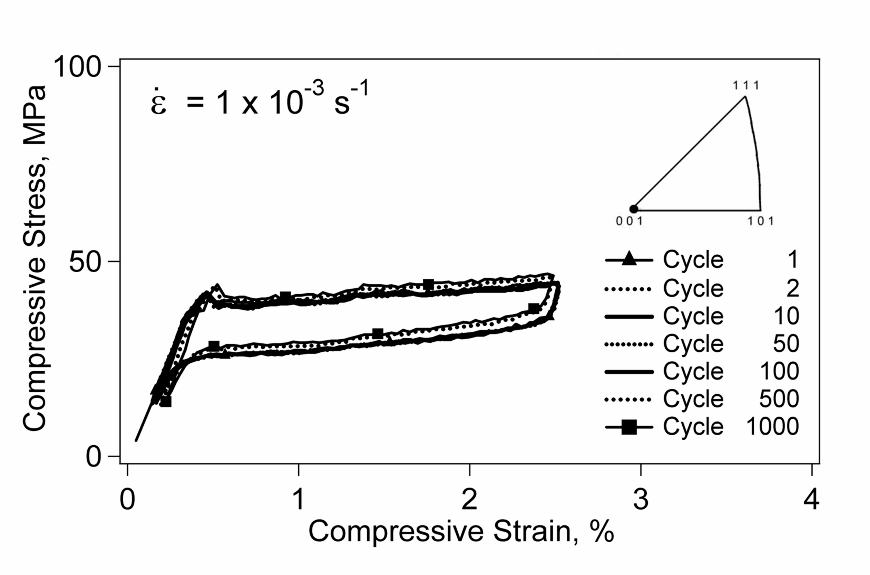

Figure 5.1: Cyclic stress-strain response at a constant maximum strain of 2.5 % in $Co_{49}Ni_{21}Ga_{30}$ [001]-oriented crystal at ambient temperature Dadda *et al.* (2008).

stress for the reverse transformation remained unchanged, the decrease in transformation stress for the forward transformation alters the stress hysteresis from cycle to cycle until it reaches saturation (Fig. 5.2). The instability in the cyclic behavior of the [123]-oriented crystal is attributed to the dislocations and their associated internal stress fields that help the transformation to occur at lower stress levels in subsequent cycles.

A quantitative measure of cyclic degradation resistance of a particular orientation is the permanent strain at a given cycle number. Therefore, permanent strains (ϵ_{PS}) as defined in Fig. 5.2 are plotted as a function of number of cycles in Figure 5.3. Fig. 5.3 demonstrates that the magnitude of ϵ_{PS} in case of the [001] orientation increases slightly and reaches a value of only 0.1 % after 1000 cycles. By contrast, ϵ_{PS} in the [123] orientation is accumulated rapidly in the early stages of cycling (1-50 cycles) and saturates after about 50 cycles at 0.9 %. Fig. 5.3 also shows the variation of stress hysteresis ($\Delta\sigma$) with the number of cycles, the magnitude of which decreases rapidly from 60 to 35 MPa in the [123] orientation, a 40

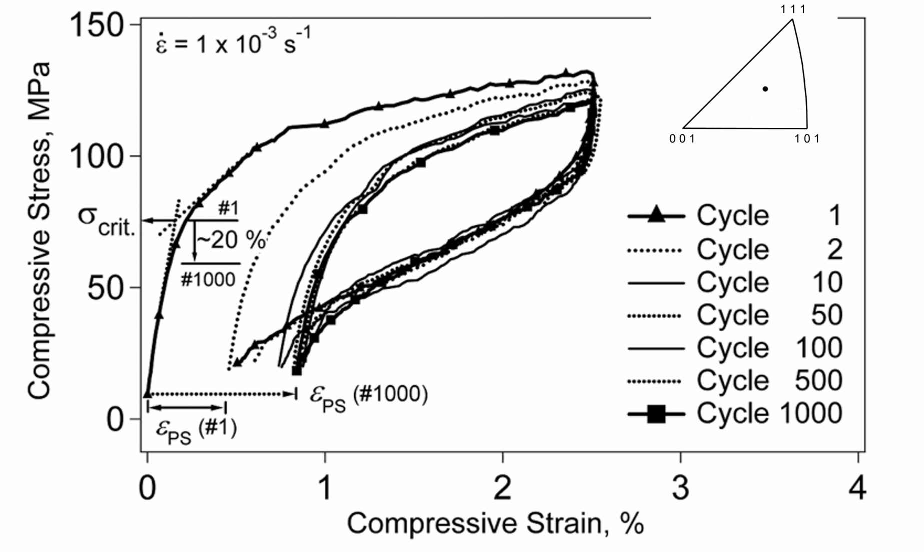

Figure 5.2: Cyclic stress-strain response at a constant maximum strain of 2.5 % in $Co_{49}Ni_{21}Ga_{30}$ [123]-oriented crystals at ambient temperature. The dashed lines in the first cycle indicate the approach adopted to calculate the critical stress for the forward transformation Dadda *et al.* (2008).

% reduction reaching saturation in about 50 cycles. Thus, the damping capacity of the [123]-oriented crystal is reduced initially but quickly reaches a steady state. The results demonstrate that prior training is an effective means to stabilize the PE characteristics in $Co_{49}Ni_{21}Ga_{30}$ alloys. The small change in $\Delta\sigma$ from 15 to 13 MPa with cycling in the [001]-oriented sample is an indication that only few dislocations are generated upon cyclic loading. Thus, interaction of dislocations with moving phase fronts and stabilization of martensite is less pronounced in this case.

The [001]-oriented crystal demonstrates a high resistance to cyclic degradation (Fig. 5.1), as dislocation slip is curtailed in this orientation due to zero Schmid factor(*cf.* Table 3.2). By contrast, the stress-strain characteristics of the [123]-oriented crystal evolves with cycling (Fig. 5.2). In the first phase of cycling (cycles 1 to 50), a dual phase austenite-martensite microstructure develops (Fig. 5.4) at the end of loading as the strain amplitude chosen is less than the expected maxi-

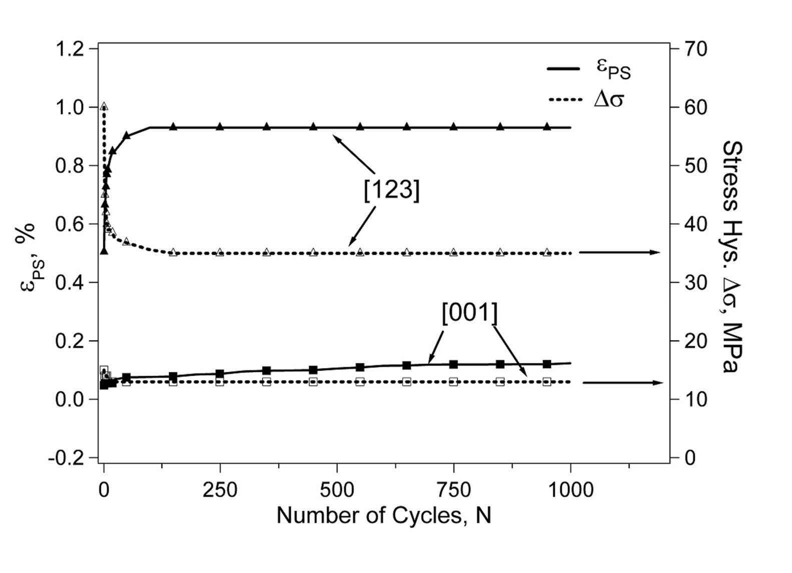

Figure 5.3: Accumulation of permanent strains, ϵ_{PS}, and evolution of stress hysteresis, $\Delta\sigma$, with the number of cycles in [001] and [123] oriented $Co_{49}Ni_{21}Ga_{30}$ single crystals at ambient temperatures Dadda *et al.* (2008).

mum transformation strain values for the [123] orientation (see Table 3.2). Upon unloading, the specimen will revert back to the austenite with a small fraction of stabilized residual martensite due to the ease of dislocation slip in the [123] orientation because of the non-zero Schmid factor (Table 3.2). As a result, permanent strains accumulate in each cycle and a stable dual phase microstructure is developed during cycling as recorded by TEM in Fig. 5.4. The strong internal stress fields associated with the microstructure promote and control the transformation. In other words, these residual or stabilized martensite regions (Fig. 5.4) act as pre-existing local nucleation sites for the transformation, lower the critical stress levels for the transformation in subsequent cycles, and thus, govern the evolution of the PE characteristics. As a result, the overall flow stress of the loading curve is altered in subsequent cycles causing a considerable amount of cyclic softening until the material behavior reaches a saturation point as seen in Fig. 5.2. Cyclic saturation will be reached when the generation of additional defects becomes negligible, and thus, the volume fraction of retained martensite remains

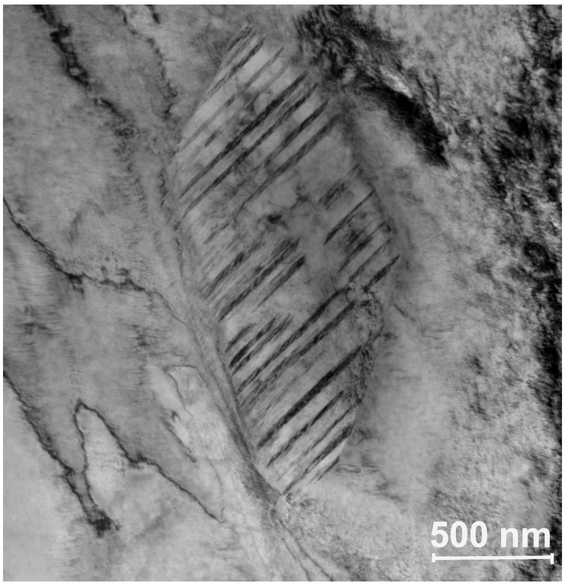

Figure 5.4: TEM images showing residual martensite after cyclic loading in $Co_{49}Ni_{21}Ga_{30}$ single crystals with [123] orientation. The pinned martensite in both cases appears to have strong stress fields as indicated by the contrast change at the martensite-austenite interface and substantial dislocation activity is also evident Dadda *et al.* (2008).

constant. When such a stable microstructure is induced due to repeated cycling, the material begins to exhibit a fully recoverable transformation (Fig. 5.2).

In addition, the long-range stress fields associated with the increase in dislocation density during cycling promote multiplicity of martensite CVPs. Consequently, the growth of martensite will become more difficult increasing the transformation stress-strain slope during cycling as seen in Fig. 5.2. Moreover, the increased dislocation density seems to suppress detwinning as a twinned martensite morphology is observed in the cyclically deformed sample in Figure 5.4. This will increase recoverability due to the substantial back stresses accommodated by the internally twinned martensite, which assist the reverse transformation. Thus, despite the initial changes in the PE behavior, the resistance to cyclic degradation is improved after some initial training cycles.

Based on the experimental results presented herein and theoretical values of

RSSFs and Schmid factors for slip deformation shown in Table 3.2 on page 50 in Chapter 3, it can be concluded that single crystals with low RSSF, i.e. unfavorable orientation of the martensite variants with respect to the applied stress state, and large Schmid factor, i.e. a favorable orientation of the slip system, demonstrate a large stress hysteresis, *cf.* the [123] orientation. In turn, the large stress hysteresis results in rapid evolution of cyclic stress-strain response, but reaches a steady state in terms of PE behavior after few initial cycles. On the other hand, the [001] orientation with large RSSF and zero Schmid factor exhibits constant PE characteristics through out cyclic loading. Therefore, a thorough study to understand the CSSR in this orientation at elevated temperatures has been carried out and presented in the following sections.

5.3 Cyclic deformation behavior at elevated temperatures

Figure 5.5 show the CSSR of $Co_{49}Ni_{21}Ga_{30}$ as-grown and untrained [001]-oriented crystal at different temperatures with a constant strain range($\Delta\epsilon$). The $\Delta\epsilon$ was chosen until an apparent elastic deformation of SIM sets in the curve (Fig. 3.10). It is clear from the figure the crystal exhibit stable CSSR without undergoing any cyclic degradation at temperatures below 100 °C, which is similar to that observed for [001]-oriented crystals with a strain range of 2.5 % strains in Fig. 5.1. However, the material exhibits a slight decrease in transformation stress levels during cycling at 100 °C, which can be connected to the favorable internal stress fields around the transformation defects. On the other hand, the CSSR at 200 °C degrades rapidly in terms of accumulation of residual strain (ϵ_{res}) of about 1 %, and the large drop in $\Delta\sigma$ and σ_{crit}^{For} values resulted in a small stress-strain hysteresis loop at the 1000^{th} cycle as shown in Fig. 5.5 for 200 °C.

Since Type II training has resulted in a stable microstructure (Fig. 4.9), one would expect a stable CSSR in Type II trained crystals. Figure 5.6 shows the CSSR of Type II trained crystal at 200 and 300 °C. As anticipated, Fig. 5.6 shows a stable CSSR that is achieved within the first 50 cycles, during this period a relatively lower degree of degradation took place compared to that recorded

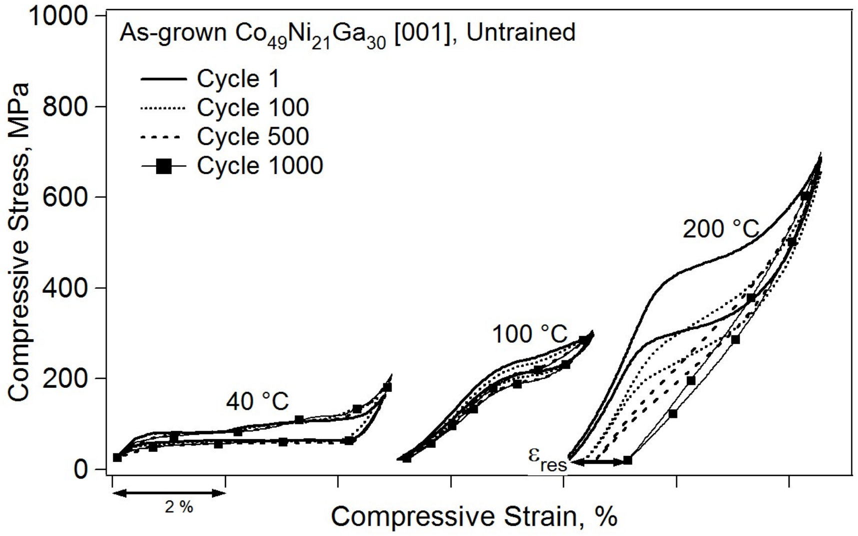

Figure 5.5: Cyclic stress-strain response of untrained as-grown $Co_{49}Ni_{21}Ga_{30}$ [001]-oriented crystal at different temperatures.

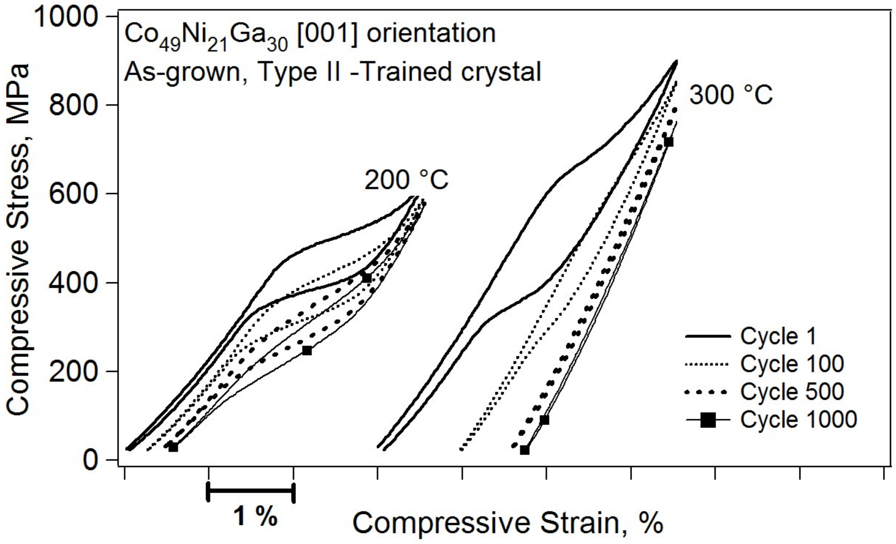

Figure 5.6: Cyclic stress-strain response of Type II trained as-grown $Co_{49}Ni_{21}Ga_{30}$ [001]-oriented crystal at different temperatures.

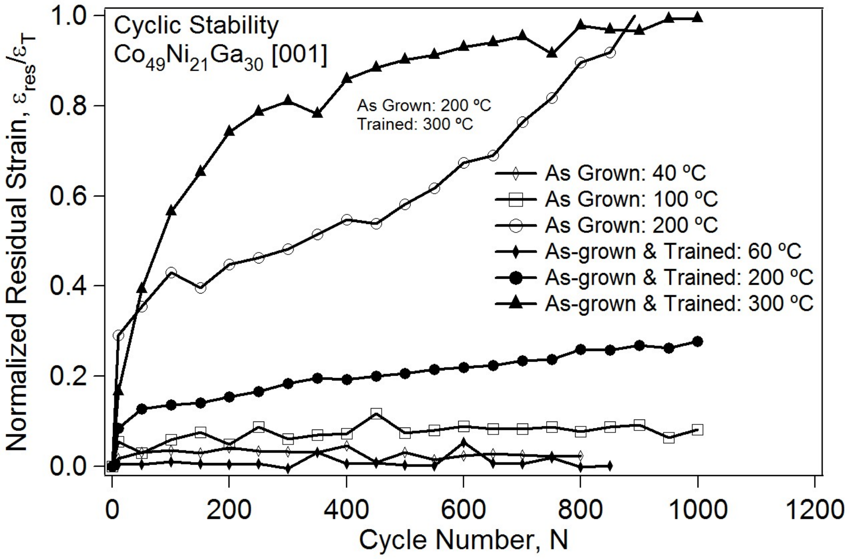

Figure 5.7: Normalized residual strains ($\epsilon_{res}/\epsilon_T$) with the number of cycles in as-grown $Co_{49}Ni_{21}Ga_{30}$ [001]-oriented crystals at different temperatures.

for the untrained crystal at 200 °C in Fig. 5.5. Finally, the material degraded completely without undergoing any SIM transformation at 300 °C resulting in linear stress-strain hysteresis loops after 500 cycles as seen in Fig. 5.6. This is further clarified in Figure 5.7 by plotting the normalized residual strains, $\epsilon_{res}/\epsilon_T$ a dimensionless quantity, with the number of cycles. Fig. 5.7 demonstrates that the $\epsilon_{res}/\epsilon_T$ values accumulates rapidly and reaches a saturation within the first few cycles for all the crystals shown here and the magnitude of which is a clear measure of the degree of cyclic degradation in $Co_{49}Ni_{21}Ga_{30}$ alloys. The material is completely degraded in terms of its functional properties when $\epsilon_{res}/\epsilon_T$ reaches unity, as it happened for the case of as-grown crystal at 200 °C and the trained crystal at 300 °C, which means a complete suppression of SIM transformation is taking place in the material upon cycling.

However, the residual strains accumulated in the as-grown crystal shown in Fig. 5.7 were recovered upon heating the sample to 400 °C but some of them were retained in the specimen, when it was cooled down to room-temperature. This was not the case with the trained as-grown crystal, which was cycled at

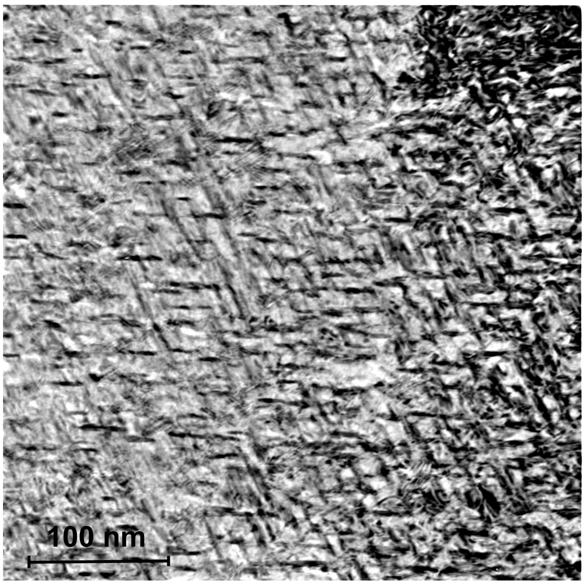

Figure 5.8: A bright field TEM image of Type II trained $Co_{49}Ni_{21}Ga_{30}$ [001]-oriented crystal after 1000 cycles at 300 °C shown in Fig. 5.6.

300 °C, thus, subsequent TEM investigations were made on this specimen to understand the deformation mechanisms and evolution of the microstructure. Figure 5.8 shows the TEM image of the fatigued sample at 300 °C and reveals the formation of fine precipitates (γ-phase) in the matrix. From the particle analysis of the dark field image shown in Fig. 5.9, the volume fraction of γ phase was 35-40 %. Moreover, Figure 5.10 shows a microstructure of a sample heat-treated for 36 hours at 300 °C demonstrating a high density of γ precipitates in the β matrix. Note that the fatigue test at 300 °C shown in Fig. 5.6 took 36 hours for the completion. These studies point out that the β-matrix of as-grown $Co_{49}Ni_{21}Ga_{30}$ crystals is unstable at elevated temperatures and decomposes into non-transformable γ-phase.

The cyclic behavior at elevated temperatures (Figs. 5.5, 5.6 and 5.7) suggest that the wider the stress hysteresis the faster the cyclic degradation, which is similar to that observed for [123]-oriented crystals discussed earlier. Therefore, the crystals operating in region II (Fig. 4.12 on page 66 in Chapter 4) degrades rapidly under cyclic loading conditions. This is consistent with the aforementioned crite-

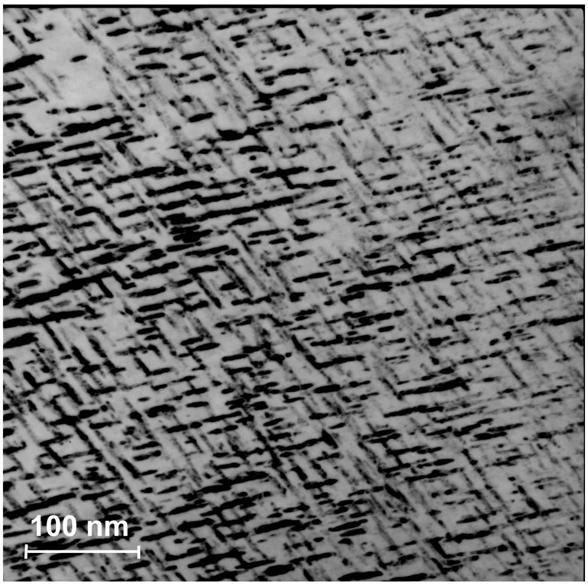

Figure 5.9: The corresponding dark fields image shown in Fig. 5.8. The contrast has been reversed to better display the γ particles in the matrix.

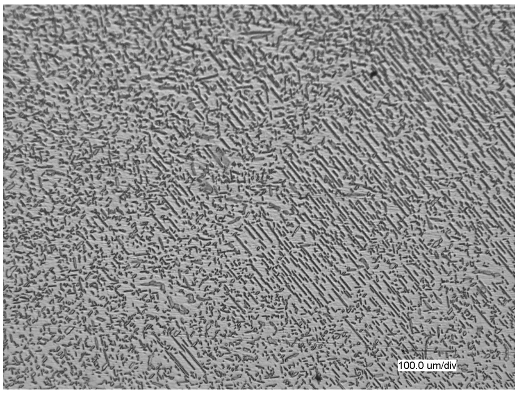

Figure 5.10: A general microstructural morphology of $Co_{49}Ni_{21}Ga_{30}$ sample heat-treated for 36 hours at 300 °C and air cooled.

rion for the occurrence of cyclic degradation based on stress hysteresis and the orientation. The large hysteresis in region II was associated with the high dislocation density, which is needed to dissipate the elastic stored energy through the relaxation of coherency stresses at the inter-phase boundaries, detwinning, diffusion of point-defects to interfaces pinning their propagation and the incoming martensite stabilization. Under these circumstances, any SMA material subjected to repeated transformations, especially to cyclic loading-unloading conditions, will cease to exhibit any functional properties. Furthermore, the decomposition of the material into other non-transformable phases such as γ at elevated temperatures added to the effect, suppressing the transformation completely as seen in Fig. 5.6 at 300 °C. This has offered a motivation to carry out several aging treatments based on the information provided elsewhere by Schlagel *et al.* (2004), and the results that demonstrate improved cyclic stability are discussed as follows.

Figure 5.11 shows micrographs of heat treated samples, revealing the distribution of γ particles in the matrix. As expected the samples aged for longer period, *i.e.* 900 °C for 24 hours, possess higher volume fraction of γ of about 17 vol. % (Fig. 5.11b), while the other sample contains 5 vol. % secondary phase (γ) in the matrix (Fig. 5.11a).

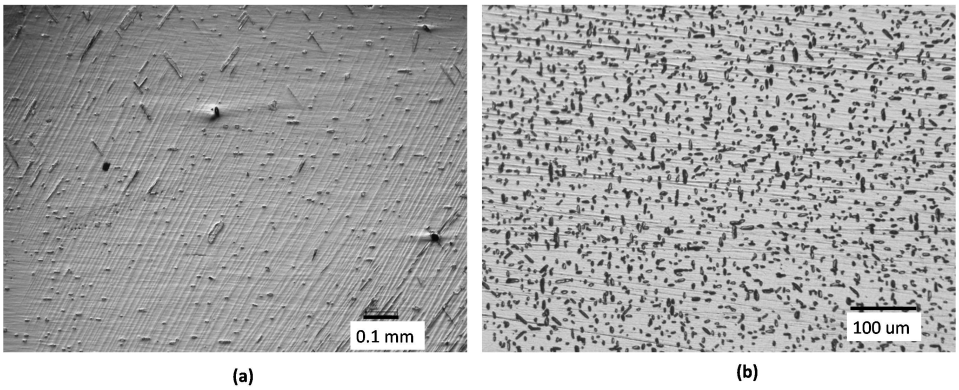

Figure 5.11: Micrographs of solutionized $Co_{49}Ni_{21}Ga_{30}$ single crystal samples heat-treated for (a) 4 hours at 1100 °C and water quenched and (b) 24 hours at 900 °C and water quenched. Solutionization was conducted at 1200 °C for 4 hours followed by water quenching.

The pseudoelastic behavior of Type II trained $Co_{49}Ni_{21}Ga_{30}$ aged samples and its dependency on the heat-treatments are emphasized with the aid of CC-curves shown in Figure 5.12. Type II training has been employed in order to stabilize the pseudoelastic cyclic behavior as seen before in the case of as-grown crystals. Interestingly, the deviation from linearity in the stress range of 650-750 MPa clearly indicates the onset of plasticity in the material, which in fact limits pseudoelasticity and its temperature range in $Co_{49}Ni_{21}Ga_{30}$ alloys. Thus, the suppression of slip deformation via austenite strengthening is a necessary condition to obtain a large PE window in these alloys. Moreover, the dependency of M_s temperatures at zero stress levels, PE window and CC-slopes can be attributed to the change in chemical composition of austenite due to the precipitation process, and the results are summarized in Table 5.1.

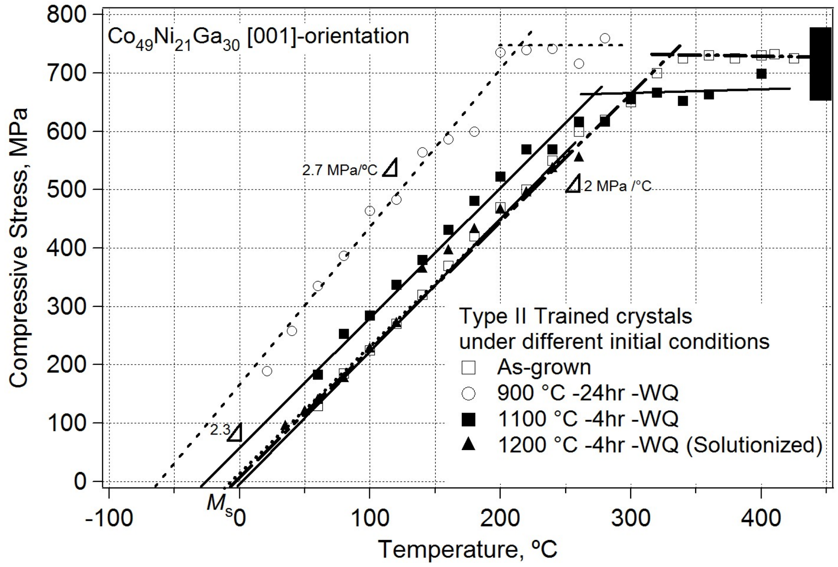

Figure 5.12: Clausius-Clapeyron curves for different heat-treated $Co_{49}Ni_{21}Ga_{30}$ [001]-oriented samples after Type II training.

Table 5.1 shows that the higher the volume fraction of γ-phase the higher the CC-slope, which is linked to strengthening of austenite. This will also change the chemical composition of the matrix as the precipiation requires Co-depletion to form the Co-rich γ phase, which rationalizes the decrease in M_s temperatures to -75 °C in the case of material with the high amount of γ from -5 °C in the case of as-grown or solutionized case (Table 5.1).

Table 5.1: Clausius-Clapeyron slopes, volume fraction of γ phase, M_s temperatures and pseudoelastic temperature window for Type II trained $Co_{49}Ni_{21}Ga_{30}$ [001]-oriented single crystals with different initial heat-treated conditions.

Type II_Trained $Co_{49}Ni_{21}Ga_{30}$ Init_Cond.	CC-slope (MPa/°C)	Vol_Frac γ-phase (%)	M_s (°C)	PE-window (°C)
As-grown	2	5	-5	400
1200_°C _4hrs	2	0	-5	> 300
1100_°C _4hrs	2.3	7	-25	325
900_°C _24hrs	2.7	17	-75	325

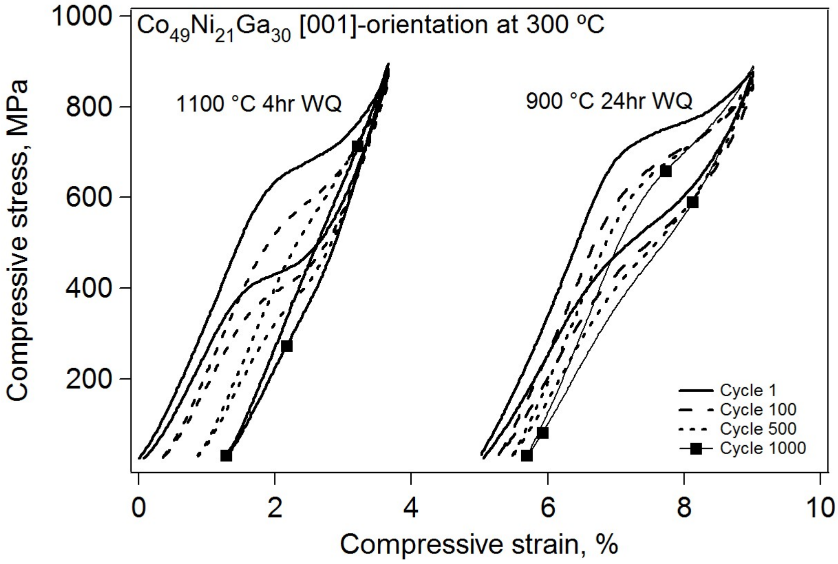

Figure 5.13: Cyclic stress-strain response of heat-treated $Co_{49}Ni_{21}Ga_{30}$ [001]-oriented single crystals at 300 °C after Type II training.

Figure 5.13 shows the pseudoelastic cycling results of heat-treated and Type II trained samples at 300 °C. The figure clearly demonstrates that the sample heat treated at 900 °C for 24 hours reaches a stable cyclic behavior after some degree of degradation within the first few cycles. The stable behavior is attributed to the increase in matrix strength due to the high amount of secondary phase particles

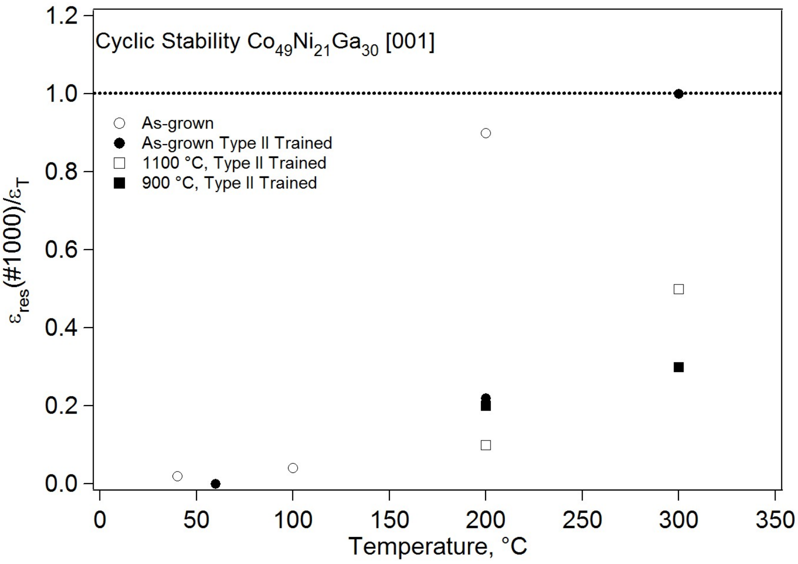

Figure 5.14: Normalized residual strains at the 1000^{th} cycle indicating the limits of cyclic stability in $Co_{49}Ni_{21}Ga_{30}$ [001]-oriented single crystalline shape memory alloys.

in the material, which might have curtailed the dislocation activity during the cycling.

The analysis about the cyclic stability of $Co_{49}Ni_{21}Ga_{30}$ [001]-oriented single crystals under different thermomechanical conditions is summarized in Figure 5.14. This was done by plotting the normalized residual strain at the 1000^{th} cycle, $\epsilon_{res}^{1000}/\epsilon_T$, as a function of temperature. This figure provides the information about the temperature ranges in which the $Co_{49}Ni_{21}Ga_{30}$ alloys can be applied safely with minimum cyclic degradation (since $\epsilon_{res}^{1000}/\epsilon_T$ is < 0.2), after some prior thermomechanical treatments.

In addition, the material with high CC-slopes reaches the yield levels of about 700 MPa very quickly (Fig. 5.12), thus, depressing the PE temperature range. The opposite is true in the case of those $Co_{49}Ni_{21}Ga_{30}$ alloys with low CC-slopes. This underlines that the strengthening of matrix in an attempt to curtail the dislocation activity is pivotal to increase the PE temperature window in $Co_{49}Ni_{21}Ga_{30}$ alloys. This can be achieved through incorporating fine coherent γ' (Ni_3Ga) precipitates in the matrix by adopting appropriate heat-treatments. Recently, a two-fold increase in transformation stress levels $Co_{35}Ni_{35}Al_{30}$ alloy system with fine subnanometer coherent γ':Ni_3Al precipitates has been found by our group. Therefore, this research can be extended further by optimizing the thermo-mechanical treatments to improve the high-temperature capability of $Co_{49}Ni_{21}Ga_{30}$ alloys.

5.4 Chapter Summary

In this chapter, cyclic deformation behavior of $Co_{49}Ni_{21}Ga_{30}$ single crystals at ambient as well as at elevated temperatures has been examined and the important findings can be summarized as follows:

1. In the [001] orientation, dislocation motion is curtailed inhibiting slip due to the unfavorable {110} <001> slip systems. Hence, [001]-oriented crystals demonstrate near perfect pseudoelastic stress-strain behavior with excellent cyclic stability, i.e. small frictional dissipation and negligible influence of strain history on the cyclic behavior. The narrow hysteresis of only 15 MPa, the lack of dislocation slip and suppression of detwinning observed, all suggest that polycrystalline aggregates with a prominent [001] texture component are highly attractive for applications.

2. In the case of the sample with [123] orientation, dislocation activity during the phase transformation accounts for the rapid evolution of the stress-strain response during the early stage of cycling loading and the accumulation of permanent strains. The stress fields of the dislocations promote the forward transformation and induce cyclic softening. Dislocations impede the reverse transformation, interact with the detwinning process and stabilize the stress-induced martensite upon unloading.

3. After only 50 cycles, the [123]-oriented $Co_{49}Ni_{21}Ga_{30}$ single crystal exhibited stable cyclic behavior with fully recoverable transformation. In addition, ease of dislocation generation, formation of multiple CVPs, detwinning and martensite stabilization are the rationale behind the large stress hysteresis of 70 MPa in the [123]-oriented $Co_{49}Ni_{21}Ga_{30}$ single crystals. The resultant

high damping capacity of a polycrystalline material with a strong [123] texture component would make the material attractive for applications involving energy absorption and vibration mitigation.

4. In $Co_{49}Ni_{21}Ga_{30}$ [001]-oriented crystal, a stable cyclic stress-strain response is observed below 200 °C regardless of the initial condition of the sample. After initial thermomechanical training, the samples tested at 200 °C exhibit a decrease in transformation stresses and accumulation of residual strains initially but reach a stable response within the first few hundred cycles. However, the as-grown samples are unstable at higher temperatures (300 °C) as the β-matrix tends to decompose into the Co-rich γ phase completely suppressing the SIM transformation. Consequently, a rapid cyclic degradation occurred at elevated temperature due to the complete suppression of SIM transformation at 300 °C.

5. The cyclic response of $Co_{49}Ni_{21}Ga_{30}$ [001]-oriented crystals at 300 °C is improved by heat-treating the samples at 900 °C for 24 hours after initial solutionization treatment at 1200 °C for 4 hours, which was in fact achieved through strengthening of the matrix by incorporating fine γ precipitates.

6. The cyclic stress-strain response in the $Co_{49}Ni_{21}Ga_{30}$ single crystals that exhibit wide stress hysteresis, which is either inherent to the crystallographic orientation or due to the operating temperature, will degrade rapidly and reaches a saturation, while in those samples with narrow hysteresis is stable without undergoing any cyclic degradation in terms of accumulation of residual strains and drop in observed stress hysteresis.

Chapter 6

Summary & Future Research

In the present study, the research regarding different aspects concerning newly developed Co-base SMAs with reference to their high-temperature capability was carried out. A thorough experimental study about mechanical and functional properties of a $Co_{49}Ni_{21}Ga_{30}$ and $Co_{38}Ni_{33}Al_{29}$ (in at.%) single crystalline alloys was executed understanding the effects due to crystallographic orientation and thermomechanical treatments. In particular, the deformation mechanisms involved in the material's stress-strain behavior during thermomechanical training was investigated; the resultant high-temperature pseudoelasticity was studied together with the variation in its characteristic hysteresis as a function of temperature. Furthermore, the effects of training on the pseudoelastic behavior were evaluated in terms of its temperature range in correlation with the microstructural evolution. The latter was achieved by using systematic *in-situ* microscopy observations at high-temperatures. This information is necessary to model the heterogeneous/homogeneous transformation behavior of $Co_{49}Ni_{21}Ga_{30}$ and $Co_{38}Ni_{33}Al_{29}$ alloys. Many of the experimental investigations summarized above, were executed on both as-grown and thermomechanically treated material and the results are compared in order to evaluate their mechanical and functional performance in order to develop new $Co_{49}Ni_{21}Ga_{30}$ and $Co_{38}Ni_{33}Al_{29}$ high-temperature pseudoelastic materials.

The [001] and [110] oriented $Co_{38}Ni_{33}Al_{29}$ single crystals subjected to high cooling rates following a solutionization treatment at 1350 °C for 24 hours exhibit large phase transformation strains of about 4.1 % under compressive stress levels as low as 50 MPa. In the case of [110] oriented single crystals this strain value exceeds the theoretical CVP transformation strain, indicating a significant contribution of detwinning strains to the overall phase transformation strain. Moreover, near-perfect pseudoelasticity above the A_f temperature was obtained in compression tests with a maximum pseudoelastic strain of about 4.3 %. The $Co_{38}Ni_{33}Al_{29}$ single crystals investigated in this work demonstrate a large pseudoelastic window of more than 250 °C, good cyclic stability and trainability with a maximum TWSME strain of 2.7%.

The TWSME strain obtained for the [001]-oriented air cooled $Co_{38}Ni_{33}Al_{29}$ samples constitutes an evidence of the substantial role of the ductile γ-phase for trainability in the absence of pronounced dislocation activity. Otherwise, during thermal cycling, due to the development of plasticity in orientations that are more favorable for the dislocation activity, an internal stress field was created; this stress field interact with the phase transformation allowing the formation of a preferentially oriented martensitic structures during cooling. This benefits the formation of the TWSME in the material remembering a low temperature shape. Therefore, the results emphasize the need for texturing polycrystalline aggregates of the current material with an optimum γ-phase volume fraction to achieve high performance in $Co_{38}Ni_{33}Al_{29}$ alloys according to the application demand.

In as-grown $Co_{49}Ni_{21}Ga_{30}$ specimens, the low critical transformation stress due to high RSSF value, *i.e.* low CC-slope, high slip resistance in the austenite due to zero Schmid factor and B2 atomic ordering allow for excellent transformation recoverability with a large PE temperature range of about 325 °C when loaded in the [001] direction. Moreover, the [001]-oriented $Co_{49}Ni_{21}Ga_{30}$ single crystals exhibit 4.4 % transformation strains at compressive stress levels as low as 4 MPa, and a fully recoverable 4.3 % pseudoelastic strain at low temperatures. The thermomechanical training resulted in a stable microstructure improving the transformation recoverability, which in turn resulted in a large PE window of 400 °C with recoverable strain of 3 % strains in the temperature range of 40-425 °C.

In addition, the pseudoelasticity, especially the hysteretic behavior of the material as a function of temperature was analyzed with the help of *in-situ* microscopy as this information is required to control the necessary parameters in designing $Co_{49}Ni_{21}Ga_{30}$ actuators that utilize the pseudoelastic phenomenon. The

$Co_{49}Ni_{21}Ga_{30}$ [001]-oriented samples irrespective of their initial condition exhibit the same trends in the stress hysteresis evolution, yet, a strong dependency of hysteresis on test temperatures has also prevailed. A temperature region with a constant stress hysteresis is recorded below 120 and 180 °C for as-grown and trained crystals, respectively. Above these temperatures, the stress hysteresis increases monotonically to a maximum of 350 MPa in both cases, which is attributed to the ease of detwinning due to high mobility of twin boundaries (because of high thermal activity) and the resultant shift of the unloading curve to lower stress levels. Moreover, the *in-situ* observations revealed that the nucleation and growth characteristics of SIM transformation on the microscopic as well as macroscopic scale are heterogeneous as the martensite growth proceeds via a single propagating interface in the room-temperature to 120 °C range and becomes quasi-homogeneous at elevated temperatures (>120 °C), which remained constant even after training at all test temperatures (40-425 °C).

During the training, the kinetic pinning induced martensite stabilization is more pronounced at elevated temperatures due to high thermal-activity, which provides room for diffusion of point defects facilitating the pinning of propagating interfaces. This has resulted in the formation of multiple variants beginning from 120 °C giving way to the formation of self-accommodating martensite. Thus the alloy exhibits lower transformation strains and ascending stress-strain response with serrated features at elevated temperatures. Moreover, due to the training, the martensite structure was stabilized by the residual stress field around the defects that were generated during the repeated transformation. As consequences, an increase in the phase transformation temperatures (M_s) and in the slope of the stress plateau together with a reduction in the stress for the onset of SIM are observed. A $Co_{49}Ni_{21}Ga_{30}$ actuator could also be useful for the production of composite materials for shape and vibration control opening a new perspective in many industrial applications owing to its ability to exhibit large stress hysteresis of about 350 MPa.

In addition, the training methods that involve isothermal loading-unloading cycles at different temperatures brought about a stable cyclic stress-strain response (CSSR) in $Co_{49}Ni_{21}Ga_{30}$ alloys at temperatures as high as 200 °C. However, at 300 °C the material degraded rapidly due to the precipitation of untransformable γ-phase and the consequently suppressing the SIM transformation in these alloys. This phenomenon was curtailed in the heat-treated samples at 900 °C for 24 hours followed by water-quenching and finally a stable CSSR was achieved at 300 °C. Moreover, a correlation between the size of stress hysteresis and CSSR has been established in $Co_{49}Ni_{21}Ga_{30}$ alloys: the samples with wide stress hysteresis, which is either inherent to the crystallographic orientation or due to the operating temperature, exhibit rapid degradation during the first phase of cycling (within the first few hundred cycles) and reach a saturation, while in those specimens that demonstrate a narrow hysteresis (< 50 MPa) a stable CSSR is observed without any cyclic degradation in terms of accumulation of residual strains and decrease in transformation stress levels and stress hysteresis values.

Future studies could be oriented to understand the cyclic stability, fatigue behavior and transformation reproducibility and recoverability with reference to pseudoelastic behavior of $Co_{38}Ni_{33}Al_{29}$ alloys at elevated temperatures, as these issues have not been addressed so far. Further studies can be focused on the optimization of thermomechanical treatments of $Co_{49}Ni_{21}Ga_{30}$ alloys in order to increase the matrix strength and ductility, thereby, improve their high-temperature capability above 400 °C. The experimental data acquired in this study can be used to develop a constitutive model which is capable of simulating the shape memory and pseudoelastic behavior of $Co_{38}Ni_{33}Al_{29}$ and $Co_{49}Ni_{21}Ga_{30}$ alloys. Future work should be carried out to analyze the abilities of the proposed approach in predicting the hysteretic behavior of the material under more complex loading conditions, such as simultaneous variation of both stress and temperature, through specific experimental tests. Furthermore, to increase the practical usefulness of the proposed method in controlling $Co_{38}Ni_{33}Al_{29}$ and $Co_{49}Ni_{21}Ga_{30}$ actuators, which are usually driven by an electric current, further studies should be carried out to improve the model with the relationship current versus temperature.

One can draw SMA wires out of these alloys with sufficient amount of soft γ phase in the material, then bring back the material to the desired microstructure by using appropriate heat-treatments. Thus, future work should also focus on the robust thermomechanical characterization of these alloys under tensile loading conditions. Currently, some investigations that include analysis of tension-compression asymmetry are underway. It is also found that tension brought about the lowest CC-slope of about 0.8 MPa/°C in [001]-oriented solutionized $Co_{49}Ni_{21}Ga_{30}$ samples, which can be exploited to achieve a large PE-temperature window in these alloys.

Acknowledgements

First of all, many thanks to my adviser Prof. Hans J. Maier, whose academic and financial support over the years made this research possible. His enthusiasm and collaborative spirit helped to create a great environment, and his amazingly broad knowledge and experience gave my research both direction and inspiration.

I would also like to thank Prof. Ibrahim Karaman, Department of Mechanical Engineering, Texas A&M University, Texas, USA. He provided me many valuable suggestions, ideas and useful discussions that improved the quality of this research study.

I would also like to thank Prof. Yuri V. Chumlyakov, Siberian Physical Technical Institute, Tomsk, Russia, for providing the single crystals, who also shared his ideas and provided me with constructive advice.

I gratefully acknowledge the support of Deutsche Forschungsgemeinschaft (DFG), US Army Research Office (DAAD 19-02-1-0261, W911NF-06-1-0319) US National Science Foundation - Division of Materials Research (0244126, 0805293), and the US Civilian Research and Development Foundation (RE1-2525-TO-03, RUE1-2690-TO-05).

It is a pleasure to acknowledge the experimental assistance that I received from Kristina Duschik, Barbara Flöing-Herring and Sabrina Sprünken, which has been very helpful in learning new techniques and approaches.

Very thanks to my girlfriend Neeraja that has accepted faithfully and gladly the challenges and uncertainties associated with the life of a doctoral student; her love and patience are for me essential.

References

Abeyaratne, R. & Knowles, J.K. (1993). A continuum model of a themoelastic solid capable of undergoing phase transitions. *J Mech Phys Solids*, **41-3**, 541–571. 51, 59

Brown, P.J., Ishida, K., Kainuma, R., Kanomata, T., Neumann, K.U., Oikawa, K., Ouladdiaf, B. & Ziebeck, K.R.A. (2005). Crystals structures and phase transitions in ferromagnetic shape memory alloy based on Co-Ni-Al and Co-Ni-Ga. *Journal of Physics: Condensed Matter*, **17**, 1301–1310. 18

Canadinc, D., Dadda, J., Maier, H.J., Karaman, I., Karaca, H.E. & Chumlyakov, Y.I. (2007). On the role of the cooling rate and crystallographic orientation on the shape memory properties of CoNiAl single crystals under compression. *Smart Materials and Structures*, **16**, 1006–1015. 2, 14, 18, 26, 27, 29, 32, 34, 40, 41, 43

Chernenko, V.A., L'vov, V., Pons, J. & Cesari, E. (2003). Superelasticity in high-temperature NiMnGa alloys. *Journal of Applied of Physics*, **93**, 2394. 48

Chernenko, V.A., Pons, J., Cesari, E. & Zasimchuk, I.K. (2004). Transformation behaviour and martensite stabilization in the ferromagnetic Co-Ni-Ga heusler alloy. *Scripta Materialia*, **50**, 225–229. 14, 18, 52

Chernenko, V.A., Besseghini, S., Villa, E., Gambardella, A. & Prez-Landazabal, J.I. (2007). Elastic and superelastic properties of $Co_{49}Ni_{22}Ga_{29}$ single crystal. *Applied Physics Letters*, **90**, 201914. 18

Chu, T.C., Ranson, W.F., Sutton, M.A. & Peters, W.H. (1985). Applications of Digital-Image-Correlation Techniques to Experimental Mechanics. *Experimental Mechanics*, **25**, 232–244. 21, 23

Craciunescu, C.M., Kishi, Y., Graef, M.D., Lograsso, T.A. & Wuttig, M. (2002). Cobalt-base ferromagnetic shape memory alloys. *Smart Structures and Materials, SPIE*, **4669**, 235–244. 14, 74

Dadda, J., Canadinc, D., Maier, H.J., Karaman, I., Karaca, H.E. & Chumlyakov, Y.I. (2006a). Stress-strain-temperature behaviour of [001] single crystals of $Co_{49}Ni_{21}Ga_{30}$ ferromagnetic shape memory alloys under compression. *Philosophical Magazine A*, **87-16**, 2313–2322. 2, 14, 18, 36, 37

Dadda, J., Maier, H.J., Karaman, I., Karaca, H.E. & Chumlyakov, Y.I. (2006b). Pseudoelasticity at elevated temperatures in [001] oriented $Co_{49}Ni_{21}Ga_{30}$ single crystals under compression. *Scripta Materialia*, **55**, 663–666. 2, 14, 18, 38, 45, 53, 63, 67

Dadda, J., Maier, H.J., Niklasch, D., Karaman, I., Karaca, H.E. & Chumlyakov, Y.I. (2008). Pseudoelasticity and cyclic stability in $Co_{49}Ni_{21}Ga_{30}$ shape memory alloy single crystals at ambient temperature. *Metallurgical and Materials Transactions A*, **39A**, 2026–2039. 2, 18, 37, 46, 47, 53, 57, 67, 76, 77, 78, 79

Dadda, J., Maier, H.J. & Karaman, I. (2009). High-temperature pseudoelasticity of co-ni-ga shape memory alloy single crystals under compression. *SMST2007 Tsukuba, Japan, Conference Proceedings*, 659–666. 2, 18, 44

Daly, S., Ravichandran, G. & Bhattacharya, K. (2007). Stress-induced martensitic phase transformation in thin sheets of nitinol. *Acta Materialia*, **55**, 3593–3600. 57

Duerig, T.W., Melton, K.N., Stöckel, D. & Wayman, C.M. (1990). *Egineering aspects of Shape Memory Alloys*. Butterworth-Heinemann. 3, 4, 12, 14

Efstathiou, C., Sehitoglu, H., Johnson, A.J.W., Hamilton, R.F., Maier, H. & Chumlyakov, Y. (2004). Large reduction in critical stress in CoNiAl upon repeated transformation. *Scripta Materialia*, **51**, 979–985. 14, 18, 27, 40

Eggeler, G., Hornbogen, E., Yawny, A., Heckmann, A. & Wagner, M. (2004). Structural and functional fatigue of NiTi shape memory alloys. *Materials Science and Engineering A*, **378**, 24–33. 13

Firstov, G.S., Humbeeck, J.V. & Koval, Y.N. (2004a). Comparison of high temperature shape memory behaviour for ZrCu-based, TiNiZr and TiNiHf alloys. *Scripta Materialia*, **50**, 243–248. 15

Firstov, G.S., Humbeeck, J.V. & Koval, Y.N. (2004b). High-temperature shape memory alloys some recent developments. *Materials Science and Engineering A*, **378**, 2–10. 14

Gall, K. & Maier, H.J. (2002). Cyclic deformation mechanisms in precipitated NiTi shape memory alloys. *Acta Materialia*, **50**, 4643–4657. 13

Gall, K., Sehitoglu, H., Chumlyakov, Y.I. & Kireeva, I.V. (1999). Pseudoelastic cyclic stress-strain response of over-aged single crystal Ti-50.8at%Ni. *Scripta Materialia*, **40**, 7–12. 13, 53

Hamilton, R.F., Sehitoglu, H., Chumlyakov, Y. & Maier, H.J. (2004). Stress dependence of the hysteresis in single crystal NiTi alloys. *Acta Materialia*, **52**, 3383–3402. 14, 30, 32, 33, 40

Hamilton, R.F., Sehitoglu, H., Efstathiou, C., Maier, H.J., Chumlyakov, Y. & Zhang, X.Y. (2005). Transformation of CoNiAl single crystals in tension. *Scripta Materialia*, **53**, 131136. 14, 18

Hamilton, R.F., Sehitoglu, H., Efstathiou, C., Maier, H.J. & Chumlyakov, Y. (2006). Pseudoelasticity in CoNiAl single and polycrystals. *Acta Materialia*, **54**, 587–599. 18, 40

Ishida, K., Kainuma, R., Ueno, N. & Nishizawa, T. (1991). Ductility enhancement in NiAl (B2)-base alloys by microstuctural control. *Metallurgical Transactions A*, **22A**, 441–446. 26

Kainuma, R., Ise, M., Jia, C.C., Ohatani, H. & Ishida, K. (1996). Phase equilibria and microstuctural control in the NiCoAl system. *Intermetallics*, **4**, S151–S158. 15, 16

Karaca, H.E., Karaman, I., Lagoudas, D.C., Maier, H.J. & Chumlyakov, Y.I. (2003). Recoverable stress-induced martensitic transformation in a ferromagnetic Co-Ni-Al alloy. *Scripta Materialia*, **49**, 831–836. 15, 18, 29, 39, 48

Karaca, H.E., Karaman, I., Chumlyakov, Y.I., Lagoudas, D.C. & Zhang, X. (2004). Compressive response of a single crystalline CoNiAl shape memory alloy. *Scripta Materialia*, **51**, 261–266. 18, 29, 40

Karaman, I., Karaca, H.E., Basaran, B., Lagoudas, D.C., Chumlyakovc, Y. & Maier, H. (2006). Stress-assisted reversible magnetic field-induced phase transformation in Ni_2MnGa magnetic shape memory alloys. *Scripta Materialia*, **55**, 403–406. 14

Kato, H., Ozu, T., Hashimoto, S. & Miura, S. (1999). Cyclic stress-strain response of superelastic Cu-Al-Mn alloy single crystals. *Materials Science and Engineering A*, **264**, 245–253. 13

Kimura, Y., Miura, S., Suzuki, T. & Mishima, Y. (1994). Microstructure and mechanical properties of two-phase alloys based on the b2 -type intermetallic compound coal in the co-ni-al ternary system. *Materials Transactions (JIM)*, **35-11**, 800–807. 15, 26

Kustov, S., Pons, J., Cesari, E. & Humbeeck, J.V. (2004a). Pinning-induced stabilization of martensite part I. stabilization due to static pinning of interfaces. *Acta Materialia*, **52**, 3075–3081. 70

KUSTOV, S., PONS, J., CESARI, E. & HUMBEECK, J.V. (2004b). Pinning-induced stabilization of martensite part II. kinetic stabilization in Cu-Zn-Al alloy due to pinning of moving interfaces. *Acta Materialia*, **52**, 3083–3096. 70

LI, Y.X., LIU, H.Y., MENG, F.B., YAN, L.Q., LIU, G.D., DAI, X.F., ZHANG, M., LIU, Z.H., CHEN, J.L. & WUA, G.H. (2004). Magnetic field-controlled two-way shape memory in CoNiGa single crystals. *Applied Physics Letters*, **84**, 3495–3496. 14

LIU, J., ZHENG, H., HUANG, Y., XIA, M. & LI, J. (2005). Microstructure and magnetic field induced strain of directionally solified ferromagnetic shape memory CoNiAl alloys. *Scripta Materialia*, **53**, 29–33. 18, 26

LIU, J., XIE, H., HUO, Y., ZHENG, H. & LI, J. (2006). Microstructure evolution in CoNiGa shape memory alloys. *Journal of Alloys and Compounds*, **420**, 145–157. 16, 17, 18, 34

LIU, Y. & FAVIER, D. (2000). Stabilization of of martensite due to shear deformation via variant reorientation on polycrystalline NiTi. *Acta Materialia*, **48**, 3489–3499. 52

LIU, Y., FAVIER, D. & ORGEAS, L. (1995). Influence of elastic energy on the unloading behaviour of NiTi shape memory alloys. *Journal de Physique IV*, **5-C8**, 593–598. 44

LIU, Y., XIE, Z. & HUMBEECK, J.V. (1999). Cyclic deformation of NiTi shape memory alloys. *Materials Science and Engineering A*, **273-275**, 673–678. 13

MA, Y., JIANG, C., LI, Y., WANG, C. & LIU, X. (2007). Heusler type CoNiGa alloys with high martensitic transformation temperature. *Materials Science Forum*, **546-549**, 2241–2244. 18

MARIONI, M.A., OHANDLEY, R.C. & ALLEN, S.M. (2003). Pulsed magnetic field-induced actuation of NiMnGa single crystals. *Applied Physics Letters*, **83**, 3966–3968. 74

Meyer, D., Maier, H.J., Dadda, J., Karaman, I. & Karaca, I. (2006). Thermally and stress-induced martensitic transformation in CoNiAl ferromagnetic shape memory alloy single crystals. *Materials Science and Engineering A*, **438-440**, 875–878. 2, 18, 30

Miyazaki, S., Imai, T., Igo, Y. & Otsuka, K. (1986). Effect of cyclic deformation on the pseudoelasticity characteristics of Ti-Ni alloys. *Metallurgical Transactions A*, **17**, 115–120. 13

Mosley, M.J. & Mavroidis, C. (2001). Experimental nonlinear dynamics of a shape memory alloy wire bundle actuator. *Journal of Dynamic Systems, Measurement, and Control*, **123**, 103–112. 33

Müllner, P., Chernenko, V.A. & Kostorz, G. (2003). A microscopic approach to the magnetic-field-induced deformation of martensite (magnetoplasticity). *Journal of Magnetism and Magnetic Materials*, **267**, 325–334. 75

Nemat-Nasser, S. & Guo, W.G. (2006). Superelastic and cyclic response of NiTi sma at various strain rates and temperatures. *Mechanics of Materials*, **38**, 463–474. 13

Niklasch, D., Dadda, J., Maier, H.J. & Karaman, I. (2008). Magneto-microstructural coupling during stress-induced phase transformation in $Co_{49}Ni_{21}Ga_{30}$ ferromagnetic shape memory alloy single crystals single crystals. *Journal of Materials Science*, **43**, 6890–6901. 2, 14

O'Handley, R.C. (1998). Model for strain and magnetization in magnetic shape-memory alloys. *Journal of Applied Physics*, **83-6**, 3263–3270. 14

Oikawa, K., Ota, T., Gejima, F., Ohmori, T., Kainuma, R. & Ishida, K. (2001). Phase equilibria and phase transformations in new B2-type ferromagnetic shape memory alloys of Co-Ni-Ga and Co-Ni-Al systems. *Materials Transactions (JIM)*, **42**, 2472–2475. 14, 15, 17, 18, 24, 74

Oikawa, K., Ota, T., Imano, Y., Omori, T., Kainuma, R. & Ishida, K. (2006). Phase equilibria and phase transformation of Co-Ni-Ga ferromagnetic shape memory alloy system. *Journal of Phase Equilibria and Diffusion*, **27**, 75–82. 14, 17

Otsuka, K. & Ren, X. (1999). Recent devlopments in the research of shape memory alloys. *Intermetallics*, **7**, 511. 14, 15

Otsuka, K. & Ren, X. (2001). Mechanisms of martensite aging effects and new aspects. *Materials Science and Engineering A*, **312**, 207–218. 68, 69

Otsuka, K. & Wayman, C.M. (1999). *Shape Memory Materials*. Cambridge University Press. 3, 4, 7, 12, 14, 15, 48, 55, 71

Panchenko, E.Y., Chumlyakov, Y.I., Kireeva, I.V., Ovsyannikov, A.C., Sehitoglu, H., Karaman, I. & Maier, H.J. (2008). Effect of disperse Ti_3Ni_4 particles on the martensitic transformations in titanium nickelide single crystals. *The Physics of Metals and Metallography*, **106-6**, 577–589. 7, 8

Patoor, E., Lagoudas, D.C., Entchev, P.B., Brinson, L.C. & Gao, X. (2006). Shape memory alloys, Part I: General properties and modeling of single crystals. *Mechanics of Materials*, **38**, 391–429. 7

Picornell, C., Pons, J. & Cesari, E. (2001). Stabilization of martensite by applying compressive stress in Cu-Al-Ni single crystals. *Acta Materialia*, **49**, 4221–4230. 38, 52

Ren, X. & Otsuka, K. (1997). Origin of rubber-like behaviour in metal alloys. *Nature*, **389**, 579–582. 68, 69

Rösner, H., Schlossmacher, P., Shelyakov, A.V. & Glezer, A.M. (2001). The influence of coherent TiCu plate-like precipitates on the thermoelatic martensitic transformation in melt-spun $Ti_{50}Ni_{25}Cu_{25}$ shape memory alloys. *Acta Materialia*, **49**, 1541–1548. 7, 8

Sato, M., Okazaki, T., Furuya, Y. & Wuttig, M. (2003). Magnetostrictive and shape memory properties of heusler type Co_2-Ni-Ga alloys. *Materials Transactions (JIM)*, **44-3**, 372–376. 14, 74

Schlagel, D.L., Lograsso, T.A. & Pecharsky, O. (2004). Phase stability of single crystalline Co-Ni-Ga shape memory alloy. *Materials Research Society Symposium Proceedings*, **785**, 219–224. 18, 85

Segui, C., Cesari, E., Font, J., Muntasell, J. & Chernenko, V.A. (2005). Martensite stabilization in a high temperature NiMnGa alloy. *Scripta Materialia*, **53**, 315–318. 14

Sehitoglu, H., Karaman, I., Anderson, R., Zhang, X., Gall, K., Maier, H.J. & Chumlyakov, Y. (2000). Compressive response of NiTi single crystals. *Acta Materialia*, **48**, 3311–3326. 30, 33, 42, 48, 67

Sehitoglu, H., Anderson, R., Karaman, I., Gall, K. & Chumlyakov, Y. (2001a). Cyclic deformation behaviour of single crystal NiTi. *Materials Science and Engineering A*, **314**, 67–74. 13, 46

Sehitoglu, H., Karaman, I., Zhang, X., Chumlyakov, A.V.Y. & Maier, H.J. (2001b). Straintemperature behavior of NiTiCu shape memory single crystals. *Acta Materialia*, **49**, 3621–3634. 30, 33

Sehitoglu, H., Hamilton, R., Canadinc, D., Zhang, X.Y., Gall, K., Karaman, I., Chumlyakov, Y. & Maier, H.J. (2003). Detwinning in NiTi alloys. *Metallurgical and Materials Transactions A*, **34**, 5–13. 30, 33

Shaw, J.A. & Kyriakides, S. (1995). Thermomechanical aspects of NiTi. *J Mech Phys Solids*, **43**, 1243–1281. 59

Sozinov, A., Likhachev, A.A., Lanska, N. & Ullakko, K. (2002). Giant magnetic-field-induced strain in NiMnGa seven-layered martensitic phase. *Applied Physics Letters*, **80**, 1746–1748. 14

Strnadel, B., Ohashi, S., Ohtsuka, H., Ishihara, T. & Miyazaki, S. (1995). Cyclic stress-strain characteristics of Ti-Ni and Ti-Ni-Cu shape memory alloys. *Materials Science and Engineering A*, **202**, 148–156. 13

Tian, W.H., Hibino, M. & Nemoto, M. (1998). Crystal structure and morphology of Co precipitates in B2-ordered (Ni,Co)Al. *Intermetallics*, **6**, 121–129. 15

ULLAKKO, K., HUANG, J.K., KANTER, C., O'HANDLEY, R.C. & KOKORIN, V. (1996). Large magnetic-field-induced strains in Ni_2MnGa single crystals. *Applied Physics Letters*, **69**, 1966–1968. 14, 24

VAINCHTEIN, A. (2002). Dynamics of non-isothermal martensitic phase transitions and hysteresis. *International Journal of Solids and Structures*, **39**, 3387–3408. 57

YAWNY, A., SADE, M. & EGGELER, G. (2005). Pseudoelastic cycling of ultra-fine-grained NiTi shape-memory wires. *International Journal of Materials Research and Advanced Techniques*, **96**, 608–618. 13

ZHANG, M., BRÜCK, E., DE BOER, F.R. & WU, G. (2005). Magnetic, martensitic transformation magnetostriction and shape memory effect in $Co_{50}Ni_{20}Ga_{30}$ melt-spun ribbons. *Journal of Physics D: Applied Physics*, **38**, 1361–1364. 14